RESISTIVE SWITCHING BEHAVIOUR IN OXIDE THIN FILMS AND DEVICES

LAU HON KIT

M.Phil

The Hong Kong Polytechnic University

2010

The Hong Kong Polytechnic University

Department of Applied Physics

Resistive Switching Behaviour in Oxide Thin Films and Devices

Lau Hon Kit

A thesis submitted in partial fulfillment of the
requirements for the degree of Master of Philosophy

August, 2009

CERTIFICATE OF ORIGINALITY

I hereby declare that this thesis is my own work and that, to the best of my knowledge and belief, it reproduces no material previously published or written, nor material that has been accepted for the award of any other degree or diploma, except where due acknowledgement has been made in the text.

Lau Hon Kit

Abstract

Resistive switching effect induced by voltage pulses has been praised as one of the potential candidates for the next-generation non-volatile memories. Resistive random access memory (RRAM) based on transition-metal perovskite oxides has demonstrated a large resistance change upon the application of small and short voltage pulses with different polarities. Some of the advantages of the effect include its fast response, low power consumption, high information packing density and non-volatile characteristics. However, the resistive switching mechanism is still under debate, and the devices have to be optimized before they can be used commercially.

The objective of this work is to study the properties of resistive switching effect based on perovskite manganites including $Pr_{0.7}Ca_{0.3}MnO_3$ (PCMO) and $La_{0.7}Sr_{0.3}MnO_3$ (LSMO), and to investigate the resistive switching mechanism. The research work includes the fabrication and subsequent characterization of PCMO and LSMO oxide thin film-based devices. The performance of the switching devices, including pulse magnitude and pulse width dependences of resistance ratio, data retention ability, and their durability towards repeated switching, have been studied. Moreover, the dependence of the switching effect on metal electrodes has been studied. For resistive switching mechanism analysis, thermal measurements including micro-thermocouples and thermoreflectance imaging techniques were used. By studying the temperature variation in the devices under different voltage biases, AlO_x was found to exist at the Al/PCMO interface, and it is proposed that electrochemical reaction of AlO_x is contributing to the resistive switching effect in Al-based resistive switching devices.

List of Publications

1. H. K. Lau and C. W. Leung, “Nonvolatile multilevel memory effect by resistive switching in manganites thin films, *Journal of Applied Physics,* vol. 104, 123705, 2008.
2. H. K. Lau, C. W. Leung and Y. K. Chan, “Resistance switching properties of epitaxial $Pr_{0.7}Ca_{0.3}MnO_3$, *Physica Status Solidi (a), 1-5,* DOI: 10.1002/pssa.200881782, 2009.
3. H. K. Lau, C.W. Leung, W. H. Hu and P. K. L. Chan, “Interfacial defects in resistive switching devices probed by thermal analysis”, *Journal of Applied Physics*, vol. 106, 014504, 2009.
4. H. K. Lau, P. K. L. Chan and C. W. Leung, “Interfacial Nature of Resistive Switching Effect in Perovskite-Oxide Thin Film Devices”, *Journal of Nanoscience and Nanotechnology* (submitted).

Acknowledgments

The past two years has been a wonderful experience with many ups and downs. I would like to thank my supervisor, Dr. C.W. Leung and Prof. K.H. Wong, for their scientific integrity and support. Their ways of thinking and ideas have led me in the right direction. They always provided information on laboratory basics and advanced research knowledge. I especially thank Dr C.W. Leung for providing a nice and open environment in my research. I also wish to thank Dr C.L. Mak for his scientific discussions in the group meetings. Special thanks goes to Dr. Paddy K.L. Chan from the Department of Mechanical Engineering, who provided lots of supports on thermal analysis and scientific ideas during discussions.

I am grateful to W.F. Cheng and Y.K. Chan for everything that they taught me, including all the trainings on experimental equipment and computer-related issues. Thanks must also go to my groupmates: C.Y. Lam, Irene Pang, Janet Ng, Pai Wong, W.C. Liu, Y.B. Yao, Victoria Li and Hong Wong.

Many people have made my life more enjoyable in research, either in office or the lab in these two years. So, in no particular order, many thanks to Flora Ng, Willy Li, Sarah Suen, Ling Li, Venus Hon, Matthew Wong, Jun Liu, Fred Lee, Argus Chan, Edward Chau, W.H. Wu and Eric Luo.

Finally, away from the campus, this work could not be made possible without the great love from my family and relatives.

Table of contents

List of Figures

Chapter 1 Introduction

1.1 Objectives

Memory device is one of the most important products in the electronics market. To fulfill the needs of various applications, such as computers, digital cameras, and smart mobile phones etc., non-volatile memories with huge storage capacities are needed. In addition, smaller devices packed with increasing number of bits are required for the present information-rich society. Portable hard disks and flash memory devices are representative examples of commercial memory devices. Over 32 GB data can be stored in a single finger-shaped USB flash memory device[1, 2], and the total capacity can be over 500 GB in 2.5-inch portable hard disks[3, 4]. Moreover, these memory devices allow data to be retained without continuous application of power, meaning that they are "non-volatile". The market of non-volatile memory is a business worth billions of dollars, and it is expected to keep growing in the future[5, 6].

The good prospect of the non-volatile memory market provides the incentive for semiconductor companies to continue investing on the research of new memory devices[7]. Non-volatility, high capacity, fast read/write and erase responses, low power consumption, stable data retention and high device endurance are some of the requirements for memory products[8, 9].

Nowadays, the main working mechanism of non-volatile memories is still based on the storage of charges, in which bits of data are stored in individual capacitors within the integrated circuit. For example, charge storage using floating gate transistors technology is the basic principle of operation in flash memory. However, to further improve their performances, many obstacles have to be overcome. When the feature dimensions continue to shrink, charge leakages would become significant in charge-storage type memory devices. For example, leakages due to band-to-band tunneling and gate-induced drain leakages will increase in flash memory devices with smaller device dimensions[10]. Besides, the device of endurance (limited to 10^5 write/erase cycle) and write/erase responses (1 μs) are challenges faced by flash memories as they continue to shrink in size. These challenges will affect the application of flash memory as the substitute for very fast memories like dynamic random access memory (DRAM) and static random access memory (SRAM), which are still used in computers nowadays[10].

At the meantime, new types of non-volatile memory technologies are being investigated[10, 11], such as magnetic random access memory (MRAM)[12-15], ferroelectric random access memory (FeRAM)[16-18], phase-change memory (PCM)[19], and resistive random access memory (RRAM)[20, 21]. MRAM is based on the relative magnetic orientations of two ferromagnetic plates, which are separated by a thin spacer layer. A resistance changes over 100%[13, 14] can be achieved, when the relative magnetization orientation changes between parallel and antiparallel alignment. FeRAM has a similar structure as DRAM, in which the dielectric layer is replaced by a ferroelectric layer. External electric field switches the polarization direction of the dipoles in the ferroelectric, thus achieving different memory states. PCM is based on the phase transition between crystalline and amorphous states of chalcogenide materials, which can be achieved by applying different magnitudes of electrical current and inducing heating. Although these technologies are still being researched, and some issues need to be addressed (*e.g.* superparamagnetism in MRAM when the dimensions of devices are further reduced, low storage densities in FeRAM etc.), they have the potential to compete with flash memory in the non-volatile memory market in the future[22].

The resistive random access memory is investigated in this thesis. RRAM based on oxide materials has shown large electrical resistance changes when exposed to an external electrical stress. Bits of data ("1" or "0") can be stored and represented by the resistance values[9, 22]. Mixed-valence manganese oxides $RE_{1-x}A_xMnO_3$ (RE= Rare Earth, A=Metal) are typical examples of such oxide materials, and the effect is reversible and non-volatile[23-29].

Electric pulse induced resistive switching, or commonly called resistive switching, is one of the means for accomplishing non-volatile RRAM. Electrical voltage signals with short durations are directly applied on oxide thin films, causing large resistance changes[21, 30-36]. This effect provides a promising way for fast[37], low power[29] and high density[38] non-volatile memory devices. Commercial memory products based on resistive switching effect can become possible if the technologies of device fabrication and the switching performances become more mature, and if the mechanism of switching is better understood[24, 39].

In my MPhil project, work was performed in this type of non-volatile memory structure, demonstrating resistive switching effect in mixed valence manganese oxide based structures. Parameters which affect the switching abilities of the structures, for example the magnitude and duration of the voltage pulse applied, will be explored. Bearing in mind the aim of memory applications, the performances of oxide resistive switching structures are also studied, including the reproducibility of the switching, stability of the resistance states in different conditions, etc.

1.2 Plan of thesis

This thesis is focused on understanding the properties and exploring the origin of resistive switching effect in transition-metal perovskite manganese-oxides (manganites). $Pr_{0.7}Ca_{0.3}MnO_3$ (PCMO) and $La_{0.7}Sr_{0.3}MnO_3$ (LSMO) thin films were deposited on $LaAlO_3$ (LAO) substrates by pulsed laser deposition (PLD). The objectives of this project are to analyze the resistive switching effect with different metal electrodes, and to understand the parameters which can affect the switching properties of manganite thin film-based devices. In addition, attempts are made to elucidate the origin of switching in such devices, with the hope of demonstrating more reliable, reproducible and stable non-volatile resistive switching devices.

The thesis is arranged in the following way:

- An overview of the resistive switching effect, and an introduction of the two manganites used in this project (PCMO and LSMO), is provided in Chapter 2. Different possible switching mechanisms are introduced, the structures and the relevant properties of the chosen manganites are described.

- In Chapter 3, an overview of the deposition method and the instruments used to fabricate and characterize the devices are provided. Sample preparations and measurement setups are also introduced.

- Chapter 4 describes the experimental details and results of multi-level RRAM devices based on LSMO. The device fabrication, characterization and measurement procedures are presented. The performance of the devices, including multi-level resistive switching behavior and the retention and endurance of such states, are provided.

- Chapters 5 and 6 focus on the experimental results of RRAM based on PCMO. The resistive switching results of planar geometry PCMO devices, including metal electrode dependence and pulse width dependence, are described in Chapter 5.

Top-down geometry PCMO switching devices are discussed in Chapter 6.

- In Chapters 7 and 8, the mechanism of resistive switching effect in PCMO devices is investigated. Electrical measurements, such as 3-point and 4-point measurements, are discussed. Moreover, results of thermal measurements using micro-thermocouples and thermoreflectance imaging techniques are shown. Based on these measurements, the possible switching mechanism is discussed.
- Finally, in Chapter 9, I summarize the work and conclude the project.

Chapter 2 Literature review of resistive switching effect in oxides and perovskite manganites

In this Chapter, the resistive switching effect is introduced, including a review of literature on its properties and possible mechanisms. The physical properties of the LSMO and PCMO are also discussed.

2.1 Resistive switching in oxides

There is a continuous demand on increasing the data storage capacities of non-volatile memories. Currently, flash memory devices have been expanding fast and strong in the non-volatile memory market. However, commercial flash memory techniques will reach technical limits in the near future if their sizes are kept decreasing[10, 40].

Many researches are attempting to explore new technologies to achieve higher storage density. One of the possible candidates is RRAM based on the resistive switching phenomenon[23, 41]. Such devices are in either a top-down[42-46] or a planar structures[47-49], with a semiconducting or insulating material coupled with two metal electrodes. Such structures are called MIM structures. Due to the simplicity of such structures and the possibility to scale them down into nano-sized devices[50-52], extra-high storage density memories based on resistive switching have been proposed[53, 54]. Moreover, the switching speed of resistive switching can be down to nanoseconds[37, 55], making RRAM a candidate to replace flash memory for the next generation non-volatile memories.

In recent years, various materials have been successfully investigated for resistive switching effect, including binary and mixed valence oxides, such as NiO[56, 57],

TiO_2[21, 58] , Cr-doped $SrTiO_3$[59] , $La_{0.7}Ca_{0.3}MnO_3$[43] , LSMO[27] and PCMO[46]. However, the switching phenomena can be different depending on the material. In terms of the behaviour, resistive switching effect can be classified into two main types, unipolar and bipolar[24].

2.1.1 Unipolar resistive switching

In unipolar resistive switching, the switching effect is independent of the *polarity* of the voltage but depends on the *amplitude* of voltage. It is mostly observed in binary oxides. Before performing unipolar resistive switching, a "forming process" is needed in the device. The forming process is a procedure in which a large voltage bias is applied to the sample, during which the resistance of the sample suddenly decreases, similar to the breakdown of dielectric materials. After that, the device can be switched between high and low resistance values. *Figure 2-1* shows the typical current-voltage (*I-V*) characteristics of the unipolar resistive switching effect.

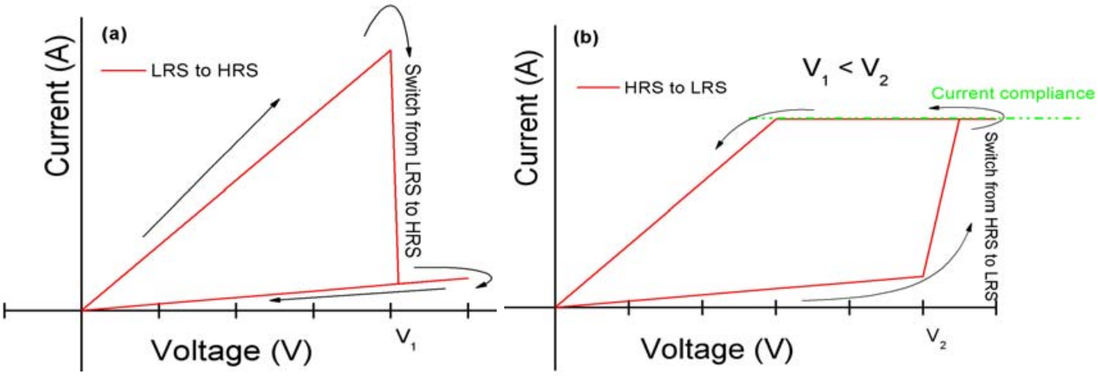

Figure 2-1 Typical I-V characteristics of unipolar resistive switching effect. (a)Switch from LRS to HRS; (b) Switch from HRS to LRS with current compliance.

2.1.2 Bipolar resistive switching

In bipolar resistive switching effect, the polarity of the voltage pulse determines the resistance state of the sample, which is in contrast to the unipolar resistive switching effect. This switching is commonly observed in perovskite oxides. For example, when positive polarity of the voltage set the device to HRS, the application of a negative voltage would switch the device from HRS to LRS. The typical *I-V* characteristic of the bipolar resistive switching effect is shown in *Figure 2-2*

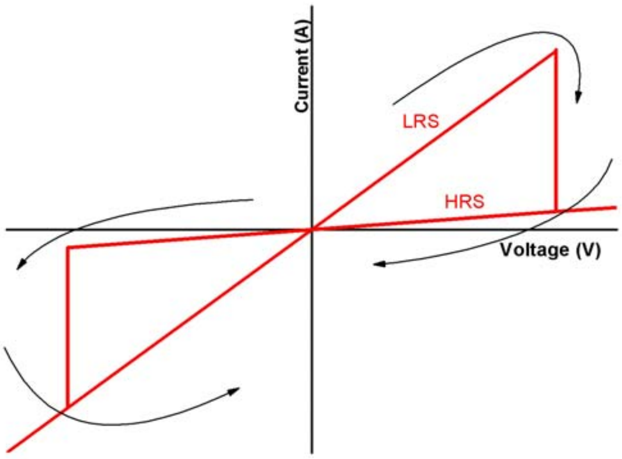

Figure 2-2 Typical I-V characteristic of bipolar resistive switching effect.

2.2 Theories for resistive switching in oxides

Hickmott[60] first reported resistive switching effect in oxide-insulator based MIM structure in 1962. Then lots of scientists also demonstrated the effect with different oxides. However, over the past 40 years, the physical origin of the resistive switching has still not been clarified[24, 39, 61].

Currently, the proposed resistive switching mechanism can be classified in two main groups, one of which I term as ‘bulk effect’ and the other the ‘interfacial effect’. Bulk effect means that resistive switching effect is originates inside the oxide layer, whereas interfacial effect suggests the metal-oxide interface dominants the switching effect.

2.2.1 Bulk resistive switching model

A representative model based on the bulk effect is the filamentation model, in which the formation and rupture of conducting paths in the oxide layer is suggested to be related to the observed resistive switching. This effect was discussed for both unipolar and bipolar switching behavior, but mostly in unipolar devices[62, 63].

In this model, a forming process is generally needed[63, 64]. A high voltage stress (normally larger than the switching voltage) is applied across the device, leading to the formation of initial conducting paths inside the oxide. After this forming process, the device can be switched between LRS and HRS by applying different amplitudes of voltage as described in Section 2.1.1.

When a reset voltage is applied, a large current is passed through the device at LRS. This high current and power destroys the filament paths due to Joule heating effect. The resistance of the device then becomes large and is switches to the HRS. In contrast, when a set voltage is applied, a high electric field with small current is applied on the device. Some filament paths are formed in a way similar to the forming process, except that a current compliance is generally imposed to prevent potential damages to the devices. Those nearly-formed conducting filament paths connect the initially disconnected filament paths and thus the LRS is restored. NiO thin film with Pt electrodes (Pt/NiO/Pt) is a common example of unipolar resistive switching structure explained by the filamentation model[65-67]. The schematics of the filamentation model is shown in *Figure 2-3*.

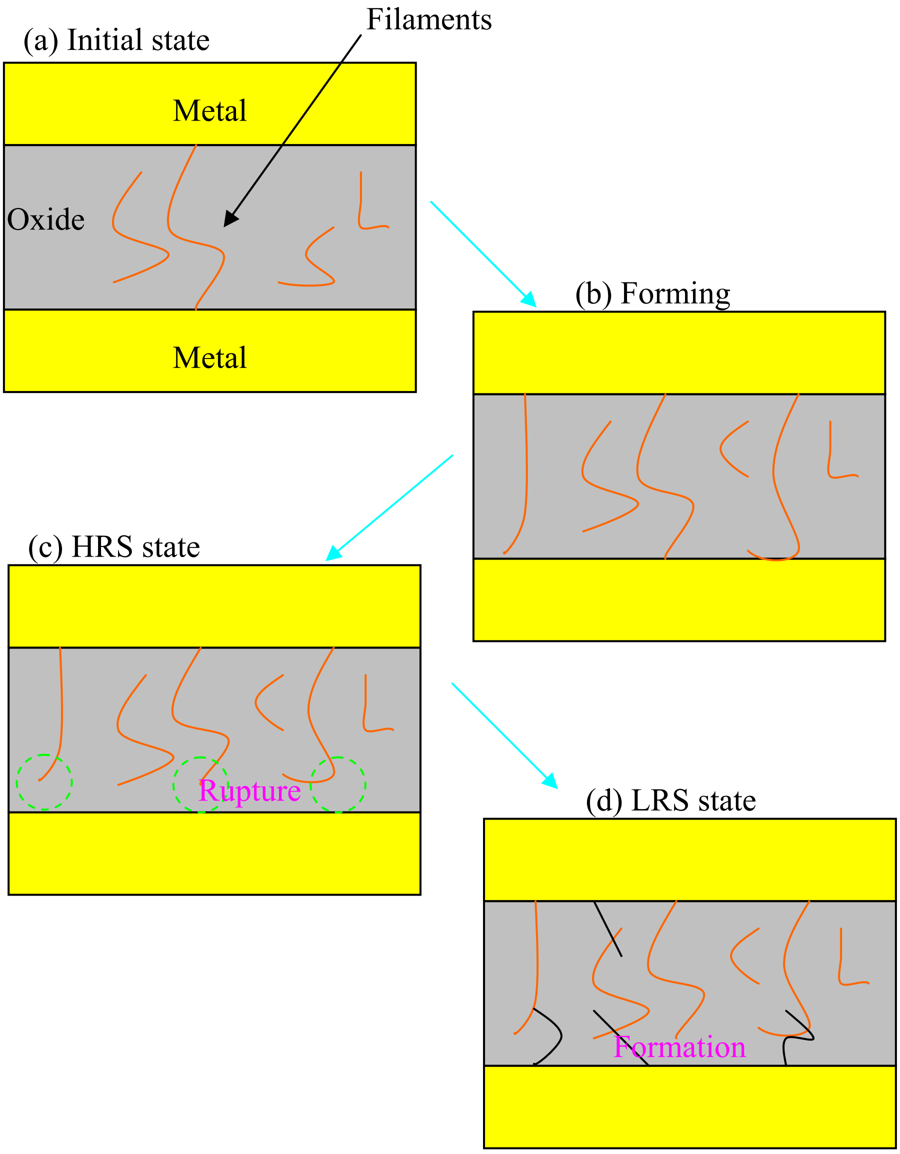

Figure 2-3 Schematic diagram of MIM structure in various states. (a) Initial state,(b) forming process, (c) high resistive state and (d) low resistive state.

2.2.2 Interfacial resistive switching models

Resistive switching phenomenon is treated as an interface effect in a number of models. Such models are mostly used to explain the switching in perovskite oxides and bipolar switching devices[49, 68-70]. To obtain switching effect, commonly two different types of metal electrodes are used instead of using the same metal for both electrodes[48, 71-73]. Some interfacial phenomena used to explain the resistive switching effect include trap states[43, 69, 74-76], oxygen vacancy migration[59, 77-79], and interfacial oxide layers[80, 81].

- **Trap states**

The trap state model[43, 69, 70, 72] can be explained in the following example. In a metal/semiconductor junction, a Schottky barrier is formed in between. A potential difference exist in the interface due to the difference between the metal work function and the electron affinity of the semiconductor. When a voltage is applied, charges are trapped in the metal-oxide interface. When the trapped charges are kept increasing, it would cause both the barrier width and height to be reduced. Charges can therefore be transported through this interface, and hence lowering the resistance value and a large current is observed. The interfacial trapped charges can stay if no external voltage bias is applied and a hysteresis behaviour is observed in the *I-V* measurements.

In contrast, the application of opposite polarity of applied voltage cancels the trapped charges, and the barrier height is back to its initial value. The resistance of the device thus return to the high value. The schematic electronic band diagram for a metal/p-type oxide Schottky interface under different polarity bias is shown in *Figure 2-4*[82].

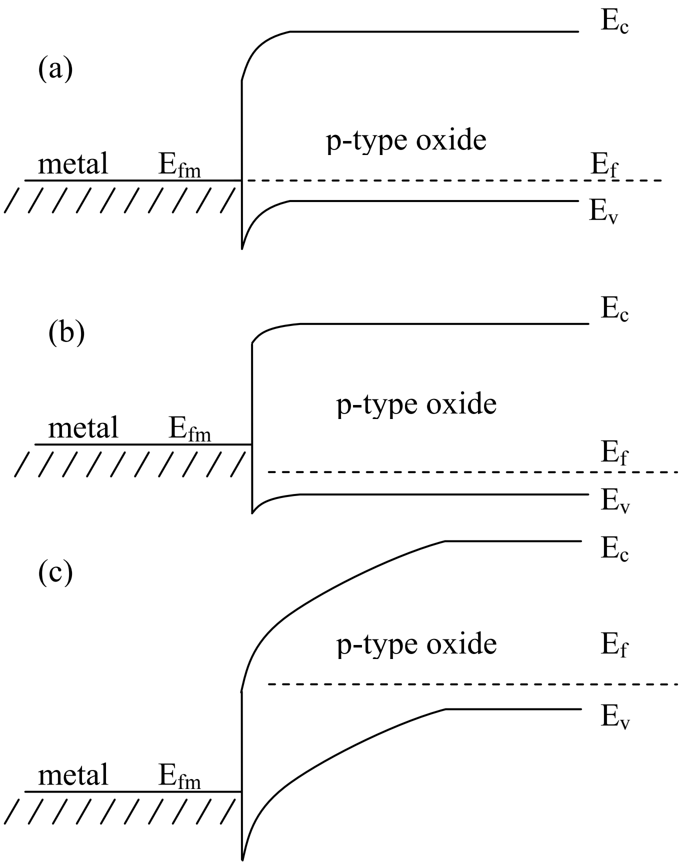

Figure 2-4 Energy band diagram of metal and p-type oxide under different voltage bias condition. (a) no bias, (b) forward bias (LRS) and (c) reverse bias (HRS)[82]. Charges are trapped at the interface.

- **Oxygen vacancy migration**

Oxygen or oxygen vacancy migration can induce resistive switching effect. In some of the transition metal oxides, oxygen vacancies are much more active than cations. Under high voltage conditions, extra oxygen vacancy creation and diffusion occurs and act as conduction paths, and so the device returns to low state[59, 77-79].

- **Formation and disruption of metal oxide**

In some recent reports, it was observed that a metal oxide was formed between the metal and the oxide interface, and it is suggested to be related to the resistive switching effect[80, 81]. For example, in Ti/PCMO interface, a TiO_x oxide is formed when a biased voltage is applied on the sample. The thickness of the TiO_X is formed to changed due to electrochemical reactions. Owing to the changes in the TiO_X layer, the total resistance of the device is switched.

There are lots of other possible mechanisms proposed by different scientists, which involve mechanisms such as the creation of crystalline defects by electric field[71], Mott metal-insulator transition at the interface[83] and they are not introduced here[39].

2.2.3 Literature review for resistive switching effect in oxides

Since the resistive switching effect was first observed in metal-oxide-metal structures in 1960's, binary oxides, such as Nb_2O_5[84] and NiO[56] were used exclusively as the insulator. At that time, NiO thin films showed resistance change by 5 orders of magnitude. However, the devices failed after several hundred switching cycles. Nb_2O_5 can be repeatedly switched between high and low resistive states after the processing[30]. Some scientists at that time already proposed the use of resistive switching effect for computer memory. Unfortunately, the device stability and reproducibility of resistances were the main challenges faced at that time, and there was no substantial improvement in the next 30 years.

In the mid-90s, silicon-based switching devices were investigated. Such devices were simple and made of amorphous silicon, which were compatible with CMOS technology[85]. However, the devices required high forming voltage, which was not controllable and reduced their potential applications.

In 2000, Liu *et al.*[46] demonstrated electric-pulse induced resistive changes in colossal magnetoresistive thin films. Since then the resistive switching effect attracted considerable interest again. Over hundreds of papers were published on resistive switching in the last few years, including different materials, such as binary oxides and perovskite oxides etc. After around 10 years of enthusiastic investigations, resistive switching devices with over 3 orders of switching magnitude[76, 86], reproducibility over 10^5 switching cycles[87], stability over 10^6 seconds[87] were demonstrated.

However, there are still strong debate on the actual mechanism of resistive switching effect. Conducting filament paths were observed in CuO[88] and TiO_2 thin films[58] at LRS by using conducting atomic force microscopy (C-AFM). An insulator-conductor transition, in chromium-doped $SrTiO_3$ single crystal with a resistive switching over 5 order of magnitude was obtained by Watanabe *et al.*[89], which was compared with oxygen vacancies movement modeling. Bipolar resistive switching was investigated in NiO/Pt-coated Si thin film devices, by using C-AFM and time-of-flight secondary ion mass spectrometry (TOF-SIMS). Composition of Ni and O was found to change between HRS and LRS, and the switching mechanism was explained by variation of stoichiometry in NiO[78]. In different polarities of voltage bias, oxygen ions moved and thus changes occurred between the oxygen-stoichiometric, crystalline and insulating NiO state and the oxygen-excess, relatively conducting NiO occurred state.

Another oxygen-related resistive switching mechanism was proposed by Kim *et al*. O_2 annealed Au/PCMO/Pt devices showed higher resistive switching ratio compare with non-annealed ones[29]. X-ray photoelectron spectroscopy (XPS) spectra showed that oxygen-annealed PCMO thin film contained more oxygen, and which led to an increase of the Mn^{4+} content at the surface. They proposed the device conductivity was regulated by the ratio of Mn^{4+}/Mn^{3+} at the metal-oxide interface. Resistive switching occurred, according to Kim *et al.*, due to the Mott transition, in which Mn ions propagated from one metal-oxide interface into the insulating oxide and created a conduction paths[83]. The changes of Mn^{4+}/Mn^{3+} ratio and the corresponding changes in the characteristics of interface domain explained an increasing switching ratio with oxygen annealing.

Scanning Kelvin probe microscopy (SKPM) was also used to measure the surface potential of planar Ag/PCMO/Ag devices[90]. Significant potential changes in the interface between LRS and HRS, which represent resistance changes in the interface region.

In other experiments, impedance spectroscopy was used to analyse the equivalent circuits in the devices. Fe-doped $SrTiO_3$ (Fe-STO)/Nb-doped $SrTiO_3$ (Nb-STO) junction switching devices displayed semi-circular loops of different sizes in Cole-Cole plot at HRS and LRS, and they were attributed to the local resistance changes in the interface[91]. From the observation of I-V characteristics, space-charge limited current and charge trapping in the Schottky barrier were suggested in Ag/$La_{0.7}Ca_{0.3}MnO_3$/Pt[43] and $SrRuO_3$/Nb-STO[69] devices.

2.3 Mixed valence manganites

The work in the project is based on PCMO and LSMO, which are under the category of mixed-valence manganites. The following sections will focus on the general physical features and properties of mixed-valence manganites, especially on calcium-doped praseodymium manganese oxides ($Pr_{1-x}Ca_xMnO_3$) and strontium-doped lanthanum manganese oxides ($La_{1-x}Sr_xMnO_3$).

Mixed-valence manganese oxides, $Re_{1-x}A_xMnO_3$ (Re = rare-earth cation, *e.g.* Pr, La, A = alkaline earth metal cation, *e.g.* Ca, Sr, Ba) with perovskite structure have been studied since 1950s[92]. This kind of material contains lots of new physical concepts, such as double exchange, colossal magneto-resistance, and Jahn-Teller effect[92].

These strongly-correlated electron systems posses strong interaction between spin, charge, orbital and lattice degrees of freedom. A brief review on the crystal structure and electronic properties is shown below[92].

2.3.1 Crystallographic structure and typical perovskite manganites

The ideal crystal structure of mixed-valence manganites is the perovskite structure, and its unit cell is close to the cubic structure (*Figure 2-5(a)*). The large-sized rare-earth ions (Re) and metal ions (A) occupy the cubic corner sites, while the transition-metal Mn ion is located at the center that is surrounded octahedrally by the oxygen ions. The Mn ions are in the state of either Mn^{3+} or Mn^{4+}, with the ratio depends on the doping concentration x (where $Mn^{3+}/Mn^{4+}=(1-x)/x$) and thus $\mathrm{Re}_{1-x}^{3+} A_x^{2+}(Mn_{1-x}^{3+}Mn_x^{4+})O_3^{2-}$ is formed.

However, due to the ionic radii mismatch in the lattice, the ideal cubic structure does not always appear in the real case. Normally the orthorhombic structure is preferred. The crystal structure adopted by the perovskite is governed by the tolerance factor, which is defined by Goldschmidt as [92]:

$$t' = \frac{(r_A + r_O)}{\sqrt{2}(r_B + r_O)} \tag{2.1}$$

where r_A is the ionic radius of the alkaline earth ion, r_B is the ionic radius of the Mn ion and r_O is the radius of oxygen ion. Being a cubic perovskite structure, t' should be between 0.89 and 1.02 . When t' is close to 1, the structure becomes rhombohedral whereas the orthorhombic structure is realized when t' is below 0.95. The ionic radii misfit influences the Mn-O-Mn bond angle and is thus related to the double exchange mechanism. Moreover, the stoichiometry of manganites is related to the oxygen content, which has a critical influence on the material properties including the Curie temperature and the magnitude of magnetoresistance (MR) effect. Therefore, the crystal structure and chemical composition of manganites are closely related to their electronic and magnetic properties[92, 93].

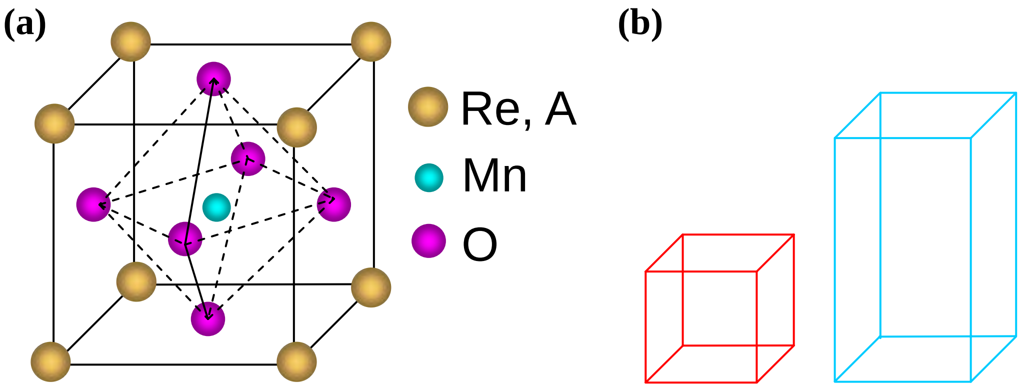

Figure 2-5 (a) Perovskite unit cell of mixed valence manganites and (b) its cubic (red) and orthorhombic (green) unit cells.

2.3.2 Electronic structure and properties

The electronic properties of manganites are mainly due to the correlation between the 3*d* orbitals and the crystal structure. For Mn^{3+} ion, the electronic configuration would be $1s^2 2s^2 2p^6 3s^2 3p^6 3d^4$, where two 4*s* electrons and one 3*d* electron are missing. In contrast, the electronic configuration of Mn^{4+} would be $1s^2 2s^2 2p^6 3s^2 3p^6 3d^3$. In an ideal cubic crystal structure, the five-fold orbital degeneracy in 3*d* orbitals is split into three t_{2g} orbitals and two e_g orbitals by a cubic crystal field. The lower energy t_{2g} orbitals contain three electrons, and the higher energy e_g orbitals take up the rest electron. This e_g electron determines the electrical and magnetic properties of the manganites.

However, most of perovskite manganites crystal structures are distorted due to lots of parameters. Such distortions would lower the symmetry of the crystal field, and it would lower the energy of Mn^{3+} and further split the e_g and t_{2g} energy levels, while nothing would be influenced on Mn^{4+}. This kind of distortion is named as “Jahn-Teller effect"[93, 94]. The energy levels of Mn^{3+} in different structures are shown in *Figure 2-6.*

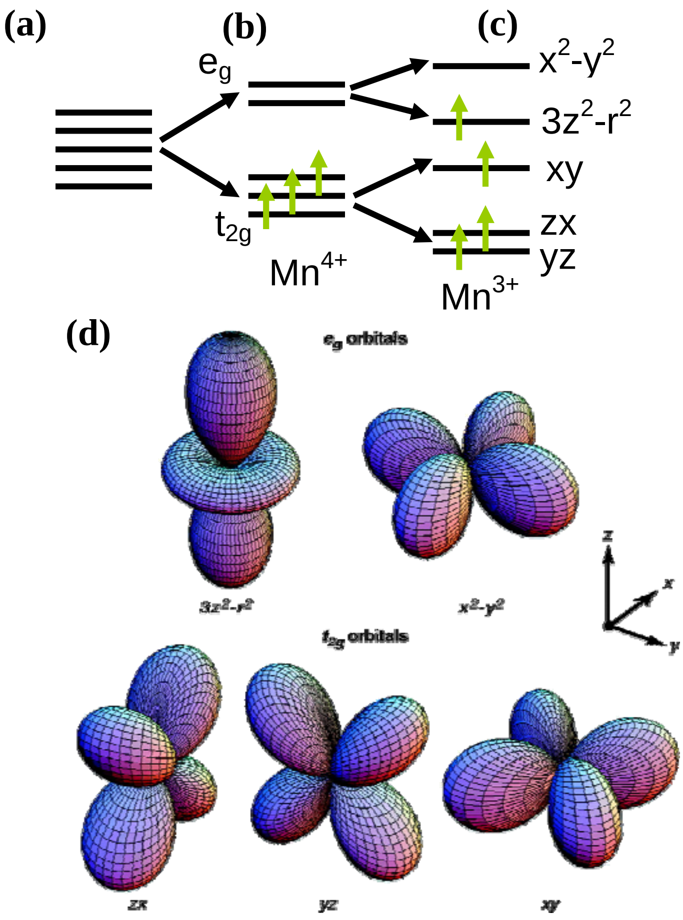

Figure 2-6 A schematic showing the energy level of Mn 3d orbitals: (a) Mn atom, (b) Mn^{4+} *and (c)* Mn^{3+} *after Jahn-Teller distortion. (d) The shape of five 3d orbitals in distorted perovskites.[94]*

As mentioned before, the e_g electron determines the electrical conduction in manganites, which is actually related to the Mn-O-Mn bonds. Due to the relatively little overlap between the t_{2g} orbitals and the orbitals of oxygen, the t_{2g} electrons tend to be more localized. However, the e_g orbitals have a large overlap with the *p* orbitals of the oxygen, which increases the possibility of electron hopping. In the case of Mn^{3+}-O-Mn^{4+} bonding, the Mn ions can exchange their valences by the jumping of a e_g electron from Mn^{3+} to the *p* oxygen orbital, and simultaneously, from the same oxygen orbital to the empty Mn^{4+} e_g orbital. After the electron transfer, Mn^{3+} becomes Mn^{4+} and the electrical conductivity is increased. This simultaneous electron transfer is called 'double exchange'. Double exchange occurs when the manganese spins are in parallel states, but it would become more difficult when the manganese spins are not in parallel or when the Mn-O-Mn bond is bent[92]. The schematic diagram of double exchange mechanism and its related orbital overlapping are shown in *Figure 2-7.*

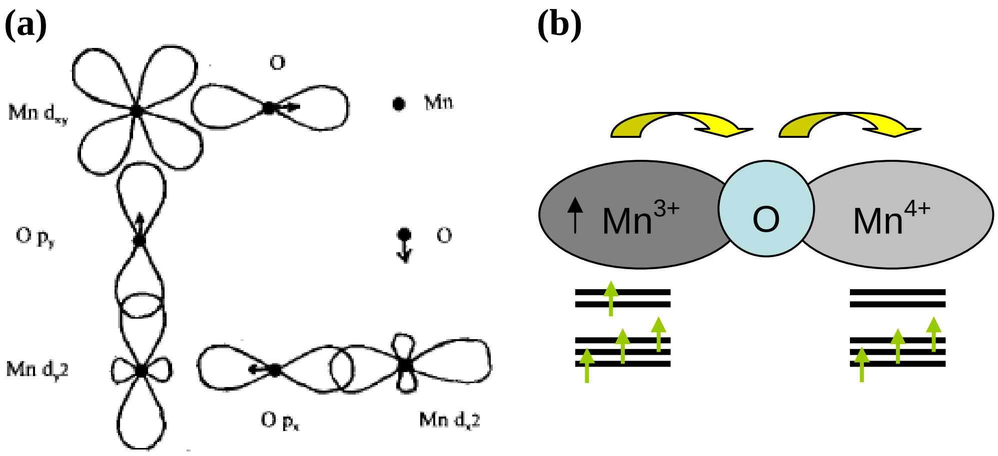

Figure 2-7 Schematic graph of (a) orbital overlap in a plane of the perovskite structure. The xy orbital has overlap little with O 2p orbital (upper panel) where $x^2$and y^2strongly overlap with O 2p orbital (lower panel)[92]. (b) The double exchange mechanism.

2.3.3 Basic properties of $Pr_{1-x}Ca_xMnO_3$ compounds

In the case of $Pr_{0.7}Ca_{0.3}MnO_3$, the crystal structure is orthorhombic, which *t'=0.95* calculated by equation (2.1), where r_A is the composition-averaged ionic radius of $Pr_{0.7}Ca_{0.3}$ (Pr^{3+} = 0.129 nm, Ca^{2+} = 0.134 nm), r_B is the corresponding averaged ionic radius of Mn (Mn^{3+} = 0.0645 nm, Mn^{4+}= 0.053 nm) and r_O = 0.140 nm. Jahn-Teller distortion would induce double exchange, in which electron hopping occurs in e_g orbitals. However, $Pr_{1-x}Ca_xMnO_3$ shows insulating behaviour at room temperature irrespective of the doping concentration, *x*. Its hopping for e_g orbitals is smaller than other manganites such as $La_{1-x}Ca_xMnO_3$ and $La_{1-x}Sr_xMnO_3$ due to the smaller sizes of Pr and Ca ions, and thus PCMO has a narrower e_g bandwidth[95, 96]. In the $Pr_{1-x}Ca_xMnO_3$ phase diagram (*Figure 2-8(a)*), $Pr_{1-x}Ca_xMnO_3$ is a paramagnetic insulator at room temperature. However, it has several phase transitions depending on the doping concentration x at low temperature. When the temperature decreases in the range of $0.3 \le x \le 0.75$, charge-ordered insulating phase is observed when temperature is below 250K. The second phase transition to an antiferromagnetic phase takes place at Neel temperature T_N ~170K. Canted antiferromagnetic phase occurs below T_{CA} ~110K when $0.3 \le x \le 0.4$. According to the $Pr_{1-x}Ca_xMnO_3$ phase diagram, ferromagnetic state is not achieved in any composition, in contrast to other manganites, again due to its small tolerance factor[92].

As mentioned before, a stable insulating state is observed in $Pr_{1-x}Ca_xMnO_3$ in the range of $0.3 \le x \le 0.75$. The resistivity of $Pr_{1-x}Ca_xMnO_3$ increases exponentially when the temperature decreases. According to the resistivity vs temperature diagram, no transition peak is obtained. However, an interesting effect can be observed, in which the ferromagnetic metallic state is induced by applying a strong magnetic field. This transition also reduces the resistivity of $Pr_{1-x}Ca_xMnO_3$. In *Figure 2-8(b)*, the resistance of a single crystal $Pr_{0.7}Ca_{0.3}MnO_3$ is diminished by over 8 orders of magnitude when a 70-kOe magnetic field is applied at low temperature (4.2 K). This magnetic field induced resistance decrease phenomenon is known as the colossal magnetoresistive (CMR) effect. ‘Colossal’ is used to illustrate such a dramatic effect and to distinguish it from the giant magnetoresistance effect[97]. Insulator-to-metal transition can also be induced in CMR materials by irradiation with x-rays[98], ultraviolet light[99] or electric field[100] at low temperatures.

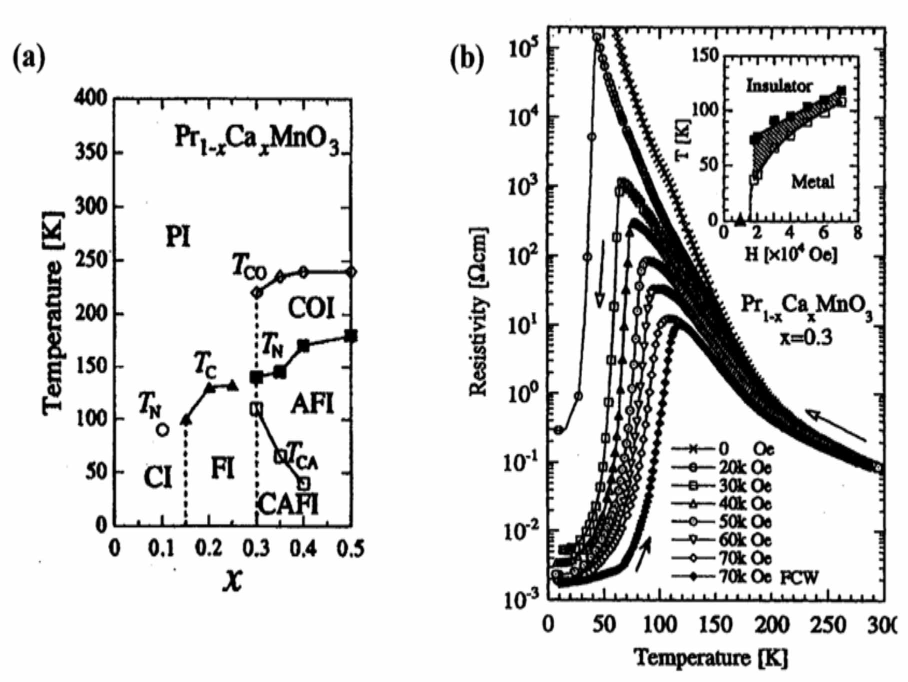

Figure 2-8 Phase diagram and colossal magnetoresistance effect of $Pr_{1-x}Ca_xMnO_3$ single crystal. (a) The phase diagram of a single crystal $Pr_{1-x}Ca_xMnO_3$ with transition temperature vs hole concentration x. (b) The resistivity of a single crystal $Pr_{1-x}Ca_xMnO_3$ of x=0.3 undergoes up to 8 orders of magnitude resistivity change under the application of a strong magnetic field (up to 7 Tesla)[97].

2.3.4 Basic properties of $La_{1-x}Sr_xMnO_3$ compounds

LSMO has a rhombohedral crystal structure, with *t'=0.98* calculated by the tolerance factor equation (La^{3+} = 0.136 nm, Sr^{2+} = 0.144 nm, Mn^{3+} = 0.0645 nm, Mn^{4+}= 0.053 nm and r_O = 0.140 nm). Due to the larger ionic radii of La^{3+} and Sr^{2+}, $La_{1-x}Sr_xMnO_3$ ($x>0.17$) is metallic with a board bandwidth. This is different from the insulating and narrow-band width nature of $Pr_{1-x}Ca_xMnO_3$. Because $La_{1-x}Sr_xMnO_3$ is a half-metallic material with low saturation magnetization and low resistivity, it is commonly used for demonstrating giant magnetoresistance (GMR) effect. According to the $La_{1-x}Sr_xMnO_3$ phase diagram *(Figure 2-9)*, as the doping concentration $x>0.17$, the ferromagnetic state becomes stable. A transition of resistivity can be observed in resistivity vs temperature diagram when $x>0.1$. When the temperature decreases to a critical point, the paramagnetic phase transits to the ferromagnetic phase, and that transition point is normally taken as Curie temperature. This ferromagnetic phase must be needed for GMR devices and other applications.

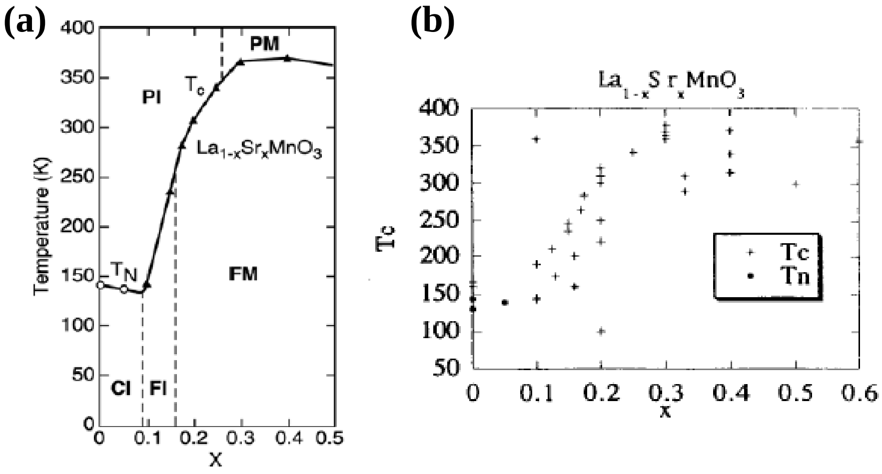

Figure 2-9 (a) Phase diagrams showing transition temperature verse concentration, x, of single crystals of $La_{1-x}Sr_xMnO_3$*[93]; (b) Curie and Neel temperature of* $La_{1-x}Sr_xMnO_3$*[92].*

2.3.5 Material selection

In the project, $Pr_{1-x}Ca_xMnO_3$ and $La_{1-x}Sr_xMnO_3$ with $x=0.3$ (PCMO and LSMO) are chosen. PCMO and LSMO have shown resistive switching effect by applying voltage pulses at room temperature, especially in thin film devices. Studies of materials similar to that used by other scientists allow better comparison with the results ion the literature. Moreover, bipolar resistive switching has good potential for application as non-volatile memory, and such kind of switching is mostly observed in perovskite oxides. Besides, PCMO is at the boundary of several phases, and that insulator-metal transition appears with a minimum magnetic field compared with other doping concentration[97]. LSMO has the highest Curie temperature (370 K [92])which is over room temperature in comparison with other doping concentration. Both PCMO and LSMO have similar lattice constants, and this allows the epitaxial growth on typical single crystal substrates such as $SrTiO_3$ (STO) and $LaAlO_3$ (LAO). PCMO and LSMO have a wide range of functionalities, which can be tuned by electric field or magnetic fields, and they are valuable for future applications[97, 101].

2.3.6 Literature review for resistive switching in PCMO and LSMO

In the last 10 years, there are lots of milestones in the study of PCMO and LSMO resistive switching effect. Firstly, in 2000, Liu *et al.*[46] observed the electric pulse-induced resistance changes in PCMO thin films, with switching ratio over 1700 % was obtained. Switching ratio over 3×10^3 % was observed by Odagawa *et al.*[72]. In term of the switching voltage of the device by switching below ±2 V was achieved [27, 29] compared to over ±10 V demonstrated by Liu *et al.*[46].Moreover, high density prototype memory device was demonstrated in 2007, which was based on multi-level resistive switching by applying voltage pulses of different values[27].

Apart from the resistive switching performance, the fabrication conditions were also changed. Originally, LAO[46] or MgO[72] single crystals were used as substrates. In recent years, Si substrates were used, which was more compatible with microelectronic processing[102]. Furthermore, Ruotolo *et al.*[103] achieved resistive switching in LSMO/Nb-STO *p-n* junctions. Besides, switching mechanisms were also studied in PCMO and LSMO, which will not be discussed in details here[48, 70, 71, 103-105].

2.4 Summary

This chapter introduced the current states of resistive switching effect, including the switching behaviors and possible switching mechanisms. Moreover, physical background of the transition metal perovskite oxides was also presented. Over several orders of magnitude of resistance changes with low power electrical pulses, and the possibility of multi-bit storages with different resistances by applying various magnitude of electrical pulses, would bring RRAM to achieve a milestone in the near future. Thus electric pulse induced resistive switching devices are worthy to be investigated for non-volatile memory applications.

Chapter 3 Experimental methods

This Chapter provides an overview of experimental methods used in the project. These include the oxide thin film growth and device fabrication methods. Besides, descriptions of the instruments I have utilized to characterize the properties of resistive switching devices are provided.

3.1 Thin film Growth technique

Pulsed laser deposition (PLD) is the main deposition technique used for thin film fabrication in the project, including oxide thin films (*e.g.* PCMO, LSMO) and metal electrodes (*e.g.* Pt, Au, Ti, Ni, Al etc.). LAO (001) single crystals were used as substrates, as LAO is insulating and has similar lattice constants with the oxides. This permits the growth of epitaxial oxide thin films and not affecting the switching performance of the electrical measurement due to its high resistivity.

3.1.1 Pulsed laser deposition

PLD is a technique commonly used for the fabrication of high-quality oxide thin films. By using ceramics with precisely-controlled stoichiometry as deposition targets, the stoichiometries in the thin films subsequently deposited can be controlled.

The mechanism of PLD is simply energy conversion. High-energy laser pulses first impinge on the target, and all elements on the target surface are evaporated. In PLD, a number of ablation mechanisms are involved. These include thermal, mechanical and electronic excitations etc., which each reaction producing different energetic species such as atoms, ions, clusters, particulates etc. Those ablated materials move to the substrate together and form a luminous plasma called plume. The energetic species reach the substrate, collide with the substrate surface, condense on the surface and lead to the film growth[106, 107].

Three different nucleation and thin film growth modes can be categorized. They arise from the combination of various parameters such as substrate temperature, density and energy of ablated species, and physical-chemical properties of the substrates etc.: (1) three-dimensional island growth (Volmer-Weber), (2) two-dimensional full monolayer growth (Frank-van der Merwe), and (3) two dimensional growth of full monolayers with three-dimensional islands growth (Stransk-Kastinov).[106, 107]

The main advantage of the PLD technique is the good stoichiometric control, which is hard to achieve by other deposition methods. Using high-energy laser as an excitation source, all of the components of the target material can be evaporated and thus thin films of all materials can be deposited in principle. Furthermore, by using flanges which can accommodate multiple targets, *in-situ* growth of composites or multilayers with different materials, under different ambient gas conditions, are feasible.

However, there are some shortcomings for PLD. There are limitations on the substrate size that can be used due to the issue of inhomogenity of film thickness. The film thickness is the largest right under the center of the plume, which gradually decreases with increasing distance from the center. To obtain a relatively uniform thin film, the deposition area is limited to around 1 cm^2 right under the centre of the plume. The generation of particulates is another main problem of PLD. Owning to the high power of laser, all of species, as well as impurities and large particulates, are deposited onto the substrate and this leads to high surface roughness of the deposited films.

3.1.2 PLD setup

Figure 3-1 shows the schematic of the PLD system used in the project. The vacuum chamber is connected with a pressure sensor, a rotary pump, a fused-silica glass window, substrate and target holders.

Before the oxide thin film deposition process, substrates were cleaned with acetone and ethanol successively in an ultrasonic bath for at least 5 minutes. During this period, targets were mounted mechanically on target holders by screws, and then the targets were pre-ablated to remove surface impurities. Then the cleaned substrates were fixed on the substrate holder with silver paint. The chamber was then pumped for at least 30 minutes until a base pressure of 10 mTorr or better was achieved. Subsequently, the substrate holder was heated up to the required temperature, and then oxygen was filled when the target substrate temperature was reached.

During the deposition, a Lambda-Physik KrF excimer laser with wavelength 248 nm was used with a pulse rate of 5 Hz. The laser pulses were focused by a lens with a focal length of 27 cm, and were transmitted through a fused-silica glass window, on the target surface. The substrate–to-target distance was set at 4 cm. After deposition, the heater was cooled down at a rate of about 10 ℃/min with the same oxygen pressure as deposition until it reached room temperature.

For metal electrode deposition, a lower base pressure is needed in order to obtain high-quality metal thin films. In this case, a similar vacuum chamber with a diffusion pump and an ionization gauge was used. With the diffusion pump, the base pressure of the vacuum chamber can reach down to at least 10^{-5} Torr range. The ionization gauge was used for measuring the pressure at high vacuum.

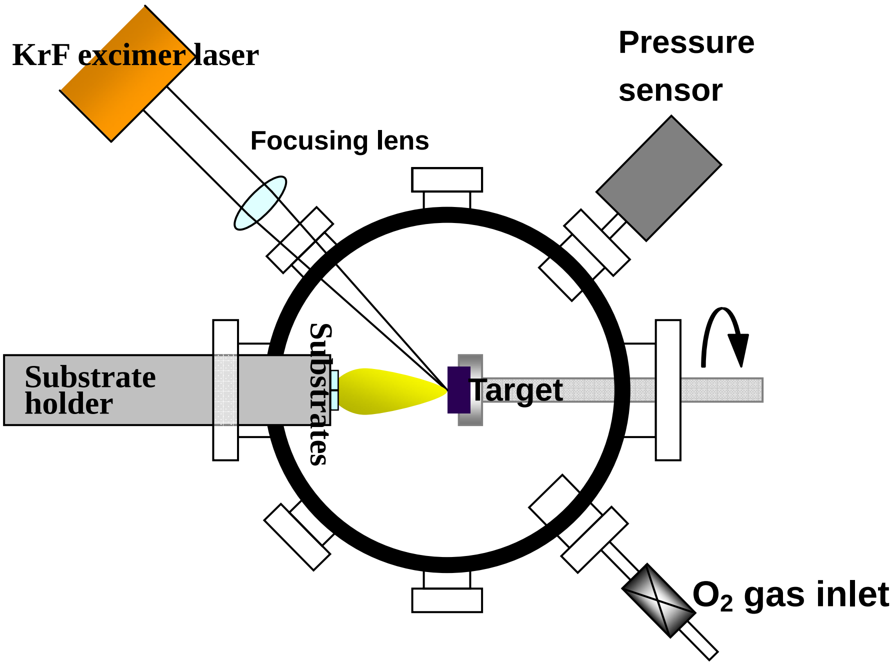

Figure 3-1 Schematic diagram of PLD system used in the project

3.1.3 Targets preparation

Targets for PLD are important for the successful thin film fabrication. Conventional solid-state reaction methods were used for synthesizing LSMO and PCMO targets in this project[108]. PCMO target was fabricated by using, Pr_2O_{11}, $CaCO_3$ and MnO_2 powders, La_2O_3, $SrCO_3$, MnO_2 powders were used for preparing LSMO target. The powders were first dried at 100 ℃ for at least 3 hours in air separately. After that, appropriate weight ratios of powders were mixed and ball-milled for 6 hours. Mixed powders were grounded and reacted in ambient at 1200 ℃ for 10 hours. The calcinated powders were ground into fine powder and pressed into pellets by an oil compressor with a 5-Tons force for 10 mins. Finally, the pellets were sintered at 1350 ℃ for 10 hours. The targets were characterized by XRD and EDX.

3.2 Device fabrication

3.2.1 UV photolithorgraphy

To fabricate planar devices with desired patterns, and to study the electrode dependence of resistive switching effect, a two-step UV photolithography process was adopted. Masks were designed by using AutoCAD^{TM} for producing square or circle arrays, with a minimum separation of 30 μm. Due to the limitation of mechanical shadow protection masks used (minimum separation possible 150 μm), they cannot be used in order to prepare smaller devices. So photolithography was used when junctions smaller than 150 μm were needed. The fabrication process of two sets of electrodes with different materials on the same thin film is shown in *Figure 3-2*.

The photolithography process was performed in a class-1000 cleanroom. After the deposition of thin films, around 3 μm thick of AZ 5214 photoresist was spin-coated on the surface of the sample, which was rotated at a rate of 4000 revolutions per minute (rpm) for 60 s. The sample was then baked in an oven at 95 ℃ for 1 minute. Afterwards, the sample was put under a UV double-side mask aligner to adjust the position of the sample. Illumination of UV light with a power density of 24 mW/cm^2 was carried out through the mask for 15 s. Lastly, the sample was immersed in a beaker filled with AZ 300 MIF developer for 40 s, during which the illuminated regions of photoresist was removed. The desired patterns were therefore transferred from the mask to the surface of the sample.

The next step was to deposit the first type of metal electrodes by using PLD method. After that, the sample was placed in acetone for over 1 hour for lift-off, during which the desired pattern of metal electrodes remained on the samples while all the photoresist was dissolved. To ensure complete removal of photoresist, the samples were placed into a low-power O_2 plasma, in which the photoresist reacted with O_2 and left the sample surface free from organic compounds. The photolithography process was then repeated, but the alignment was done carefully; this ensured that the second set of patterns did not overlap with the previous set of metal electrodes, and the desired electrode separation could be achieved. Deposition of the second set of metal electrodes was performed, followed by another lift-off process. Finally, a sample with two different types of metal electrodes was fabricated.

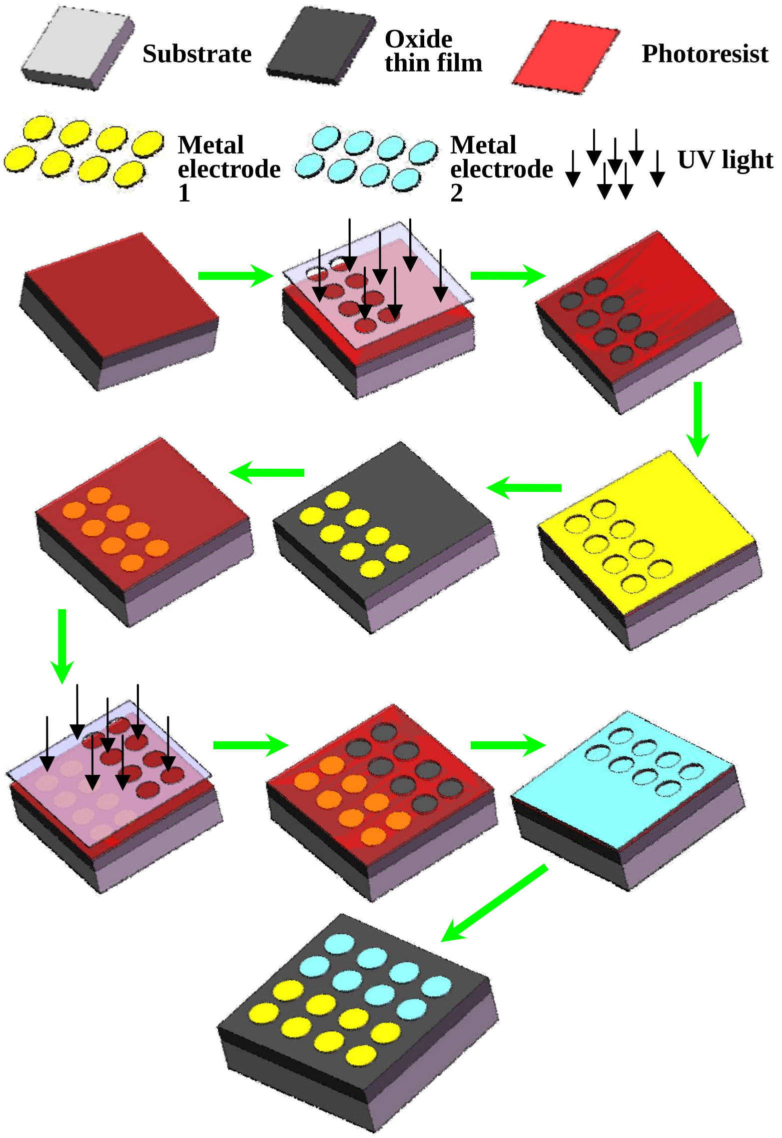

Figure 3-2 UV-photolithography procedures for fabricating two different types of metal electrodes on the same oxide thin film.

3.3 Structural and surface characterization methods

3.3.1 X-ray diffraction (XRD)

XRD is a non-destructive method to characterize the crystal structure of bulk and thin film samples. An x-ray beam diffracts when it interacts with atoms. Based on Bragg's law, constructive interference occurs at certain incident angles θ with crystal plane:

$$2d\sin\theta = n\lambda, \quad n = 1,2,....$$

where d is the atomic plane separation, θ is the angle of incident ray, and λ is the wavelength of the x-ray source. From the peaks present in the diffraction pattern, the lattice parameters of the unit cell a, b and c could be calculated if λ is known. In this project, a Bruker D8 Discover x-ray diffractometer was used. Three main types of measurements (θ-2θ scan, rocking curve (ω- scan) and phi- (ϕ) scan were performed. CuK_α x-ray radiation with λ = 1.541 Å was used.

Firstly, θ-2θ scans were performed, during which the detector and the sample were rotated at an angular speed ratio of 2:1. The θ-2θ scan can give the out-of-plane lattice parameters by calculating by the Bragg's equation. Afterwards, the degree of crystallinity of the film was obtained by rocking curve measurements. During the rocking curve measurement, both the x-ray source and the detector were fixed for a certain angle related to the atomic plane spacing, while the sample was rotated (or rocked) about the ω-axis. A peak was obtained, and the full-width at half-maximum (FWHM) is a measure of the distribution of alignment of crystallites. The smaller the FWHM, the stronger the preferred alignment of crystallites in a particular direction. In order to understand the epitaxial relation between the thin film and the substrate, ϕ scan was performed. The detector was set at a certain angle which can detect the reflection signals of the thin film from a particular plane. The sample was also titled to a related angle through the χ-axis in order to measure the corresponding peak, followed by a scanning on the ϕ-axis. If the thin film was epitaxially grown on the cubic LAO substrate, four peaks with 90° separation in ϕ should be observed and the peak positions of the substrate and the thin film should overlap. The schematic of x-ray measurement geometry is shown in *Figure 3-3.*

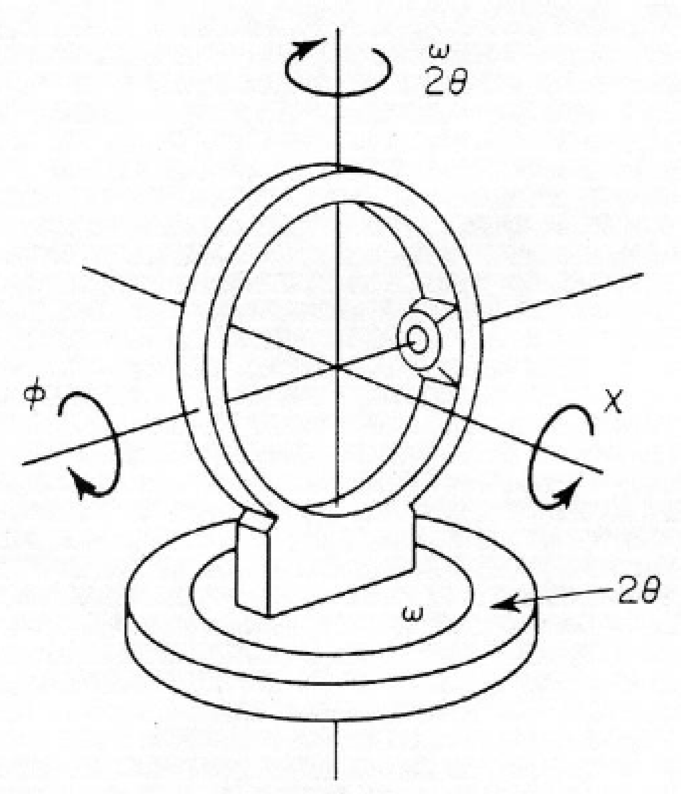

Figure 3-3 Geometry of four axis x-ray diffractometer[109].

3.3.2 Scanning electron microscopy (SEM), focused ion beam (FIB) microscopy and energy dispersive x-ray (EDX) spectroscopy

SEM is a conventional technique to image sample surfaces. By using the SEM, the thickness and the surface quality of the thin films can be obtained. In a SEM, an electron beam is emitted and accelerated, and then it is focused by electromagnetic lenses. When electrons bombard on the surface of a sample, inelastical scattering of electrons occurs. The interaction between the electron beam and the sample can generate secondary electrons, backscattered electrons, Auger electrons, cathodoluminescence and x-rays. The image of the SEM is built upon by collecting the secondary electrons emitted from irradiated areas of the sample.

On the other hand, FIB is a technique used for the analysis or deposition of material on specific positions. Instead of using electron beam, metal ions are emitted and accelerated to high energy and focused by electrostatic lens. When the ions hit on the sample, atoms are sputtered from the surface. Thus FIB can be used for nano-machining purposes.

The purpose of using SEM and FIB in this project was to check the film thickness and inspect the interface of the samples at specific location. FIB was used for performing etching at certain areas of the electrodes, and SEM was subsequently used to observe the interface between the oxide thin films and the metal electrodes. To avoid destruction of the surfaces, tungsten protecting layers were deposited on the designated areas of the samples before FIB etching.

In addition, SEM system is commonly accompanied by EDX facilities, which can be used for characterization of chemical composition. In the project, EDX was used to characterize the composition of the PLD bulk targets.

3.4 Electrical characterizations

3.4.1 Two-point measurement

Two-point measurement is typically used to measure the resistance of the sample. A schematic diagram of the experimental setup is shown in *Figure 3-4*. Two-point measurement is the simplest way to measure the resistance, and it can be performed irrespective of the geometry of samples.

In my measurements, a Keithley 2400 sourcemeter was used. Voltage or current was applied by the sourcemeter, and the corresponding current or voltage values of the sample were extracted. This two-point measurement technique was performed in *I-V* characteristics and resistive switching behavior measurements, where sometimes a pulse generator was added in the circuit for the application of short (<1 ms) voltage pulses.

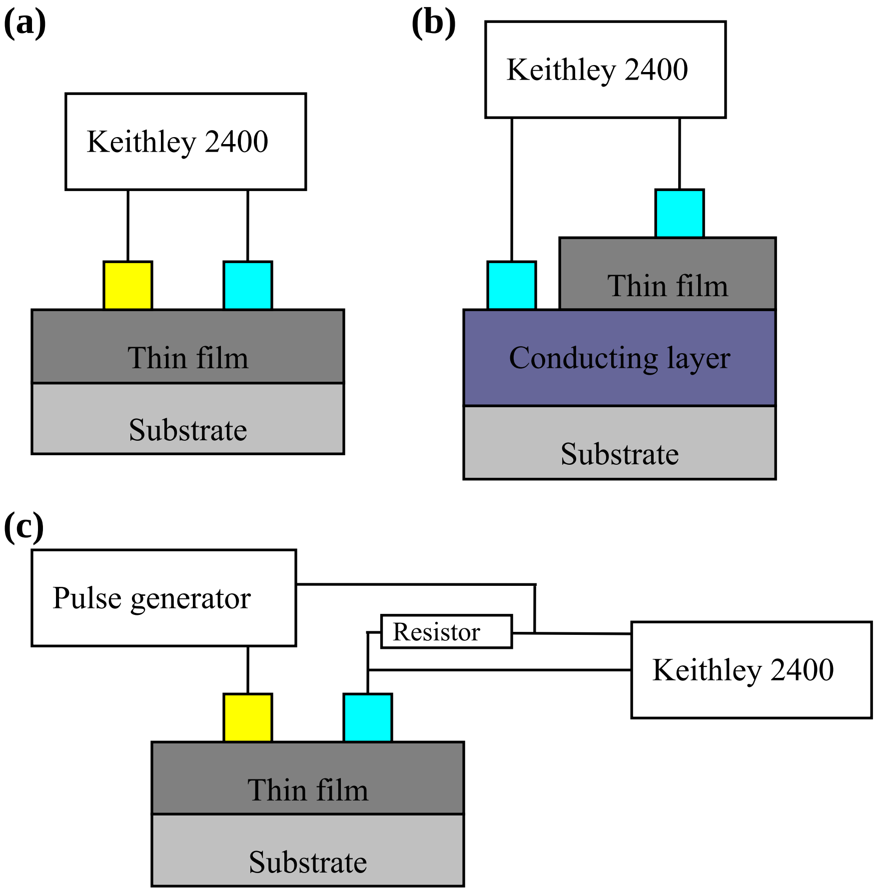

Figure 3-4 Schematics of electrical setups for (a) planar and (b) top-down device geometry for measuring I-V and resistive switching characteristics. (c)Resistive switching measurements were made with pulse duration <1 ms.

3.4.2 Three-point measurement

Three-point measurement is a simple method to obtain the interface resistance between oxide thin films and metal electrodes. In order to determine the resistive switching effect and the contribution of interfaces to the total resistance of the devices, this measurement was used to obtain the interface resistance between metal electrodes and oxide thin films [110].

Two Keithley 2400 sourcemeters were used for the measurement, one for providing a constant current and the other for measurement of potential difference. Three contact pads were required, and the schematic circuit is shown in *Figure 3-5*. A voltage pulse was first applied across electrodes 2 and 3 for switching. A small constant current (I_{12}) was then forced through these two electrodes, using a Keithley 2400 sourcemeter (labeled Keithley 2400 I in Figure 3.5(a)). Owing to the contact resistance in the interface between electrode 2 and the thin film, a potential drop can be observed. This potential drop (V_{23}) across the interface can be probed across electrodes 2 and 3 using another Keithley 2400 (labeled Keithley 2400 II in Figure 3.5 (a). The interface resistance can then be calculated by $\frac{V_{23}}{I_{12}}$. By measuring the difference of interfacial resistance values between LRS and HRS, the interface or bulk contribution to the switching effect can be estimated [49, 111].

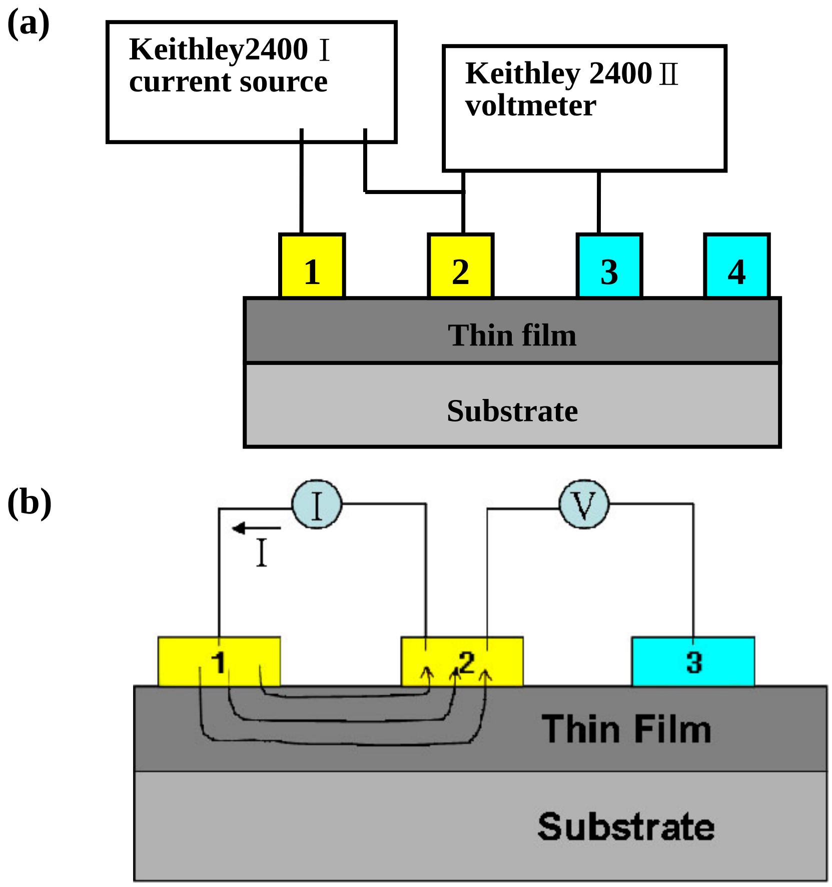

Figure 3-5 (a)Schematic diagram of three-point measurement. Keithley 2400 Ⅰ is used either as a constant current source for measurement in junction 1, 2. Keithley 2400 Ⅱ is used to measure the voltage across electrode 2 and the oxide thin film. (b) Electrical circuit of the three-point measurement.

3.4.3 Four-point measurement

The purpose of four-point measurement is to determine the bulk or intrinsic resistance of thin films by eliminating the contact or interface resistances. Four-point measurement was used to determine the resistance and the *I-V* characteristics of oxide thin films in this work. When planar geometry devices show resistive switching effect in two-point measurement, four-point measurement can be further performed to determine the location for the occurrence of the switching effect.

In the measurement, four contact pads were needed, and a Keithley 2400 was used to supply a constant current. The same multimeter was used to measure the voltage across another pair of electrodes on the thin film. In this case, only one Keithley 2400 sourcemeter was needed due to the presence of such a measurement functionality. The four-point resistance measurement setup is shown in *Figure 3-6*. By comparing the *I-V* characteristics between two-point and four-point measurements, the relative contributions of bulk or interface switching effect can be deduced.

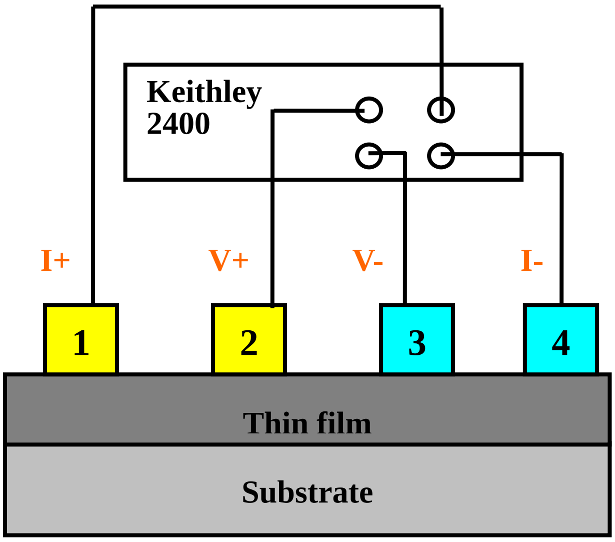

Figure 3-6 Schematic diagram of four-point measurement. Contact pads 1 and 4 are connected to the current source, while pad 2 and 3 are used for voltage measurement across the thin film channel between them.

3.5 Thermal measurements

3.5.1 Micro-thermocouple measurement

Micro-thermocouple measurement is a low cost, straightforward technique for localized temperature measurements. A thermocouple is a junction made of two dissimilar metal wires that joined together. Owing to the thermoelectric properties of different metals, a potential is developed when the thermocouple is heated. The measured voltage can be correlated with the temperature at the junction. Theoretically, any two different metals can be used to form a thermocouple, but there are some standard commercial thermocouples available on the market.

In my experimental setup, two commercial 30 µm type-T micro-thermocouples, which were made of Cu and Cu/Ni alloy with an accuracy of 0.01 K, were used (*Figure 3-7*). In the experiment, planar resistive switching devices with electrodes of two different materials were involved. The device was connected to a Keithley 2400 multimeter for electric source biasing. Two thermocouples were placed on the surface of metal electrodes directly. They were then connected to a TC-2000 measurement station for thermal voltage-temperature conversion. Temperature data were recorded by a LABVIEW program at a rate of 5 Hz. The temperature variations between the two electrodes under the same biasing, and the temperature difference between the electrodes in different bias condition, were measured.

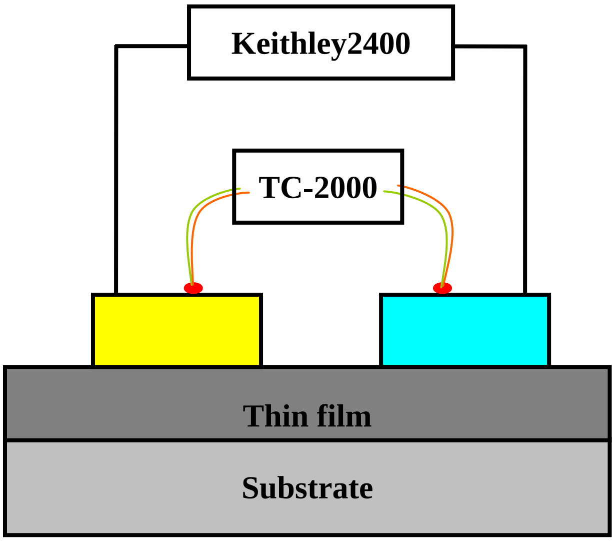

Figure 3-7 Schematic diagram of micro-thermocouple setup.

3.5.2 Thermoreflectance imaging

Thermoreflectance imaging is a non-contact, optical measurement technique that detects the surface temperature variation of a sample by measuring the changes of surface reflectivity. Based on the temperature-induced optical reflectivity variations and correlating that to the temperature changes of the sample, a temperature map across the device area can be obtained. The reflectivity (*R*) of the material with normal incidence of light can be written as

$$R = \frac{(n-1)^2}{(n+1)^2}$$

where reflectivity is related to the refractive index, which is also a function of band gap and is thus correlated to the temperature of the semiconductor[112, 113].

Thermoreflectance has been successfully involved in the analysis of various electronic devices including quantum dots, quantum well lasers and other applications[114, 115]. In my experiment, DC thermoreflectance was detected by a 12-bits CCD camera. Owing to application with CCD, it is useful for generating two-dimensional profiles of temperature across the device area.

In the experiment and analysis, for a small temperature change ΔT, the relationship between ΔT and change in reflectivity ΔR is approximately linear with the equation:

$$\Delta T = \kappa^{-1} \frac{\Delta R}{R}$$

where $\frac{\Delta R}{R}$ is the thermoreflectance signal, and κ^{-1} is a proportionality constant known as the thermoreflectance coefficient. This coefficient is material and wavelength (light source) dependent, and has a value normally in the range of 10^{-3} and 10^{-6} [112, 113, 116].

For thermoreflectance signal detection (*Figure 3-8*), a sinusoidal bias signal with frequency f_1 (blue curve) is sent to the device, and the CCD camera is triggered with a $4f_1$ square wave (green) and captures the signal on each falling edge wave. Thus, four pictures are taken by the CCD camera during each cycle of device bias. A constant power LED produce a constant optical flux for sample illumination. The reflectivity variation of the device surface due to heating was captured by the CCD camera with a f_1 sinusoidal wave (red). The intensity captured by the CCD camera can be evaluated by the following equation[116]:

$$I_z = \int_a^b S(x,y,t)dt = \int_a^b \Phi R_0(x,y,t) + \Phi\Delta R(x,y,t)\cos(2\pi f_1 t + \Theta(x,y)),$$

$$\begin{array}{lll} z=1, & a=0, & b=1/4f_1 \\ z=2, & a=1/4f_1, & b=1/2f_1 \\ z=3, & a=1/2f_1, & b=3/4f_1 \\ z=4, & a=3/4f_1, & b=1/f_1 \end{array}$$

where S represent the signal captured by the CCD, R_0 and R are the reflectivities for unbiased and biased device respectively[112, 113].

By combining all the I_z equations, the temperature difference between an unbiased and a biased device can be written as:

$$\Delta T \approx \kappa^{-1}\frac{2\Delta R}{R} = \sqrt{2}\pi\frac{\sqrt{(I_1 - I_3)^2 + (I_2 - I_4)^2}}{I_1 + I_2 + I_3 + I_4}.$$

And thus, the two-dimensional temperature variation image can be obtained.

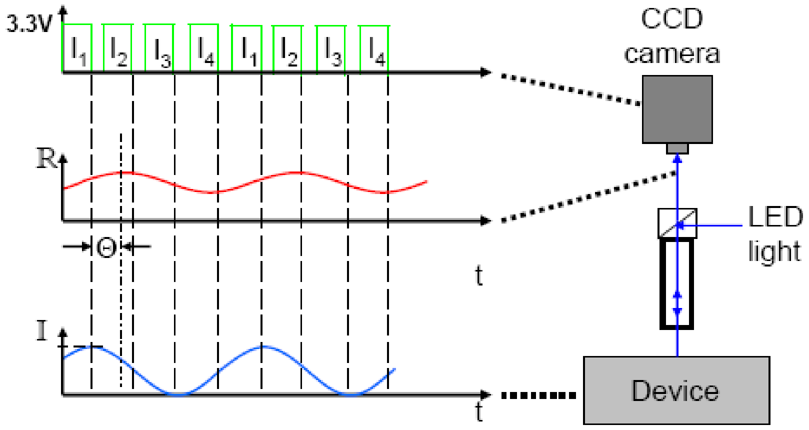

Figure 3-8 Schematic diagram of the bias signal sent to the sample (blue), CCD camera triggered by square wave (green) and the reflectance signal captured by the CCD camera (red.[116].

In my experimental setup, a 12-bit CCD camera was mounted on the microscope for capturing images. Two signal generators were connected to the device and the CCD camera, into which sinusoidal and square waves were inputted, respectively. The signal generator connected to the CCD camera was externally triggered by the signal generator connected to device, which can increase the signal-to-noise ratio. Blue LED light with 470 nm wavelength and constant power was used as a light source.

3.6 Summary

The experimental methods used in my work were discussed in this Chapter. Device fabrication by using PLD and photolithography technique was discussed, followed by structural and electrical characterization methods (*e.g.* XRD, SEM, two-, three- and four-point electrical measurements). A brief discussion of thermal measurements, micro-thermocouple and thermoreflectance imaging technique were shown in the last.

Chapter 4 Characteristics of multi-level non-volatile RRAM based on $La_{0.7}Sr_{0.3}MnO_3$

In this Chapter, $La_{0.7}Sr_{0.3}MnO_3$ (LSMO) thin film resistive switching devices are discussed. The fabrication processes, as well as structural and electrical analysis of LSMO thin films, are discussed. It is found that such samples exhibit multiple-values of resistance upon the application of different magnitudes of voltage pulses. The resistance values are well-separated and reproducible over thousands of switching cycle.

4.1 Introduction

For typical binary data storage mechanism, data should be stably stored at two states, conventionally labeled as ‘1’ or ‘0’. A more radical approach of further increasing the storage capacity in memory devices is to store more data into each single memory component, thus allowing the expansion of storage capacities without reducing the feature dimensions. For the implementation of such a multi-state memory element, it must have some intermediate states which can be reached by applying different external stimuli, and the states should be stable enough for retaining the information. Besides, such states have to be reproducible over repeated read/ write processes.

Indeed, a few studies have suggested the potential of multi-level resistive switching effect with some metastable states. Watanabe *et al.*[89], for example, applied current pulses across single crystals of Cr-doped STO and obtained clearly distinguishable resistance states. Unfortunately, their measurements have been repeated for less than 10 switching cycles only. Besides, their measurements were based on single crystals of doped STO, which is too expensive to be employed for memory applications.

A more promising approach arises from thin film-based devices, which are more compatible with the micro- or nano-electronics technology. Shang *et al.*[43], for example, presented *I-V* measurements with varying maximum ramping voltages in $La_{0.7}Ca_{0.3}MnO_3$-based top-down structures. Hysteretic *I-V* behaviour was observed in all cases, and interestingly the current ramped back to zero along different paths. The results implied that different sample resistances could be achieved, depending on the voltage previously applied across the device before measuring the resistance with a small probing voltage. Such a multi-level switching behaviour was indeed demonstrated in a recent work by the same group[44]. Similar effect has also been shown by Oligschlaeger *et al.* in a similar structure but with $Ba_{0.7}Sr_{0.3}MnO_3$ as the spacer[45]. Disappointingly, the multi-level switching behaviour was demonstrated only for tens of times in both works, failing to address the issue concerning the long-term reproducibility of the multi-state memory effect. Besides the reports were based on heterostructures with functional epitaxial oxide films grown on either metal[43, 44] or oxide[45] electrodes at elevated temperatures. Such conditions are not appropriate for industrial applications. Moreover, differences in preparation conditions can lead to variations in interface structures, film crystallography, and electronic states in different works, complicating the interpretation of results.

Here I demonstrate a multi-bit non-volatile memory structure, based on resistive switching effect in manganite thin films using a planar device geometry. By the application of suitable voltage pulses, LSMO films with photolithography-prepared Au electrodes can exhibit metastable resistive values that are reproducible for at least 10000 cycles. Repeated probing of resistances at various states suggests the durability of the structure. Such features, together with its simplicity in fabrication and compatibility with current device fabrication technologies, highlight the potential of perovskite resistive switching elements for non-volatile memory applications.

4.2 Experimental details

LSMO films were deposited on the single crystal LAO (001) substrates by PLD. In this work, the substrate temperature and oxygen pressure were maintained at 750 ℃ and 300 mTorr. The laser repetition rate was set at 5 Hz, and the thickness of LSMO films was around 300 nm. Subsequent to PLD deposition of oxides, circular gold (Au) metallic electrodes with diameter 0.8 mm and thickness 120 nm were prepared on the films by using photolithography lift-off technique. The minimum distance between the electrodes was 20 μm.

Structural and electrical analyse were performed on the samples. In the electrical measurements, aluminum wires were ultrasonically bonded on the electrodes, and a Keithley 2400 sourcemeter was used for the application of voltage signals with duration of 50 ms across the electrodes. Two-point resistance measurements were performed using the current bias mode with a direct current of 100 μA. The schematic diagram of the sample, and the corresponding circuit diagram, are shown in *Figure 4-1*.

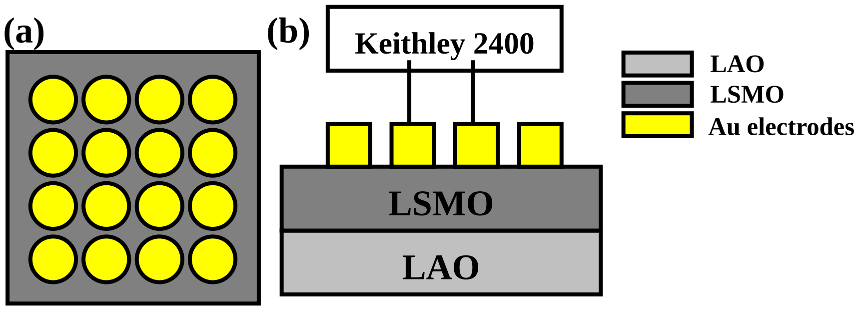

Figure 4-1 Schematic diagram of the samples (a) and set up for electrical measurements (b).

4.3 Structural analysis

Figure 4-2 depicts the θ-2θ scan of a LSMO thin film grown on a LAO (001) substrate. (00h) peaks for the substrate and the film are observed, indicating an epitaxial growth of LSMO film on LAO. The rocking curve of LSMO at the (002) peak was also scanned, showing a highly textured growth with a FWHM of 0.32° (*Figure 4-3*). Phi (ϕ) scans further confirm the epitaxial relation between the film and the substrate (*Figure 4-4*). LSMO can be treated as having a pseudo-cubic structure, and LSMO (202) and LAO (202) peaks are detected in the ϕ-scan. Both the scans of LSMO and LAO show four diffraction peaks separated by 90°, which indicates the four-fold symmetry of the structure and confirms the (pseudo-)cubic structure of both LSMO and LAO substrate. Moreover, the ϕ angles of the peaks match well together, which indicates that the LSMO thin film was grown cube-on-cube on the LAO substrate.

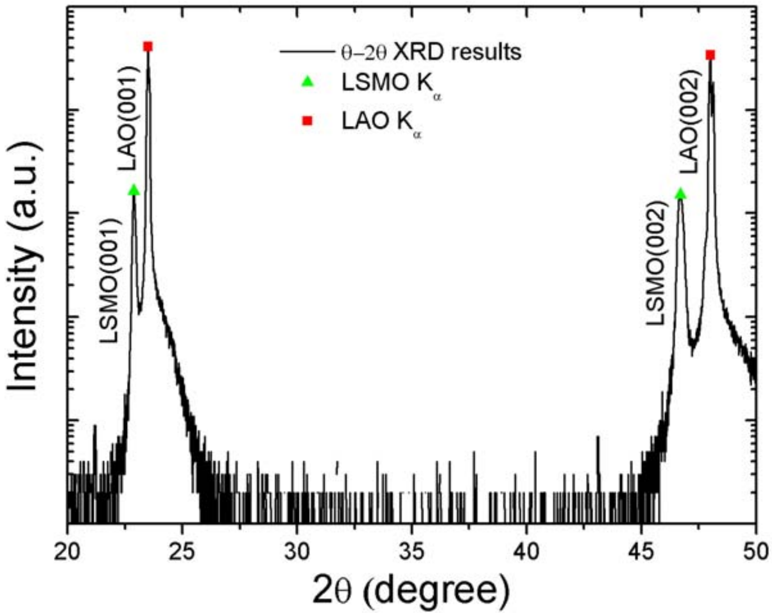

Figure 4-2 XRD θ-2θ scan of a LSMO film deposited on LAO (001) substrate.

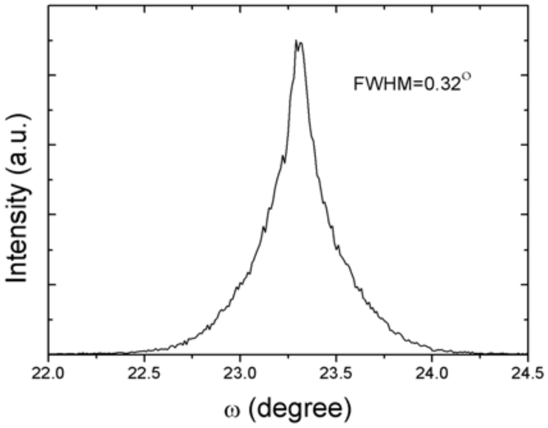

Figure 4-3 XRD rocking curve of LSMO (002) peak.

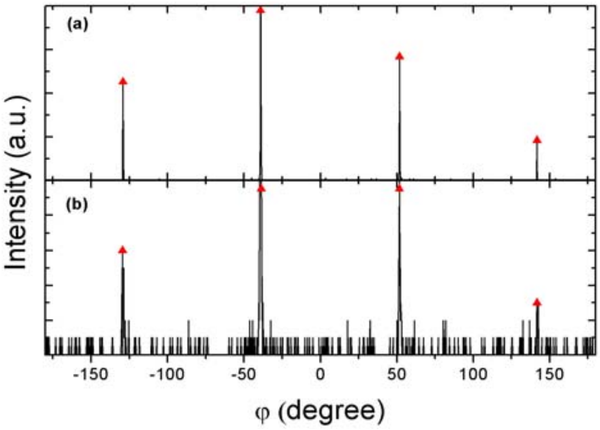

Figure 4-4 Phi scan of (a) LAO (202) and (b) LSMO (202) planes.

4.4 Electrical characterization

4.4.1 *I-V* characteristics

Figure 4-5 shows the *I-V* characteristics of the sample before and after forming. When the voltage is initially ramped, the sample is kept in the conducting state with a resistance around 300 Ω (Path 1-2). When the voltage is ramped back from -13 V to zero, the resistance of the sample suddenly increases from 300 Ω to the order of 20-30 kΩ (Path 3). This sudden increase of resistance phenomena is the forming process and it didn't affect other neighbor devices. After that, the resistance of the sample is kept at the same order and does not switch back to its initial state, no matter how high a voltage is applied (Path 4-7).

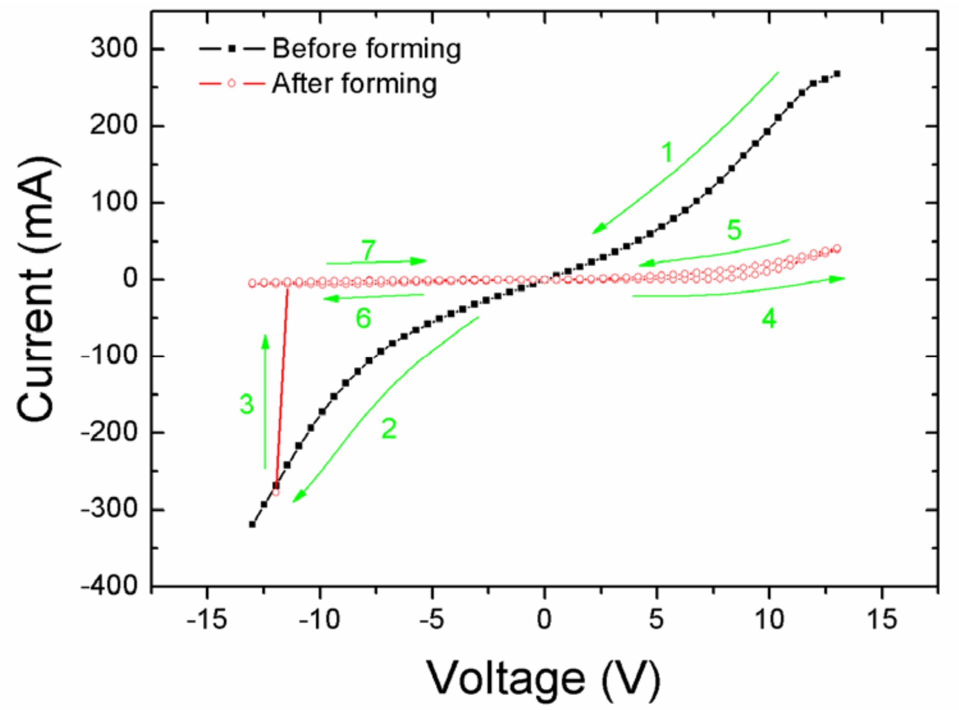

Figure 4-5 I-V characteristics of LSMO sample before (black) and after forming (red).

After forming, a clear hysteretic asymmetric *I-V* behaviour is observed, which is similar to the typical binary switching behaviour reported in other systems[43, 89, 117].The *I-V* characteristic of the sample after forming (red curve in *Figure 4-5*) is shown in the expanded scale *Figure 4-6*. As the voltage across the electrodes increases from zero (branch 1), the slope of the *I-V* plot was fairly gentle until around 10 V, at which the slope of the curve (i.e. differential conductance of the sample) suddenly increases. The voltage is subsequently ramped down to zero (branch 2). Note that the current across the sample retains a higher value compared to that of branch 1, suggesting a decrease in the sample resistance. When the voltage is dropped below -12 V (branch 3), the magnitude of current across the sample suddenly decreases. The current value then retains at a relatively small value, which implies a higher resistance when the voltage is ramped back to zero (branch 4).

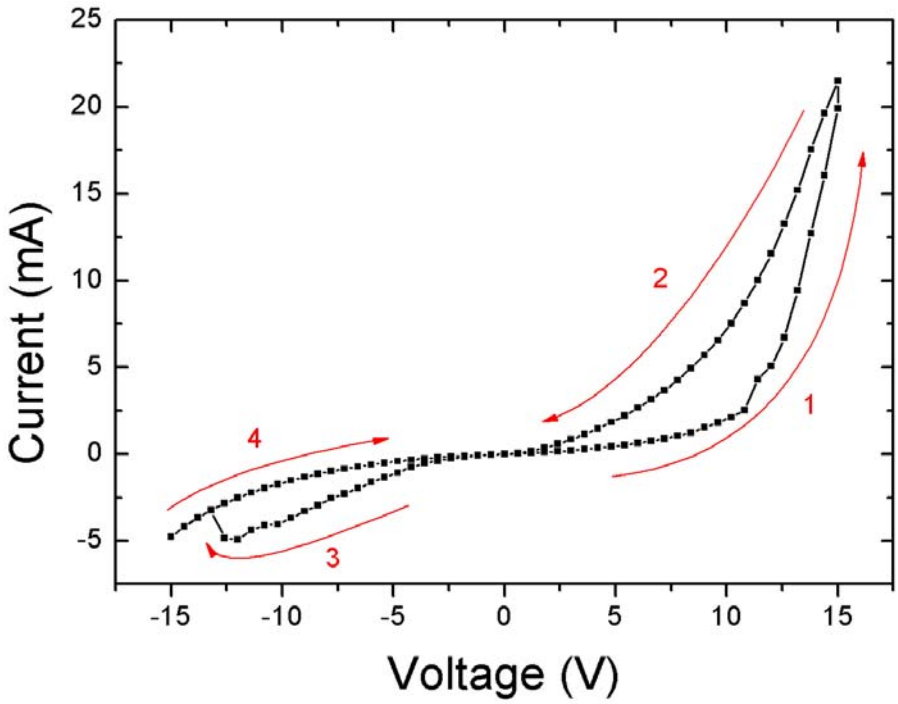

Figure 4-6 I-V characteristics of a LSMO switching device after the forming process.

From the hysteretic behaviour of the *I-V* characteristic, especially on the positive voltage bias, a continuously and gradual increment of current is observed when the voltage bias is increased. Thus it would be expected that “minor loops” of *I-V* plots in the positive voltage bias region can yield hysteretic behaviour similar to the full loop (i.e. *I-V* scan between +15 and -15 V). Such minor loops can be obtained by ramping the voltage between a fixed negative voltage V_- and various positive voltage values V_+. The schematic of the ramp function is plotted in the inset of *Figure 4-7.* In *Figure 4-7*, V_- is set at -15 V and V_+ varies from +8 V to +15 V. V- was set at -15 V for two reasons. From the observation of the previous *I-V* characteristics, while a sudden increase of resistance of the sample at around -12 V, no difference in sample resistances can be observed by the driving voltage below -15 V. Moreover, it is a precautionary measure to set the voltage limit at 15 V to avoid unrecoverable sample damages.

To ensure identical starting conditions for the samples during minor loop measurements, samples were first pulsed at -15 V before *I-V* minor loops were extracted. The *I-V* characteristics were then measured with the voltage sweeping cycle 0 V→ V_+→ 0 V→ V_-→ 0 V. Selected *I-V* curves with different V_+ values are shown in a semi-log plot in *Figure 4-7*. Here we focus only on the positive regions of the *I-V* curves. As long as V_+ does not exceed 8 V, the *I-V* plots are completely reversible, and branches 1 and 2 basically overlap on each other. Starting from V_+=10 V onward, hysteresis sets in at both positive and negative branches of the plot. It should be mentioned that branches 1 of all *I-V* minor loops basically followed the same path. This suggests that the samples were starting from the same conditions at the beginning of the experiment, which was caused by the application of the -15 V "reset" voltage.

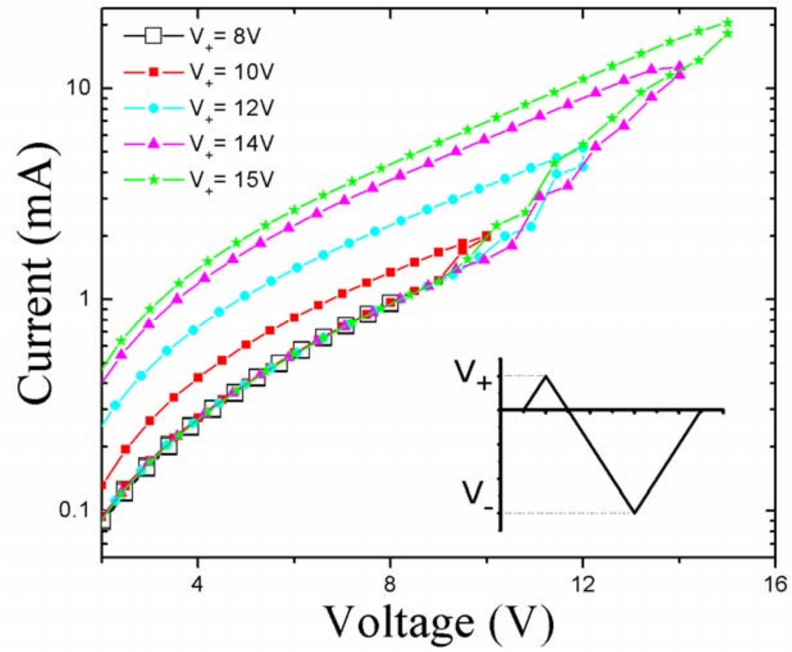

Figure 4-7 Semi-log plot of minor loop I-V curves in the positive voltage region. Inset shows the corresponding voltage ramp profile.

4.4.2 Resistance switching measurements

On the other hand, deviation can be observed along branch 2 of the *I-V* curves, as the applied voltage returned to zero. As mentioned before, this result implies that multiple resistance values can be obtained from the same sample, depending only on the V_+ value previously applied. This is illustrated in the resistance switching measurement in *Figure 4-8(a)*. In this particular measurement, voltage pulses of specific values (as labeled on the graph) were applied across the electrodes, followed by resistance probing of the sample with a constant current of 100 μA which corresponding to a voltage less than 3 V; such a small voltage was not sufficient to switch the device. From the observation, a minimum resistance value is obtained after a +15 V pulse is applied. However, as V_+ decreases, the resistance of the sample gradually increases to a maximum of about 9 V; this high resistance state can also be obtained by directly "resetting" the sample with a -15 V pulse, as explained previously. Therefore, for multi-level resistance states, only V_+ larger than 9 V can be used as memory.

I also examined the response of the sample by resetting the device with +15 V pulses, following by the application of varying negative voltage signals. The results are shown in *Figure 4-8(b)*. As seem in the figure, the resistance change could only take place if the negative pulse is larger than -12 V. More importantly, the maximum resistance is reached as the voltage reaches -14 V. By comparison, in the negative side, it is not very desirable for manifesting the multiple resistive states due to its narrow switching voltage.

I also tested the stability of resistance in the device by the initially -15 V pulses, and then followed by the application of the positive voltage pulses with the sequence of +1 V→+2 V→…→+15 V→+14 V→…→+1 V. The result in *Figure 4-9* shows that metastable low resistance state can switch to a lower resistance state with larger V_+. However, it cannot switch back to the previous resistance value by pulsing the sample with a smaller V_+, unless V_- (-15 V) is applied.

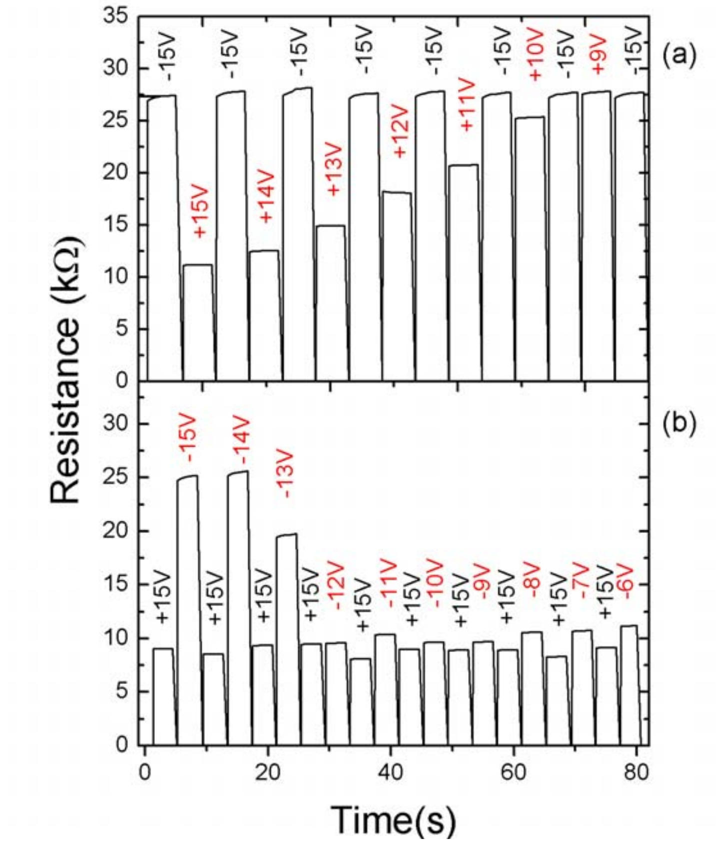

Figure 4-8 Resistance of a device after the application of varying voltage pulses. Voltage pulses applied are as labeled in the Figure. (a) Cycling between -15 V and varying positive voltages. (b)Cycling between +15 V and varying negative voltages.

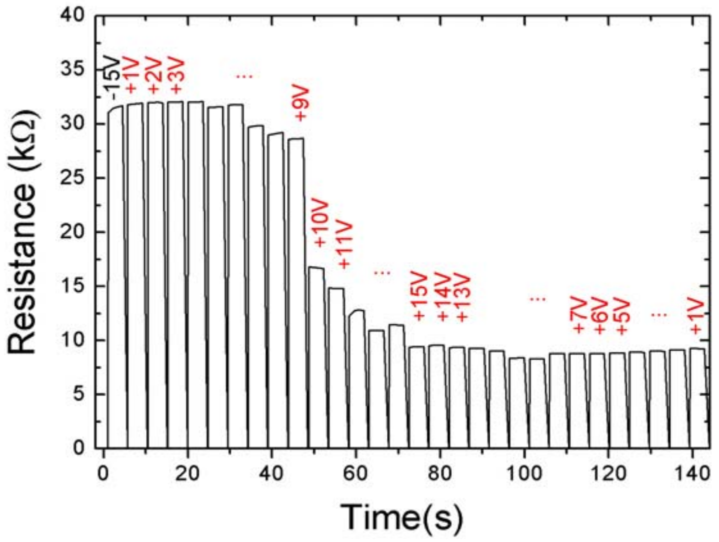

Figure 4-9 Resistance of different positive voltage pulse after -15 V pulse.

From the results in *Figure 4-8 and 4-9*, it can be seen that the resistance level of a sample can be determined by the magnitude of positive voltage pulse previously applied. Indeed, one can arbitrarily determine the number of intermediate resistance states that can be obtained in such kind of resistive switching elements, subjected to a number of limitations. Two of the crucial issues need to be addressed when deciding the number of possible states include the reproducibility of each single state, and the stability of individual states upon repeated measurements.

4.4.3 Reproducibility and stability measurements

Reproducibility and stability measurements were performed on a Au/LSMO/Au device at room temperature. For the reproducibility test, we subjected a sample to a series of repeated pulses for 10000 cycles with the following pulse pattern: -15 V→ +11 V→ -15 V→ +12 V. After the application of each pulse, the resistance of the sample was probed with a current of 100 μA. In *Figure 4-10*, we can see that various resistance states are well separated from each other. While there are only three separate states in this run, more resistive states can be obtained by the application of suitable voltages. The fluctuation of resistances from the mean value is minimal, illustrating the (short-term) repeatability of the states. However, an undesirable feature, as observed from the figure, is the continuous rise in the resistance of the low state with the continuous application of pulses.

Furthermore, I also tested the stability of the sample upon prolonged probing of resistance, which is shown in *Figure 4-11*. The resistances seem to be fairly stable over 30 minutes of continuous measurements. While there was a trend for the resistance reset state to increase with time, various resistance states were definitely well separated from one another. Although both the reproducibility and stability tests show that the devices are still far from ready for commercial applications, the results suggested the possibility of repeatable and stable memory state in a single device. More tests should be conducted on such memory devices.

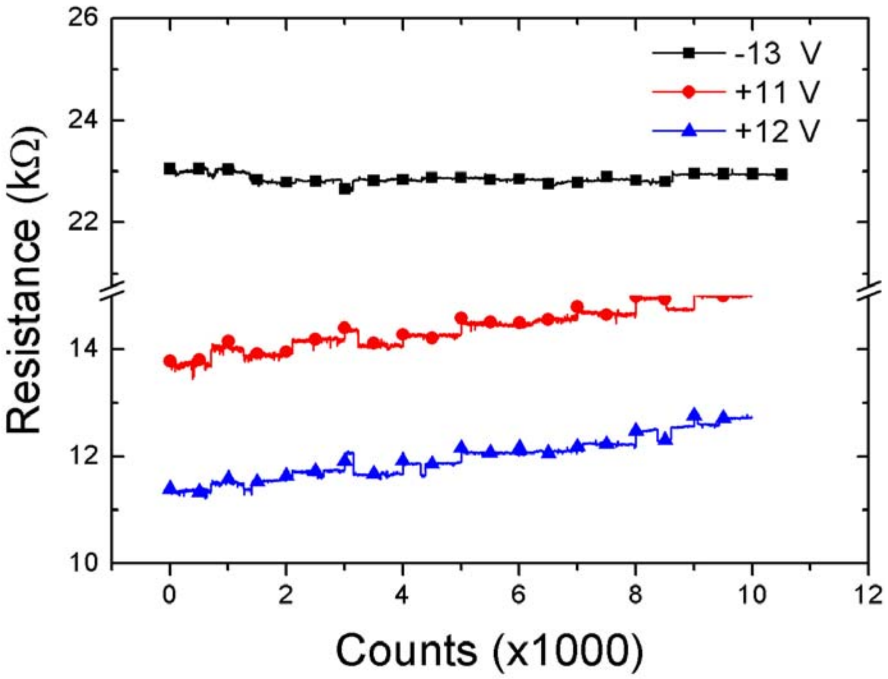

Figure 4-10 Reproducibility of the sample with repeated cycling of voltage sequence: -15 V→ +11 V→ -15 V→ +12 V.

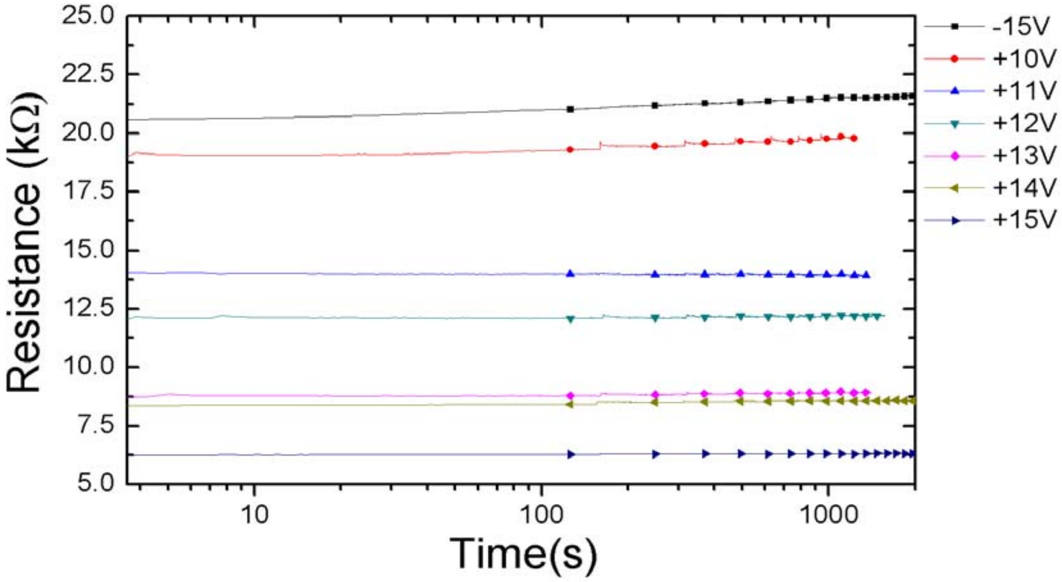

Figure 4-11 Stability of the resistance states after pulsing at specific voltages.

4.5 Discussion

Base on the experiment results, it can be seen that there are two possible ways to switch the devices between LRS and HRS. A large positive pulse can be used to drive the element to an intermediate resistance state. If the data need to be re-written, a large negative reset pulse can be applied to switch the element back to the HRS and followed by a suitable positive writing pulse. Another possible way to write the data is overwrite the previous data with a large positive pulse. According to the previous results, the resistance of the element can be further reduced by subjecting the device to a positive pulse with magnitude larger than that applied previous to the sample. Instead of resetting with a negative pulse and then writing with a positive pulse, the second scheme allows a lower resistance memory states to be achieved with less switching time and power. On the other hand, re-writing of the device to higher resistance values can be reliably achieved only through the first scheme.

4.6 Conclusion

To summarize, the use of thin film resistive switching Au/LSMO/Au elements for multi-state nonvolatile memory structures, based on planar measurement geometry, is proposed. The simplicity of the setup, both in terms of sample preparations and switching processes, should prove a great advantage for adoption into the current microelectronics technology. Repeated switching over 10,000 times among different resistance levels has been demonstrated, close to some existing multiple switching memory technologies. Moreover, in the current case, the negative voltage is acting simply as a reset mechanism. Although some of the further measurements are needed to fulfill commercial applications, this structure, LSMO with Au electrodes is one of the choices for multi-bit non-volatile memory devices.

Chapter 5 Resistive switching properties of epitaxial $Pr_{0.7}Ca_{0.3}MnO_3$ thin films with different metal electrodes

5.1 Introduction

As mentioned before, there are many different combinations of insulating films, electrode materials and measurement geometries that have exhibited resistive switching effect. For example, Kim *et al.*[73] showed that PCMO top-down geometry samples with Au top electrodes and Pt-coated Si as bottom electrodes did not show resistive switching effect. However, at the same time, Lee *et al.*[118] and Kim *et al.*[105] measured samples with similar geometry and obtained resistive switching effect. Moreover, Fujimoto *et al.*[102] showed resistive switching effect in Pt/PCMO/Pt/SiO_2 top-down devices with a resistance change by an order of magnitude with a voltage of 3 V, where Kim *et al.*[73] did not obtain any switching up to 4 V.

Most of scientists propose that resistive switching effect mainly from the interface between the oxide thin films and the metal electrodes, but the variation of results made it hard to reach a conclusion. It is worthy to perform a more systematic investigation on the electrode dependence of resistive switching effect. Tsubouchi *et al.*[48], for example, deposited different metal electrodes (Mg, Ag, Al, Ti, Au, Ni and Pt) on PCMO thin films and investigated the metal electrodes dependence of resistive switching effect. However, the result is hard to be compared directly because the distance of electrode pairs were different. Therefore, their results cannot eliminate the influence of electrodes separation difference on switching ratio.

In order to be systematic in comparing and determining the dependence of metal electrodes on resistive switching effect, and to have a better understanding about the mechanism of resistive switching, different metal electrodes were deposited on PCMO thin films with the same electrode separation. It is hoped that a good comparison can be obtained among different metal electrodes.

5.2 Experimental details

Thick (250 nm) epitaxial films of PCMO were grown on LAO (001) substrates by PLD. During deposition, substrates were maintained at 650 ℃, and an oxygen pressure of 150 mTorr with 8 mTorr chamber base pressure was applied. The laser pulse energy was around 250 mJ, with a repetition rate of 5 Hz. After deposition, the films were cooled down to room temperature at a rate of 10 ℃min^{-1} under the same oxygen pressure.

After deposition of oxide films, metal electrodes of diameter 0.4 mm were prepared by lift-off technique. All metal electrodes, Ti, Pt, Au and Al electrodes were prepared by PLD. The minimum distance between pairs of electrodes was 0.03 mm. and the thickness of the metal electrodes were 100 nm.

Structural analysis was done by XRD, and electrical measurements (*I-V* characteristics and resistance switching measurements) were performed with a Keithley 2400 at room temperature. *Figure 5-1* shows the layout of electrodes on sample surfaces and the measurement setup. All of the measurements, unless specified, were performed on electrodes pairs (1-I) which were nearest neighbors.

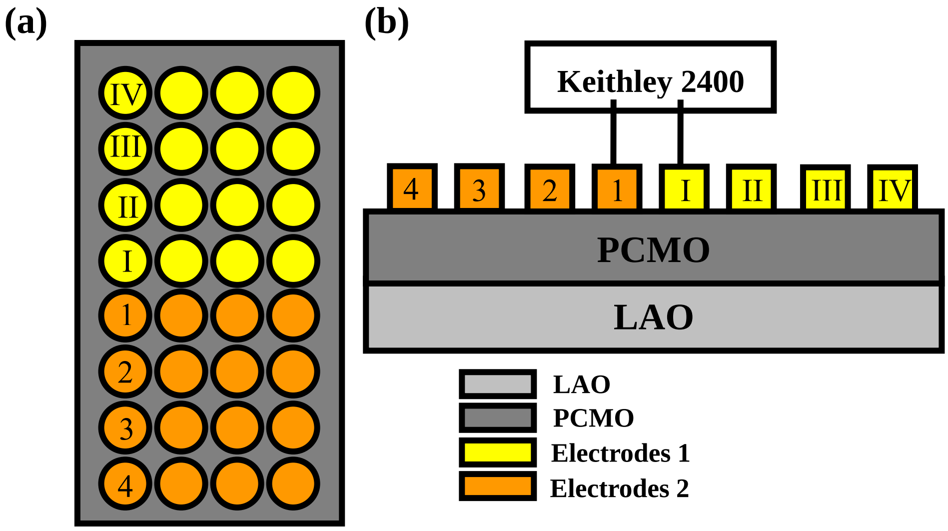

Figure 5-1 *Schematic diagram of (a) the electrode geometry, (b) measurement setup. Each sample has 2 different type of electrodes (orange and yellow).*

5.3 Structural analysis

Figure 5-2 shows the *θ-2θ* scan profile of a PCMO film on LAO substrate. The PCMO thin film was single-phased and highly c-axis oriented, with a strong PCMO (002) peak next to the LAO (002) substrate peak. The FWHM of the rocking curve was 0.67°, indicating a highly-textured growth of the film (*Figure 5-3*). *ϕ*-scan (*Figure 5-4)* on the film confirmed that the PCMO film was grown cube-on-cube on the LAO substrate.

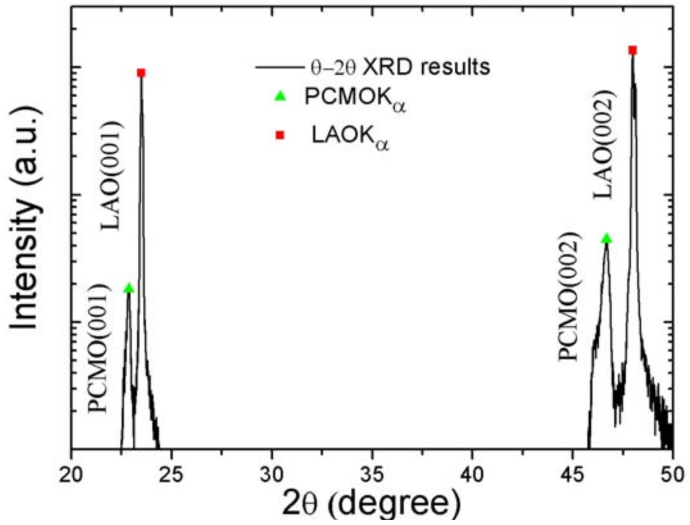

Figure 5-2 XRD θ-2θ scan of a PCMO film deposited on LAO (001) substrate.

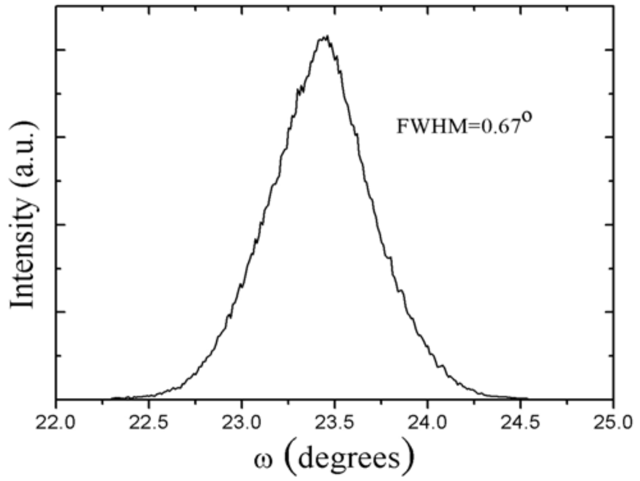

Figure 5-3 XRD rocking curve of PCMO (002) peak.

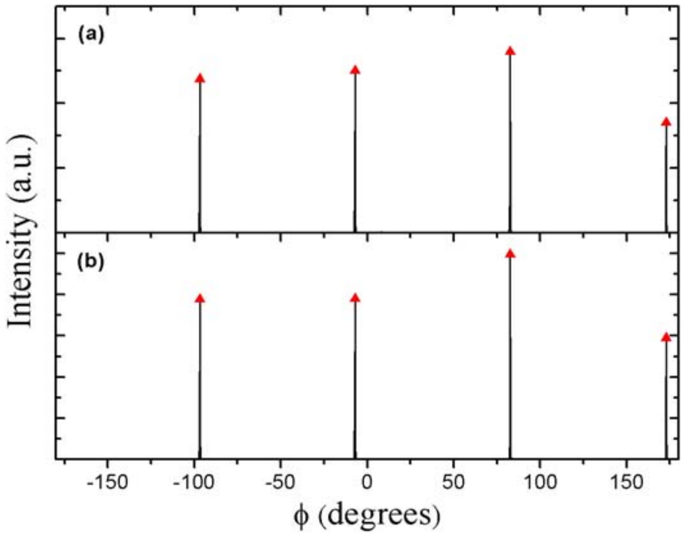

Figure 5-4 Phi scan of (a) LAO (202) and (b) PCMO (202) planes.

5.4 Electrical characterization

5.4.1 *I-V* characteristics and resistive switching measurements with minimum electrodes separation of 0.03 mm

Figure 5-5 shows the *I-V* characteristics of a PCMO thin film, with Al electrode on one side and four different types of metal electrodes (Al, Ti, Au and Pt) on the other. In these samples, no forming processes were performed, and the *I-V* characteristics were obtained by two-point measurements. A positive bias is defined as the current flowing from the Al electrode to other electrode. During the *I-V* measurements, the bias voltage across the electrodes was scanned in a sequence 0→ $+V_{max}$→ 0→ $-V_{max}$→ 0.

As shown in *Figure 5-5*, all *I-V* characteristics show non-Ohmic behaviour. Interestingly, clear hysteretic and asymmetric *I-V* behaviour is observed in Al-Ti, Al-Pt and Al-Au electrode pairs. As the voltage across the electrodes increases from zero, the slopes of all *I-V* plots are fairly gentle, representing high resistance values for all samples. When the voltage is subsequently ramped down to zero, the returning curves basically overlap with plots for rising voltage.

In the small negative voltage bias region, the plots are nearly symmetrical with the positive voltage branch when the voltage drops from zero. However, when the voltage reaches around -7.5 V, the currents across the samples suddenly increase, which stay at relatively large values when the voltage ramps back to zero. This indicates that a low resistance state is reached by the samples when a large negative voltage is applied. For the sample with two Al electrodes, nearly symmetric *I-V* behaviour is observed, and a relatively small hysteretic loop is shown in the negative voltage bias regime.

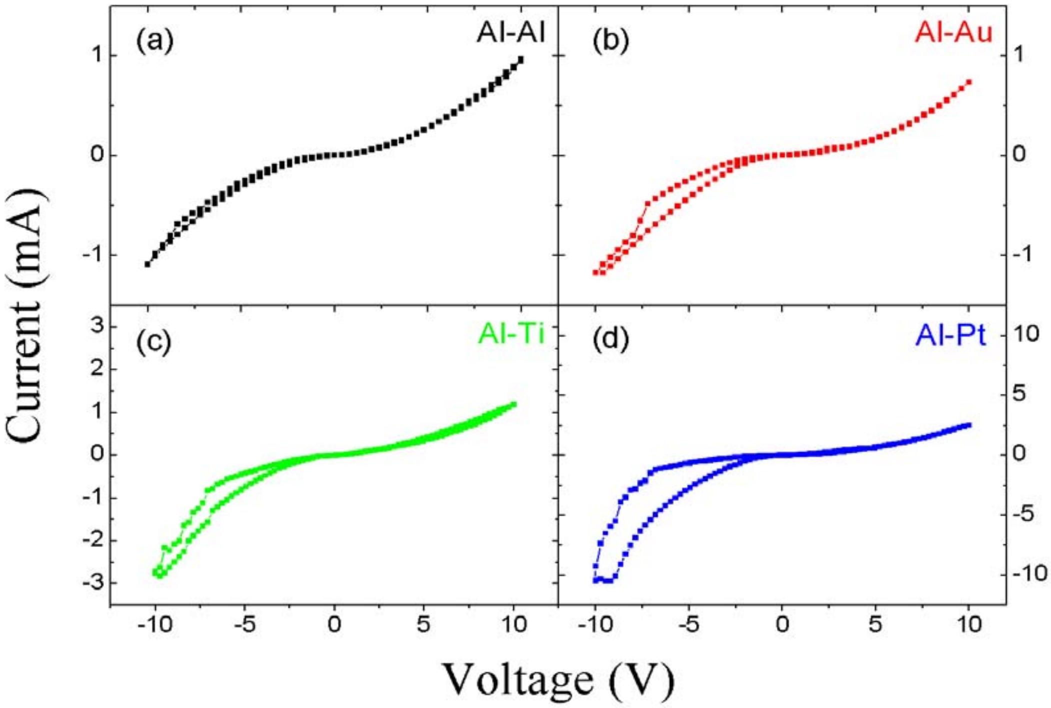

Figure 5-5 I-V characteristics of Al/ PCMO/ M structure, where M=Al (a), Au (b), Ti (c) and Pt (d).

Resistance switching measurements were performed with the circuit shown in *Figure 5-1*. After applying two pulses at -10 V for 1 ms, the sample resistance was measured with a bias of -2 V. Subsequently, two +10 V pulses were applied to switch the sample back to the high resistance state, and the resistance was measured again. To avoid damaging the samples and yet to ensure the reproducibility of resistive switching effect, ±10 V was chosen as the switching voltage. Two consecutive pulses were applied before resistance probing, as this yielded more reproducible switching behaviour at low and high resistance states. The -2 V probing voltage was applied for more observable resistive switching effect.

Changes in sample resistances, after the application of voltage pulses, are displayed in *Figure 5-6*. Before voltage pulses are applied, all the samples exhibit high resistance values. Applications of negative pulses causes the samples to switching from high (23-60 kΩ) to low (8-30 kΩ) resistance states; the exact resistance value depends on the combinations of metal electrodes. The largest switching ratio [($R_{high} - R_{low}$)/R_{low}] of over 90% is obtained for Al-Au, compared with 75% for Al-Pt and 23 % for Al-Ti electrode combinations. For Al-Al structure, although only a minute hysteretic *I-V* behaviour was observed, a 26% of resistance switching ratio was obtained. However, due to the small difference between high and low resistance states in Al-Al electrode samples, the actual effect of resistive changes was masked by the fluctuations (±13 %) in resistance measurements, rendering it difficult to obtain a stable resistance switching effect.

In terms of reproducibility of resistance switching, all of the samples showed clear separation between high and low resistance states except Al-Al. There is a distribution of the switching ratio in different samples with the same geometry. However, the switching voltage shows little variations and the fluctuations in the switching ratios is around 10% of the mean values.

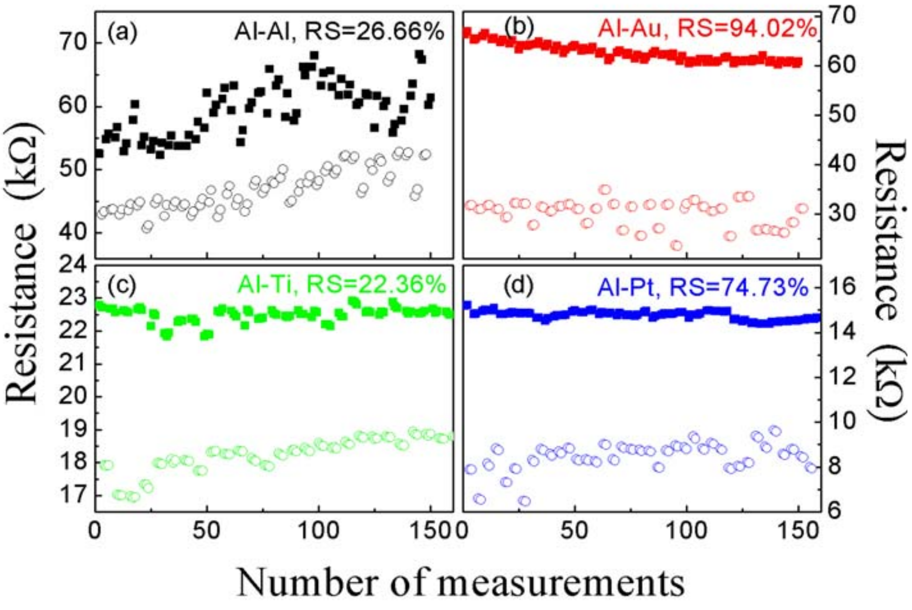

Figure 5-6 Resistance switching measurements of Al/PCMO/M structure, where M= Al(a), Au(b), Ti(c) and Pt(d). RS represents resistance switching ratio, open circles correspond to LRS, and solid squares to HRS.

In order to fully investigate the dependence of metal electrodes on the switching behaviour, *I-V* characteristics for samples with other combinations of metal electrodes (Ti, Au and Pt) were measured in the two-point geometry. *Figure 5-7* shows the *I-V* characteristics of M1/PCMO/M2 structure, where M1, M2= Ti, Au or Pt. For Pt-Pt and Au-Au structures (*Figure* 5.7(b)), the *I-V* characteristics show Ohmic behaviour. Besides, the measured resistances for samples with Pt-Pt and Au-Au electrodes were the smallest among all the measurements. For the rest of the electrode combinations, nonlinear but symmetric plots were observed, and all of the *I-V* characteristics were reversible and non-hysteretic on both the positive and negative voltage regimes. During *I-V* measurements, a 10-mA current compliance was set to avoid damages to the samples. Therefore, when the current was larger than 10 mA, a horizontal line was observed in the *I-V* characteristic curves. Moreover, these structures did not have any resistance switching behaviour, at low measuring voltage (-2 V) used in measurements, the curves of ramping up and down were almost overlapping one another, with minute hysteresis that could probably arise from Joule heating. In summary, only samples with Al electrodes showed resistance switching behaviour.

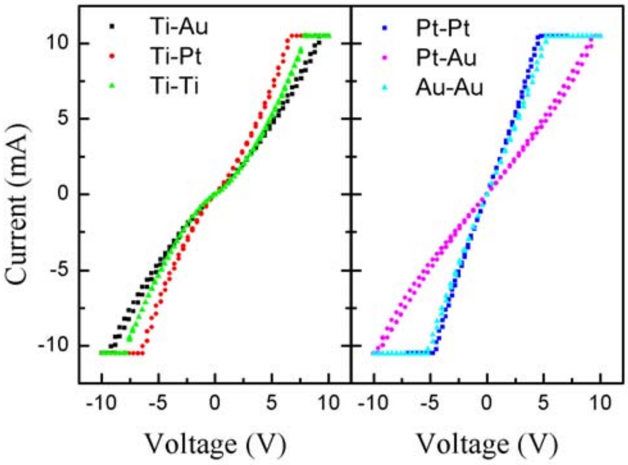

Figure 5-7 I-V characteristics of M1/PCMO/M2 structure, where M1, M2=Ti, Au and Pt.

5.4.2 *I-V* characteristics and resistive switching measurements with different electrode separation

Apart from the general *I-V* measurements, I also performed *I-V* and resistance switching measurements for electrodes with varying separation. During measurements, a certain Al electrode was used, and the electrodes with varying distances from this Al electrode were used as the counter electrodes. The schematic diagram of the sample is already shown in *Figure 5-1*, and the electrode combinations followed the numbers in the figure (for example electrode I with electrodes 1, 2, 3, 4). An example of measurement on Al/PCMO/Ti structure is shown in *Figure 5-8*. As the electrode separation increases, the maximum current passing through the sample can be seen to reduce greatly, and the hysteretic loops on the negative voltage side shrink with increasing electrode separation from 0.03 mm to 1.32 mm.

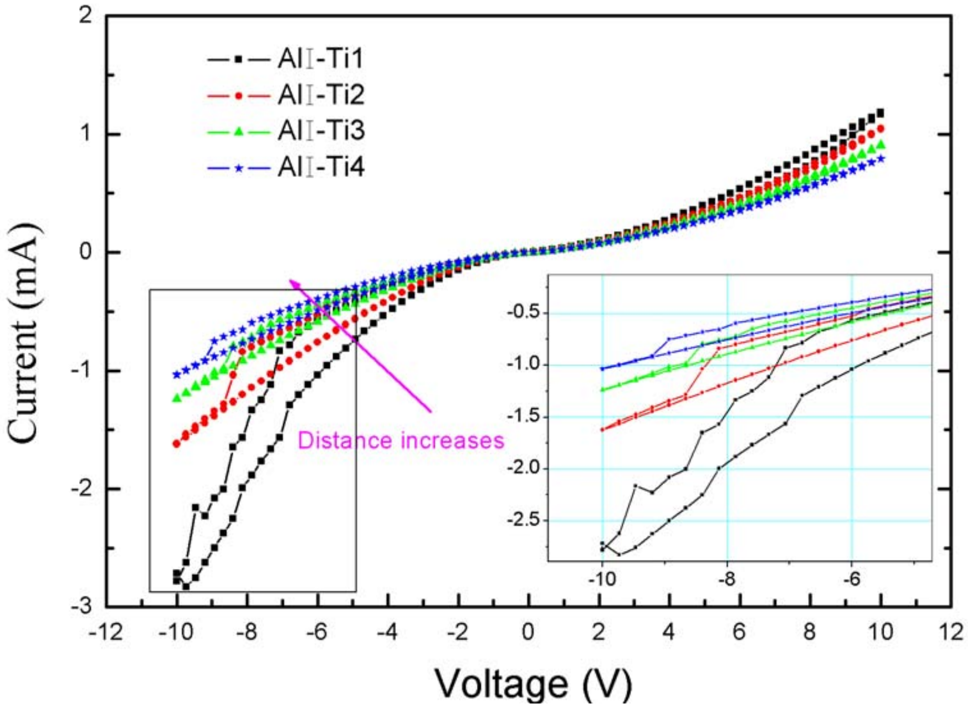

Figure 5-8 I-V characteristics of Al/PCMO/Ti structure, where the separation between electrodes is 0.03 mm (black), 0.46 mm (red), 0.89 mm (green) and 1.32 mm (blue), respectively. The inset highlight the curves at the large negative bias region.

In resistance switching measurements, when the electrode separation becomes large, the resistance of the Al/PCMO/Ti structure increases (*Figure 5-9*). However, the resistance change did not seem to be proportional to the distance between electrodes. This result indicates that the interfacial resistance makes a significant contribution. The resistance switching ratio reduces from 23% to less than 10%, when the Al-Ti separation increases from 0.03 mm to 1.32 mm. Furthermore, according to the results, the resistance values at LRS increases with rising electrode separation, and the fluctuation of low resistance values is larger compared with samples with small electrode separation. These may be related to the electric field across the electrodes. The summary of lower resistance values, resistance differences and the switching ratio against electrode separations are plotted in *Figure 5-10*

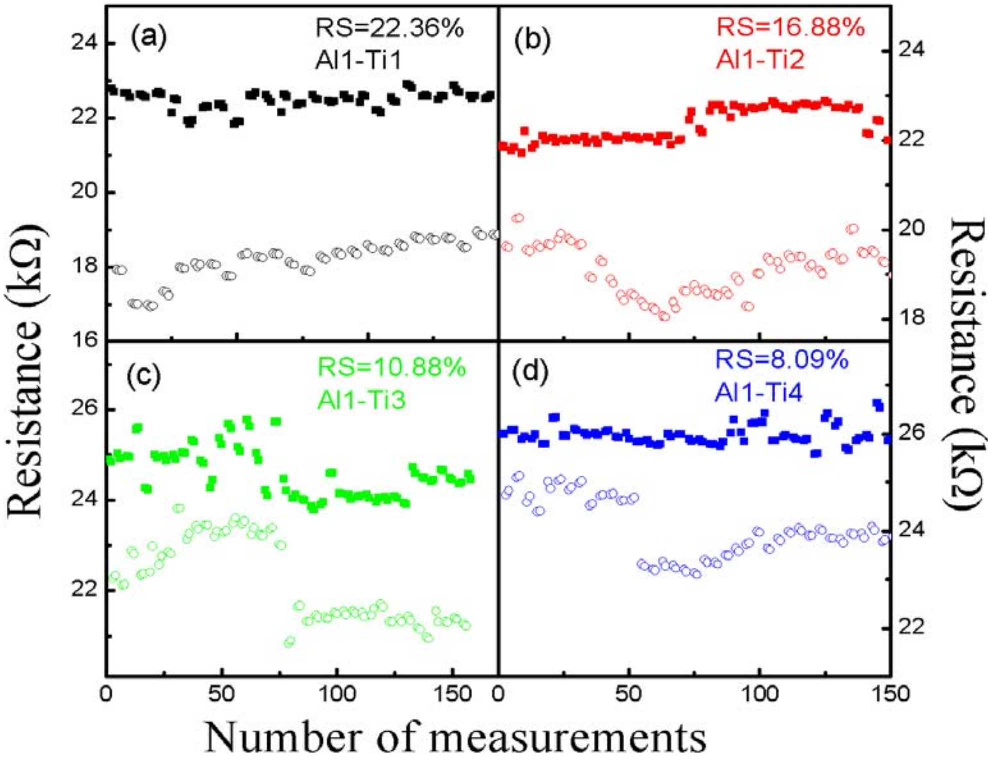

Figure 5-9 Resistance switching measurements of Al/PCMO/Ti structure, with electrode separation of 0.03 mm (a), 0.46 mm (b), 0.89 mm (c) and 1.32 mm (d), respectively. Solid and open circle represent HRS and LRS.

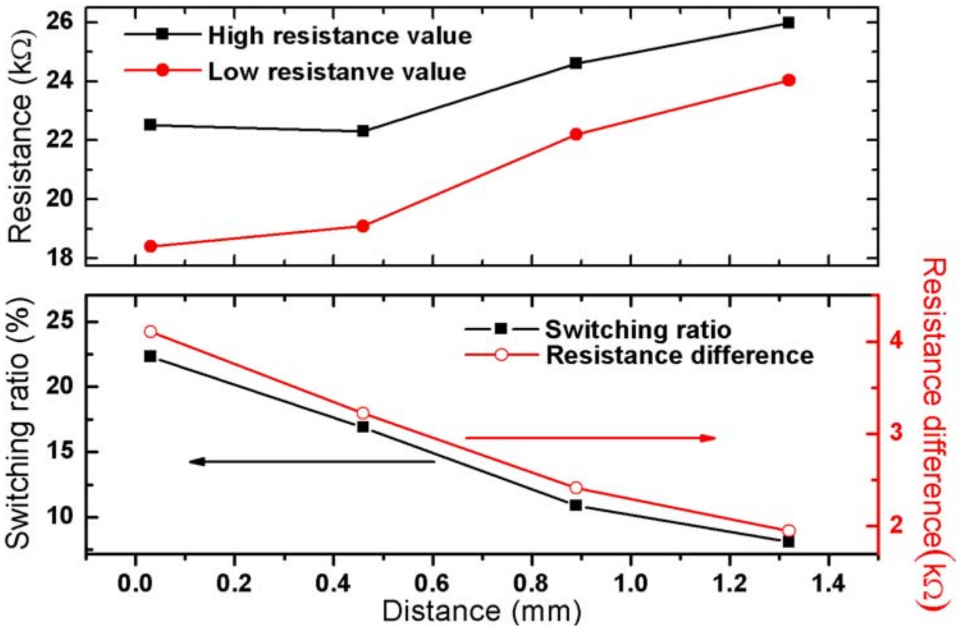

Figure 5-10 Summary of high and low state resistances (a); resistance differences and the resistive switching ration (b) against electrode separation, for Al/PCMO/Ti sample structure.

5.4.3 Four-point measurements

Four-point measurements were also performed, with a maximum bias current of 1-mA. The measurement could eliminate the influences of contact resistances, thus shedding light on the relative contributions of the bulk and interface of the oxide film on the switching effect. The choice of 1 mA as the maximum bias current was to prevent potential damages the sample. *Figure 5-11* shows the *I-V* characteristics of an Al/PCMO/Ti structure, measured with two-point and four-point probe geometries. Ohmic characteristics, and no resistance switching behaviour, can be observed in four-point measurement. The resistance of the PCMO thin film is around 2 kΩ across nearest electrodes, which is small compared with the total resistance of the sample (23 kΩ) obtained from the two-point measurements. The small value of the PCMO resistance cannot explain the 4-kΩ resistance reduction during switching. These observations clearly indicate that the resistance switching phenomenon occurs near the Al/PCMO interface.

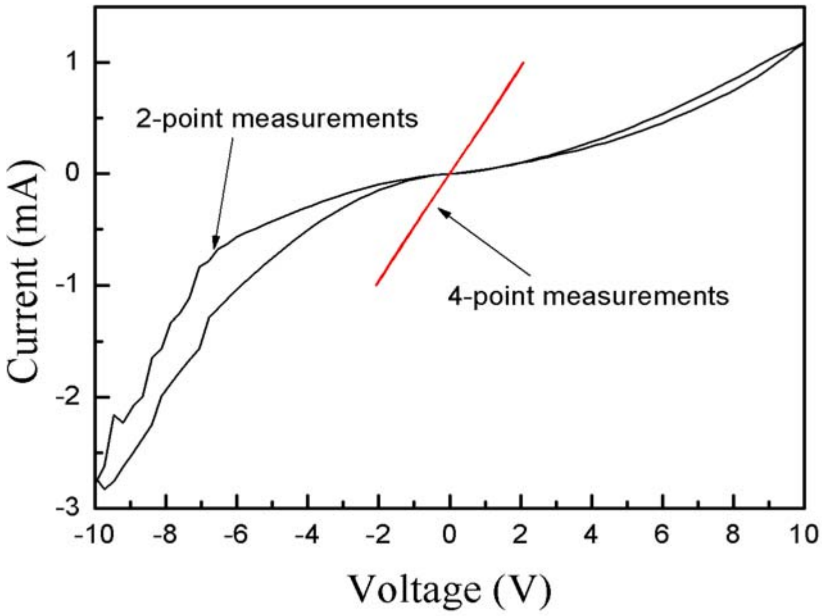

Figure 5-11 Two-point and four-point I-V characteristics of Al/PCMO/Ti.

5.5 Discussions

According to the nonlinear and asymmetric *I-V* characteristics of Al/PCMO/M structures, it is postulated that Schottky contacts is a possible origin for the resistance changes[48]. PCMO can be considered as a p-type semiconductor, in which Ca^{2+} ions are doped into Pr^{3+} ions sites and generate extra holes. Oxide vacancies can act as the hole transporting media. At the metal/oxide interface, a Schottky barrier can be formed. The most possible current transport mechanism across the Schottky barrier is based on hole injection from the metal to the oxide layer.

P-type PCMO forms Schottky barriers with metallic electrodes[49, 119]. For p-type Schottky contacts, when the work function of the metal decreases, the barrier height for hole conduction increases, and the interface resistance between the metal and PCMO increases. The electron affinity of PCMO film is 4.9 eV, and the work functions of Al, Ti, Au an Pt are 4.28, 4.33, 5.1 and 5.65 eV, respectively[120]. According to the experimental results, the largest barrier height is observed in

Al/PCMO interface and the lowest in Pt/PCMO. Thus, maximum and minimum resistances are obtained in these two cases. When Al electrode was replaced by Pt or Au metal electrodes, due to the high work functions of Pt and Au compared with the electrode affinity of PCMO, positive charges can be transported easily and thus the smallest resistance value were obtained with both Pt or Au electrodes in all cases.

According to the above analysis, it seems that only samples with Al metal electrodes can exhibit hysteretic behaviour and resistance switching effect[24]. However, Ti has almost the same work function as Al, but surprisingly no resistance switching was observed in Ti/PCMO interface. From that observation, it seems that Schottky barrier is not sufficient to explain the resistive switching effect.

Moreover, it should be noted that Al is an electrochemically active metal, in which the atoms are more prone to charge migration[39, 121]. Owing to this, the Al/PCMO interfaces should also play a role on resistive switching. However, further investigations are needed to fully understand the mechanism. Such investigations are discussed Chapter 7.

5.6 Characteristic of EPIR switching effect

For commercial memory devices, low power requirements, fast write and erase times, and good reliability (including reproducibility and excellent data retention) are some of the basic requirements. In order to investigate the suitability of resistive switching phenomenon in PCMO-based devices for potential memory applications, pulse width dependence of switching ratios, as well as endurance and retention experiments, were performed in the PCMO switching devices.

5.6.1 Pulse width dependence of PCMO switching device

Since the resistive switching ratio depends on both the pulse magnitude and the pulse width, desirable switching performances can be tested by performing pulse width- and magnitude-dependence tests. *Figure 5-12* shows the switching ratio dependence on the pulse width. The experimental setup was shown in *Figure 3-4(c)*, and a -2 V probing voltage was used to measure the resistance. In order to increase the switching ratio, a large voltage pulse magnitude of -21 V was set. The switching ratio was measured by progressively increasing the pulse width, so to prevent any damages and influence on the device performance. Assuming that 100% of switching ratio is reached for -21 V with 1 ms pulse width, it can be seen that when the pulse width reduces, the resistive switching ratio also decreases. Switching effect is absent when the pulse width is less than 100 ns. The result shows a log-linear relationship between the pulse width and the switching ratio. It should be noted that the switching ratio has not reached saturation at a pulse duration of 1 ms, and it actually increases with further increase in the pulse width.

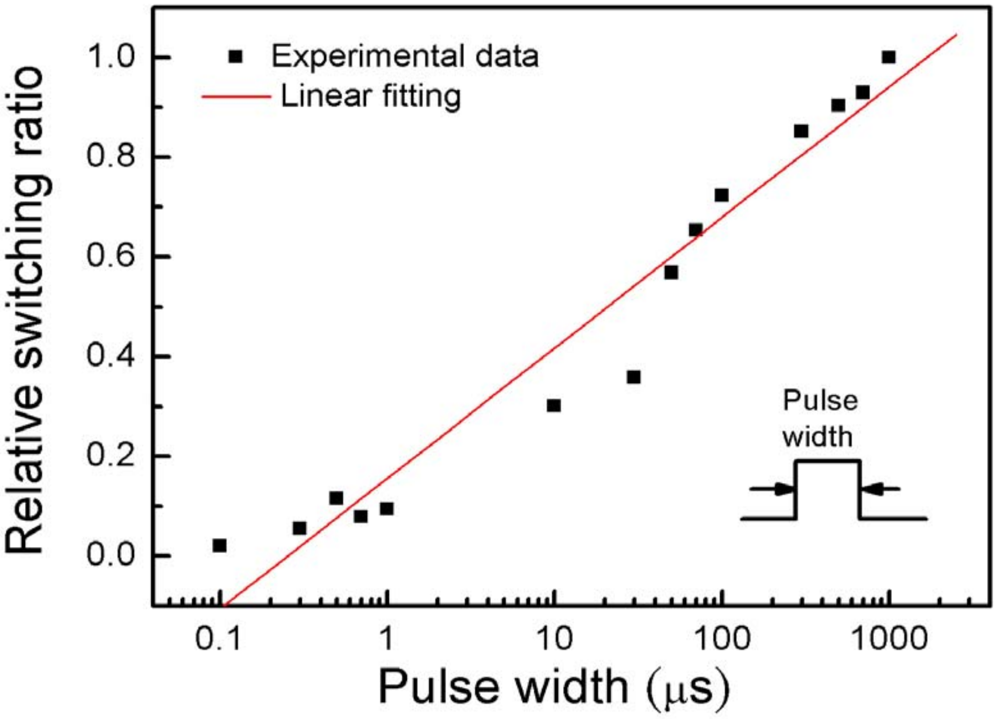

Figure 5-12 The dependence of switching ratios on pulse width: using the same pulse magnitude (-21 V).100% of switching ratio was defined as the switching effect with pulse width of 1 ms.

As we can see, the switching ratio decreases when the pulse width decreases with the same voltage magnitude. That means if a constant resistive switching ratio is to be achieved, a larger switching voltage should be applied. To do so, a constant switching ratio was set as the designated value, and the voltage pulse magnitude was increased progressively while keeping the pulse width fixed. After the magnitude of the required voltage was found out at that particular pulse width, the pulse width was decreased and the voltage magnitude was increased until the preset switching ratio was obtained again. The process was repeated until the pulse width was reduced to 10 μs. *Figure 5-13* shows the relationship between pulse width and voltage magnitude for obtaining a constant switching ratio. Again, a log-linear relationship is observed between the pulse width and the switching voltage.

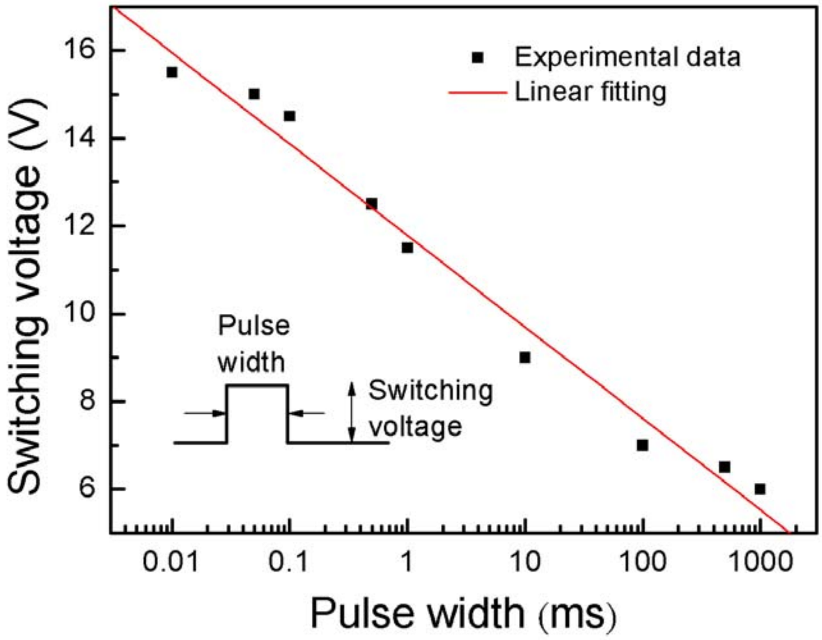

Figure 5-13 The relationship between switching voltage and pulse width for achieving a constant switching ratio of around 30%.

5.6.2 Retention

The ability of information retention is one of the most important criteria for non-volatile memory applications. Retention is defined as the duration in which information can be stored in the device after programming. Commercial memory products are commonly designed for storing information over 10 years (10^8 s). In my measurements, the resistances of switched devices were measured every 24 hours for a month. The device was placed in an atmospheric condition within a plastic box to avoid dust and accidental damaging. *Figure 5-14* shows the result of a PCMO resistive switching device with 100 µm square Al and Au electrodes. At the beginning, a resistance change by over one order of magnitude was obtained. However, in the next 5 days, the low resistance value kept increasing, and it stabilizes at 1 MΩ after several days. Over 1 month after the information was stored, two resistance states were still separated widely, with a resistance ratio of 4 between the two states. After one month, the sample was switch to HRS and measurements was repeated.

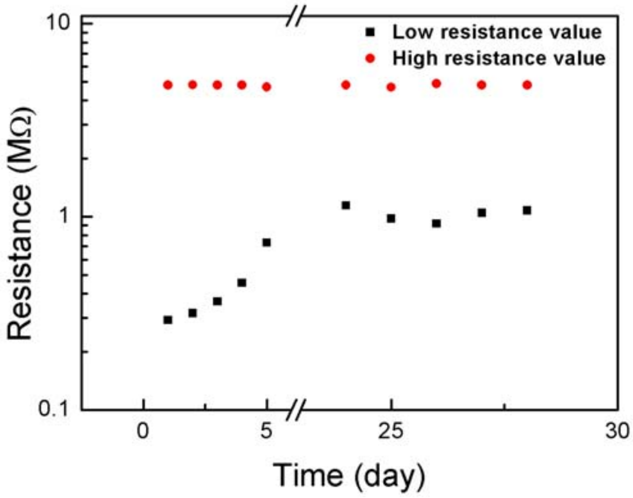

Figure 5-14 Retention of the PCMO resistive switching device at LRS (black) and HRS (red).

5.6.3 Endurance

Another important criteria for non-volatile memory applications is endurance. This represents the reproducibility of information upon repeated switching, i.e. how many set/reset cycles can be endured by the device before the LRS and the HRS are no longer distinguishable. In my experiments, switching was performed with similar setup as resistance switching measurement (*Figure 3-4(a)*). The device was continuously switching for 50,000 times with ±8 V pulses of 10 ms, and the results are shown in *Figure 5-15.* Over around 50,000 times switching cycles, the resistance values of both states were nearly the same. Fluctuations of the resistance values were obtained, but no overlapping of resistance states was observed. However, when the measurements were stopped, both resistance state values increased slowly back to a relatively high value (~22 kΩ HRS and 18 kΩ in LRS).

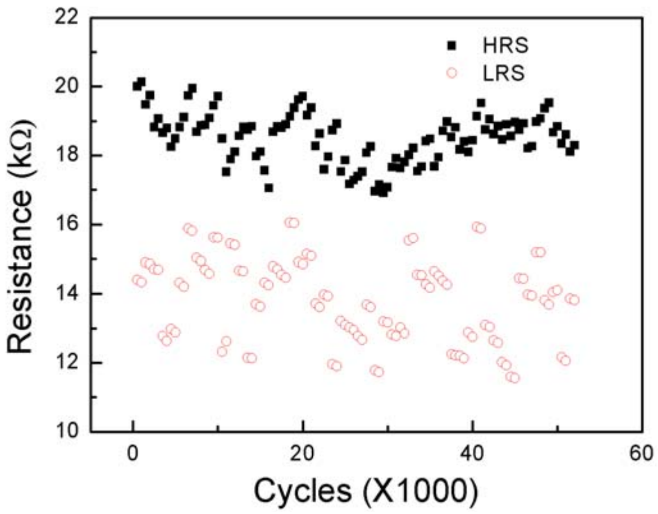

Figure 5-15 The endurance test of Al/PCMO/Ti switching device over 50,000 cycles.

Although the PCMO switching devices survived an endurance of 5×10^4 cycles, the resistance values of both states and the switching ratio are not stable enough for commercial products. For the further work, apart from the investigation of resistive switching mechanism, the improvement of the switching performances (including retention and endurance of the devices) is an important goal to achieve.

5.7 Summary

Planar PCMO resistive switching devices with different electrodes were introduced. The characteristics and performances of such switching devices, including *I-V* characteristics, pulse width and pulse magnitude dependence, retention and endurance, were discussed in this Chapter. Only PCMO devices with Al electrodes on one side showed good switching behaviours. The switching ratio of the devices depended on the separation between electrodes, pulse width and magnitude. The devices achieved 50000 cycles of endurance test. However, the switching devices were not stable enough for commercial application. Further investigations and improvements are needed for it to become a promising candidate of next-generation memory.

Chapter 6 Resistive switching properties of top-down epitaxial $Pr_{0.7}Ca_{0.3}MnO_3$ thin films

6.1 Introduction

Resistive switching effect in planar devices were discussed in Chapter 5 and resistive switching properties and performance were discussed. Planar resistance switching devices are easier to fabricate and to observe the switching effect, allowing a more straight-forward study on the parameters related to the switching effect. However, for memory applications, planar PCMO switching devices are far too large for compact memory devices. In order to apply resistive switching effect in commercial memory devices, a top-down geometry should be employed. In this Chapter, such devices are prepared by depositing conductive $LaNiO_3$ (LNO) on LAO (001) single crystal substrates, followed by the growth of PCMO thin films and Pt top electrodes.

6.2 Experimental details

Thick (200 nm) epitaxial films of LNO were grown by PLD with a LAO substrate temperature of 650 ℃ and an oxygen pressure of 150 mTorr . The laser pulse energy was around 250 mJ, with a repetition rate of 5 Hz. The 100 nm thick PCMO was then deposited with a mechanical stainless-steel shadow mask at 650 ℃ substrate temperature and 150 m Torr oxygen pressure with 200 mJ laser pulse energy. After deposition, films were cooled down to room temperature at a rate of 10 ℃ min^{-1} under the same oxygen pressure. Then, metal electrodes with diameter 100 μm were patterned and deposited on both LNO and PCMO thin films by using a shadow mask. Structural analysis was performed by XRD, and electrical measurements (*I-V* characteristics and resistance switching measurements) were performed with a

Keithley 2400 at room temperature. *Figure 6-1* shows the measurement setup.

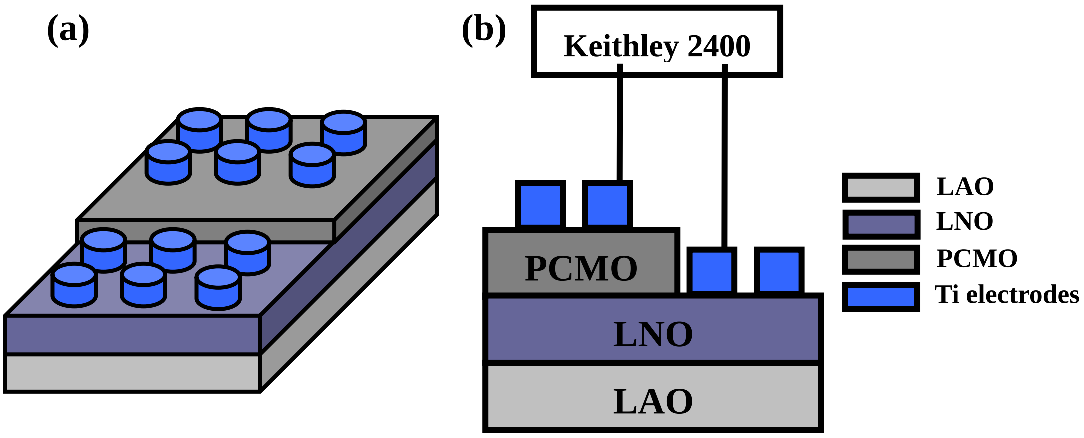

Figure 6-1 Schematic diagram (a) and setup (b) of Ti/PCMO/LNO/LAO top-down switching devices.

6.3 Structural analysis

Figure 6-1 shows the θ-2θ scan of a PCMO/LNO thin film grown on LAO substrate. The PCMO (002) and LNO (002) peaks are almost in the same position. A sharp peak shows that the PCMO film deposited on LNO has good crystallinity. The rocking curve of the PCMO at the (002) peak was also scanned, and *Figure 6-3* shows that the film is textured with a FWHM of 0.67°. Phi (ϕ) scans further confirm the epitaxial cube-on-cube growth of the film (*Figure 6-4*).

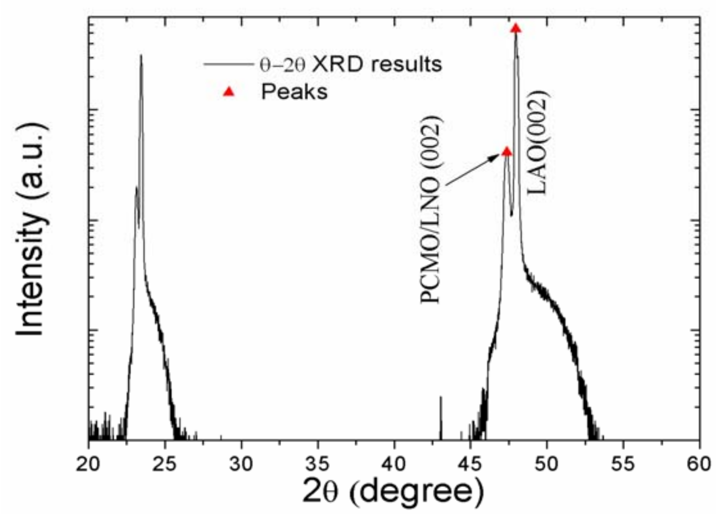

Figure 6-2 XRD θ-2θ scan of a PCMO/LNO film deposited on LAO (001) substrate.

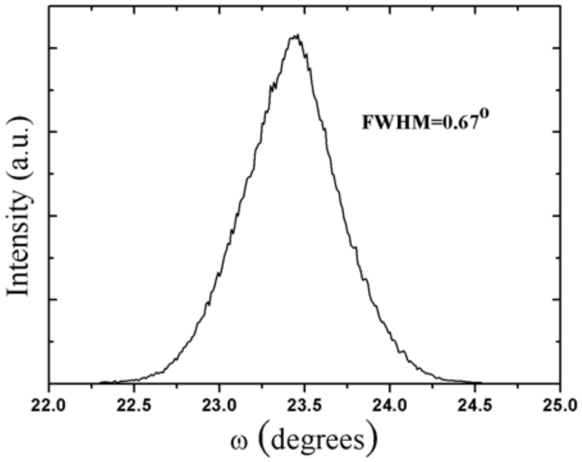

Figure 6-3 XRD rocking curve of the PCMO (002) peak.

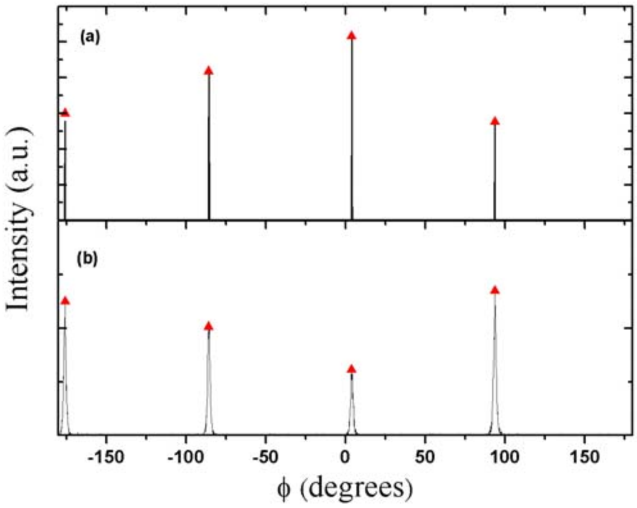

Figure 6-4 Phi scan of (a) LAO (202) and (b) PCMO/LNO (202) planes.

6.4 Electrical characterization

Figure 6-5 shows the *I-V* characteristics of the sample before and after forming. When the voltage is initially ramped from 0 to +8 V (Path 1), current passes from the top PCMO to bottom LNO layer, and the sample is kept in the highly conducting state (around 300 Ω). When the voltage is ramped to +8 V, the resistance of the sample increases suddenly to the order of a few kΩ (Path 2). This is the forming process Afterwards, the resistance of the sample is kept at the same order and does not return back to its initial state, no matter higher voltage is applied (Path 3-6).

After forming, a clear asymmetric and hysteretic behaviour with a sharp switching voltage observed in the negative voltage bias. In the first *I-V* cycle after forming process (*Figure 6-5*), the resistance suddenly changes to a lower value at -5 V; such a switching voltage, however, is reduced to -4 V and -3.5 V in the second and the third cycles, respectively (*Figure 6-5*). Afterwards the switching voltage is stabilized and remains fairly constant.

After forming and a few cycles of voltage sweeps, the *I-V* characteristic becomes stable, which is shown in *Figure 6-6*. As the voltage across a device increases from zero, the slope of the *I-V* plot is very small and represents a high resistance value of the sample. When the voltage is subsequently ramped down to zero, the current is kept at a low value similar to the ramp-up path. When the voltage drops below -4 V, the size of current across the sample sharply increases. The current value then retains at a large value when the voltage ramps back to zero, which is implying a lower resistance.

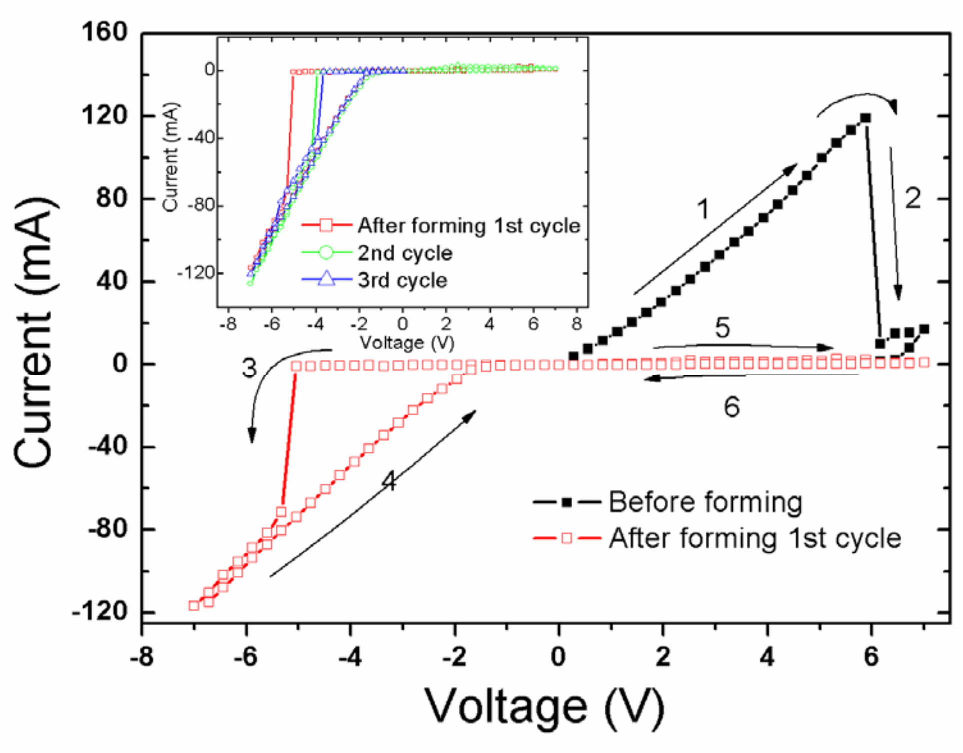

Figure 6-5 I-V characteristics of Ti/PCMO/LNO/LAO top-down sample before the forming process (black) and during the 1st I-V cycle after forming (red). Inset: 1st (red), 2nd (green) and 3rd (blue) I-V cycles after the forming process.

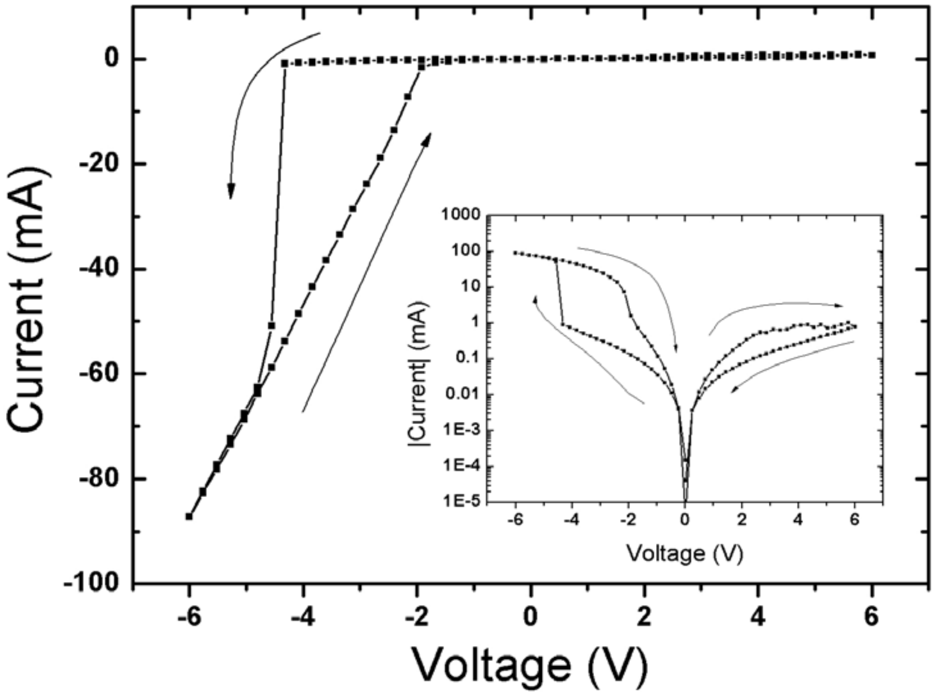

Figure 6-6 I-V characteristic of Ti/PCMO/LNO/LAO top-down resistive switching device. Inset: Semi-l-log scale plot of the I-V characteristic.

Resistance switching measurements were performed with the circuit shown in *Figure 6-1*. Changes in sample resistances, after the application of voltage pulses, are displayed in *Figure 6-7*. The measurement procedure is as follows. After applying a pulse at 4.5 V for 1 ms, the sample resistance was measured with a bias of -2 V. Subsequently, a -4.5 V pulse was applied to switch the sample to the LRS, and the resistance was measured again. To avoid damages to the samples, ±4.5 V was chosen as the switching voltages. Moreover, according to the *I-V* characteristics, -4.5 V is enough to switch the sample from the HRS to the LRS. On the other hand, the probing voltage was set at -2 V as this gave a larger switching ratio. Switching properties were stable over 40 switching cycles, and an averaged switching ratio of 230 % was obtained.

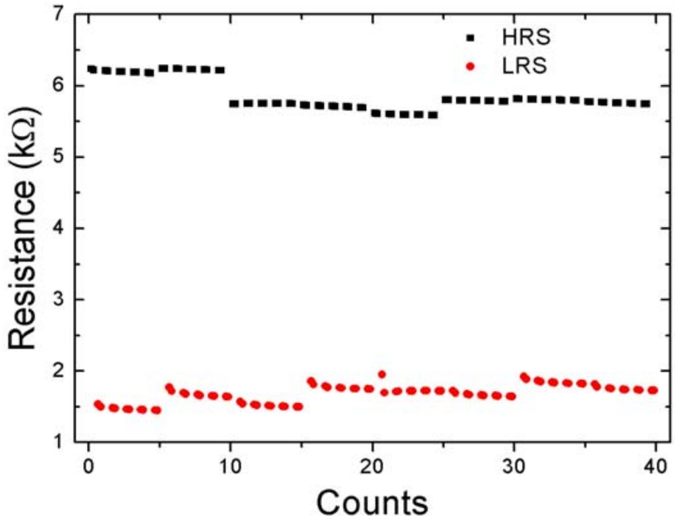

Figure 6-7 Resistance switching measurements of Ti/PCMO/LNO/LAO top-down device, where solid circles and squares correspond to LRS, and HRS.

A simple analysis of the top-down geometry device (*Figure 6.8(a)*) is made with 3 interfaces and 2 bulk resistances, and the corresponding circuit is shown in *Figure 6-8(b)*. $R_{Ti/PCMO}$, $R_{PCMO/LNO}$ and $R_{Ti/LNO}$ are the interface resistances between Ti/PCMO, PCMO/LNO and Ti/LNO, where R_{PCMO} and R_{LNO} are the bulk resistances of PCMO and LNO. As seen in Chapter 5, resistive switching occurs dominantly at the interfaces; in planar and top-down geometry devices there are two and three interfaces, respectively.

In order to locate the position in which switching occurs in this devices, several "electrode swapping measurements" were done. During such measurements, the *I-V* behaviour was measured by switching between several top (or bottom) electrodes, with the forming process only performed on a fixed pair of electrodes, *e.g.* Ti1/PCMO/LNO/Ti I. Subsequently, the *I-V* characteristics were measured by fixing the top Ti electrode (Ti1) while switching between two separate bottom Ti electrodes (Ti Ⅰ and Ti Ⅱ). The results are shown in *Figure 6-9*. For Ti1/PCMO with Ti Ⅰ /LNO pair, the junction shows hysteretic *I-V* behaviour after forming, similar with the previous case (*Figure 6-6*). After that, Ti1/PCMO was fixed and the bottom electrode was switched to Ti Ⅱ. Nearly identical *I-V* characteristic is observed. From this observation, it can be concluded that resistive switching is due to the upper part of the device.

I-V characteristics for swapping the top electrodes were also measured. Firstly, resistive switching was performed in the Ti1/PCMO/LNO/Ti Ⅰ device, which shows the same behaviour as in *Figure 6-9*. Then the *I-V* characteristic was measured with Ti1 replaced by Ti2, which was a top electrode with no measurements performed previously on it. If Ti Ⅰ /LNO junction contributes switching effect, Ti2/PCMO with Ti Ⅰ /LNO pairs should also show hysteretic behaviour. However, according to *Figure 6-10*, non-hysteretic *I-V* behaviour was obtained. The *I-V* characteristic was similar as that before forming was obtained. Owing to these results, I conclude that the Ti/LNO interface does not contribute to the resistive switching effect.

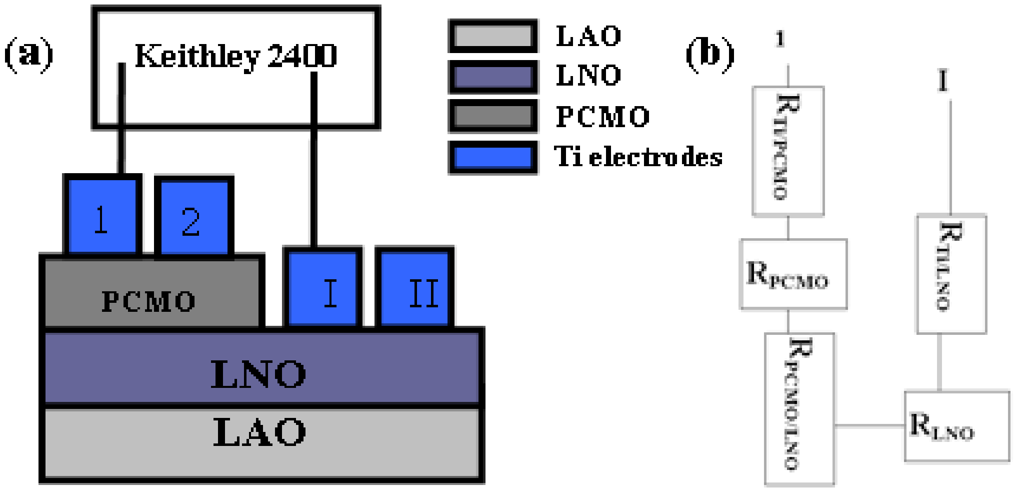

Figure 6-8 Schematic measurement setup of the PCMO top-down device (a) and its equivalent resistance circuit (b).

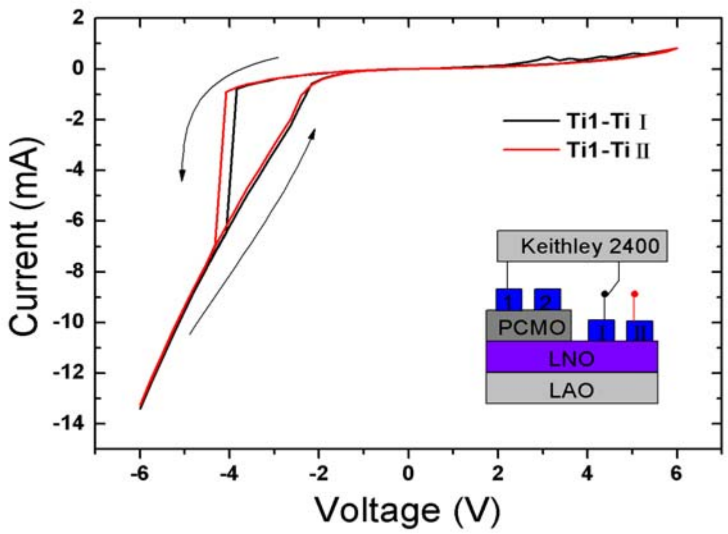

Figure 6-9 I-V characteristics of PCMO top-down resistive switching devices with different bottom electrodes, measured after the forming process was performed across Ti1/PCMO/LNO/Ti Ⅰ : Ti1/PCMO - Ti Ⅰ/LNO pair (black) and Ti1/PCMO - Ti Ⅱ/ LNO pair (red).The schematic of the measurement setup is shown in the inset, with a switch inserted between the bottom electrode connection.

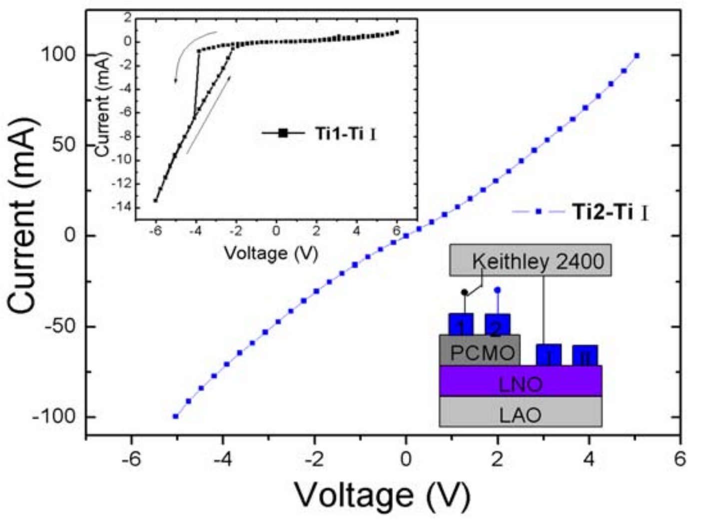

Figure 6-10I-V characteristics of PCMO top-down resistive switching devices with different top electrodes after the forming process at Ti1/PCMO with Ti Ⅰ/LNO pair: Ti1/PCMO with Ti Ⅰ/LNO pair (black) and Ti2/PCMO and Ti Ⅰ/LNO pair (blue). Inset: Schematic of measurement setup, which a switch inserted between the top electrode connection.

Forming processes are needed to activate the resistive switching phenomena. The forming voltage must be a positive bias, in which the current passes from Ti top electrode through PCMO and LNO layer and finally into the Ti bottom electrode. In contrast, firstly applying a large negative bias (-9 V)would also cause a sudden resistance drop similar to the forming process in positive bias, but no resistive switching effect can be observed and only a non-linear symmetric *I-V* characteristic can be obtained.

I-V measurements were also performed for swapped top and bottom electrodes for devices formed under -8 V bias conditions, and the results are shown in *Figure 6-11 and 6-12*. Similar current ranges and *I-V* behaviours can be observed, when the top electrode Ti1 is changed to Ti2 while the same bottom electrode is Ti used. However, when the bottom Ti Ⅰ electrode is replaced by a fresh Ti Ⅱ electrode, both resistance value and *I-V* characteristic is similar as a fresh sample. In conclusion, large negative voltage bias would damage the junction of Ti/LNO interface.

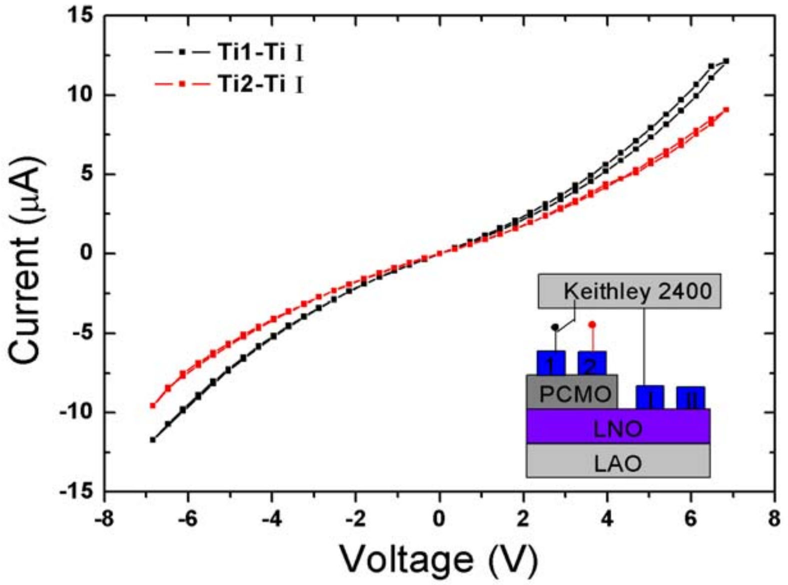

Figure 6-11I-V characteristics of PCMO sample with different top electrodes after-9 V voltage bias at Ti1/PCMO with TiⅠ/LNO pair: Ti1/PCMO with TiⅠ/LNO pair (black) and Ti2/PCMO and TiⅠ/LNO pair (red). Inset: Schematic measurement setup, which a switch was inserted between the top electrode connection.

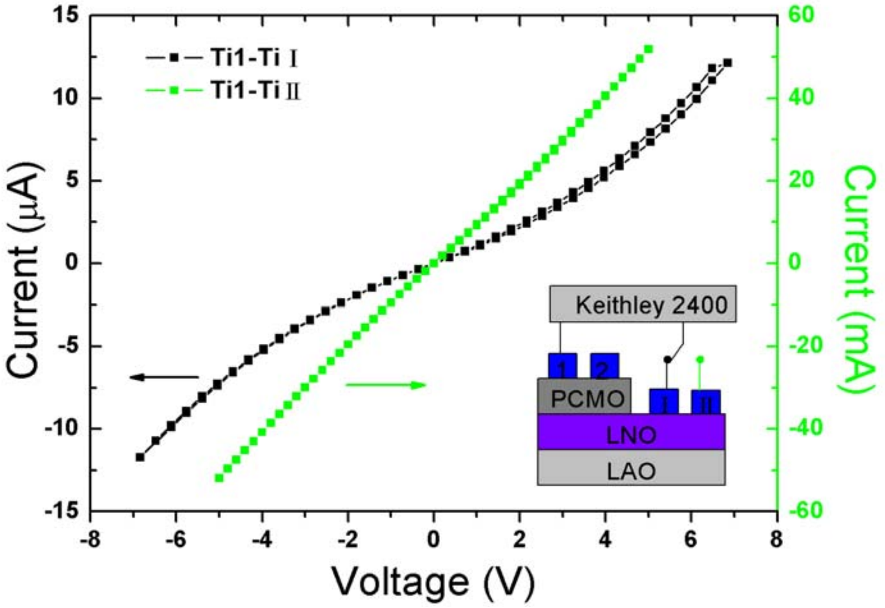

Figure 6-12I-V characteristics of a PCMO sample with different top electrodes after forming with a -9 V voltage bias at Ti1/PCMO/LNO/ TiⅠ: Ti1/PCMO-TiⅠ/LNO pair (black) and Ti1/PCMO-TiⅡ/LNO pair (green). Inset: Schematic measurement setup, with a switch inserted between the bottom electrode connection.

In order to clarify the exact location where the switching takes place, additional devices with the PCMO layer sandwiched between two LNO layers were prepared. Similar *I-V* characteristic measurements were performed. No hysteretic *I-V* behavior can be observed (*Figure 6-13*). If the PCMO/LNO interface does contribute to the switching effect, resistive switching behaviour should be observed after the forming process. However, the result indicates no hysteretic behaviour, which implies that no resistive switching can be achieved and the PCMO/LNO interface is not responsible for the switching in PCMO-based devices studied in this work.

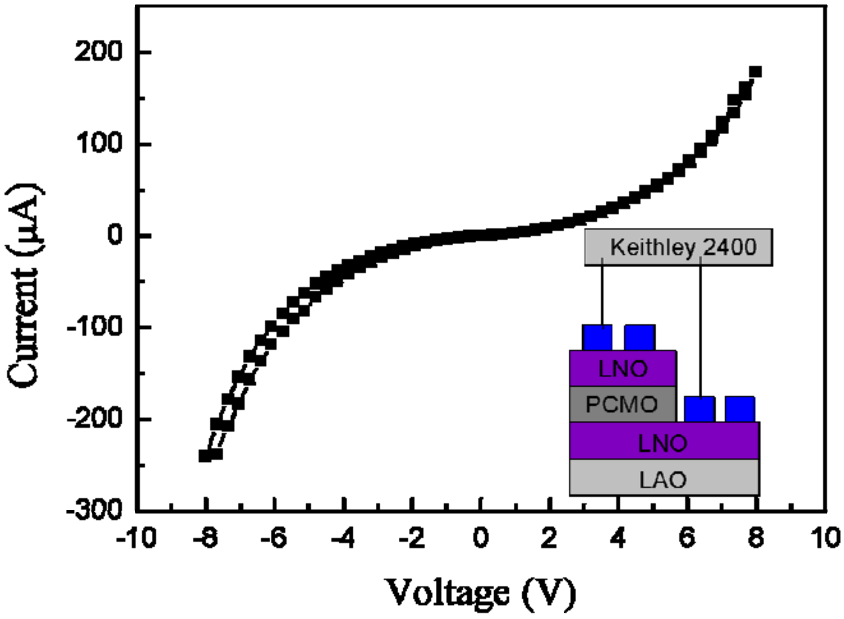

Figure 6-13 I-V characteristics of LNO/PCMO/LNO top-down device after forming with a -9 V voltage bias. .

The mechanism of resistive switching is still under debate. The experiments above have indicated that the Ti/PCMO interface is responsible for the switching effect. It has been suggested that the formation and disruption of TiO_x at Ti/PCMO interface is responsible for the switching effect[80]. When a high positive voltage bias is applied to the sample from the top Ti electrode, the electrode acts as an anode and attracts oxygen ions from the PCMO to form a TiO_x resistive layer. A sudden resistance increase constitutes the forming process, and a hysteretic *I-V* and resistive switching behaviour is obtained. In positive voltage bias, the top Ti electrode attracts negative-charged oxygen ions from the PCMO and further increases the thickness of the TiO_x resistive layer. In the negative voltage bias, the voltage can dissociate TiO_x into Ti and O^{2-}, so the sample resistance is decreased and is driven into the low resistive state.

6.5 Conclusion

PCMO-based top-down geometry resistive switching devices with Ti electrodes were demonstrated in this Chapter. Ti/PCMO/LNO/LAO resistive switching devices were obtained after the forming process, in which a large current passed from top electrode to bottom electrode. Over 200% of resistive switching ratio was obtained in ±5 V. Several experiments were performed, which showed that the bottom Ti electrode was not responsible for the switching effect, and the Ti/LNO interface was not responsible for the switching process.

Chapter 7 Study of EPIR switching mechanism with thermocouple based on planar PCMO resistive switching devices

In this Chapter, planar PCMO resistive switching devices with Al and Ni electrodes are investigated. In particular, thermal measurements on these devices with micro-thermocouples are discussed, which sheds light on for the resistive switching mechanism.

7.1 Introduction

As mentioned in Chapter 2, although resistive switching devices have been successfully demonstrated by different research groups, the actual operating mechanism behind the effect is still under debate[24, 39]. In order to determine the mechanism of resistive switching effect, lots of experiments and analysis were performed, including electrical and structural characterization. For example, impedance spectroscopy was used to analyze the changes of resistance circuit in the devices before and after switching[122]. Scanning Kelvin probe microscopy was involved to measure the surface potential changes of the switching devices[90]. X-ray photoelectron spectroscopy was performed for analyzing the elemental composition and their electronic states in the devices[83]. Recently, high-resolution transmission electron microscopy was also used to study the interfaces between metal electrodes and oxide thin films, and the existence of an interfacial metal oxide layer was observed[81].

While most of the studies are focused on the electrical aspects of resistive switching devices[90, 122], there are only a few groups which studied the switching effect by thermal methods. Sato *et al.*[123] found that the pulse duration needed to switch the sample back to HRS with constant voltage depends on the resistance in the LRS in NiO switching devices, and they used thermal simulation to calculate the thermal distribution of the device. Cheng *et al.*[124] studied the switching effect in capacitor-like NiO switching devices, and they numerically simulated the thermal distribution inside the devices. They showed that bottom electrode thickness played an important role in the resistive switching behaviour, and suggested it is related to the thermal stability of conducting filaments. Experimental evidence was proposed by Azumi *et al.*[125], who used microspectroscopic imaging for observing the optical reflectivity of $La_{0.33}Sr_{0.67}FeO_3$-based planar geometry switching devices. This technique was similar to my later experiment of the thermo-reflectance imaging. They noticed that the profile of conducting area between two electrodes changed during switching, and it was explained by the Joule heating which caused oxygen-ion migration. Janousch *et al.*[59] also performed similar experiment in Cr-doped $SrTiO_3$ single crystal with infrared thermal image, in which hot spots were observed in the anode at HRS.

However, it has been shown that the interface resistance between the electrodes and PCMO is much larger than the intrinsic resistance of PCMO thin films, and it is believed that the transport properties are dominated by the interfaces[68]. Besides, devices with PCMO films and metal electrodes of similar work functions have shown drastically different I-V characteristics and resistance switching phenomena, as shown in Chapter 4. These suggested that carrier transport at interfaces cannot be simply explained by Schottky barrier effect[68, 73, 81]. Indeed, Li *et al.*[81] have observed an AlO_x layer at the Al/PCMO interface by transmission electron microscopy, and they have attributed the RS effect to the formation and dissociation of the alumina layer. However, due to the experimental difficulties on direct profiling the electrical properties of the interface between the metal electrodes and the PCMO films, it remains challenging to investigate the influence of the interface effect on resistance switching.

It is therefore worthwhile to investigate resistive switching by thermal means, in order to obtain further information for investigating the resistance switching mechanism. In this project, I monitored the temperature variations of the metal electrodes in PCMO-based planar resistive switching devices. Micro-thermocouples were used for direct probing of the temperature of the electrodes. Such a measurement provides a direct, non-destructive and simple characterization method to obtain the thermal information from the devices. In the experiment, the temperature of electrodes at both HRS and LRS at the same current bias levels were measured. Temperature variations at HRS and LRS were compared directly, and according to the measurements, the origin of the heat sources was studied.

7.2 Experimental details

The structure tested was Al/PCMO/Ni in a planar geometry. 250-nm-thick PCMO perovskite thin films were epitaxially grown on LAO (001) substrates by PLD, using the same deposition conditions as described in Chapter 5. Metal electrodes with 800-μm diameters were prepared on PCMO through photolithography-prepared lift-off patterns, and the minimum separation between pairs of electrodes was 30 μm (*Figure 7-1)*. Electrical measurements, including *I-V* characteristics and resistance switching measurements, were performed with a Keithley 2400 sourcemeter.

For temperature measurements, two 30-μm-diameter type-T microthermocouples were placed on the Al and Ni electrodes directly, and the temperature data were real-time monitored and recorded by a LABVIEW program at a rate of 5 Hz. All measurements were performed at room temperature. The schematic diagrams of electrical and thermal measurement setups are shown in *Figure 7-1*.

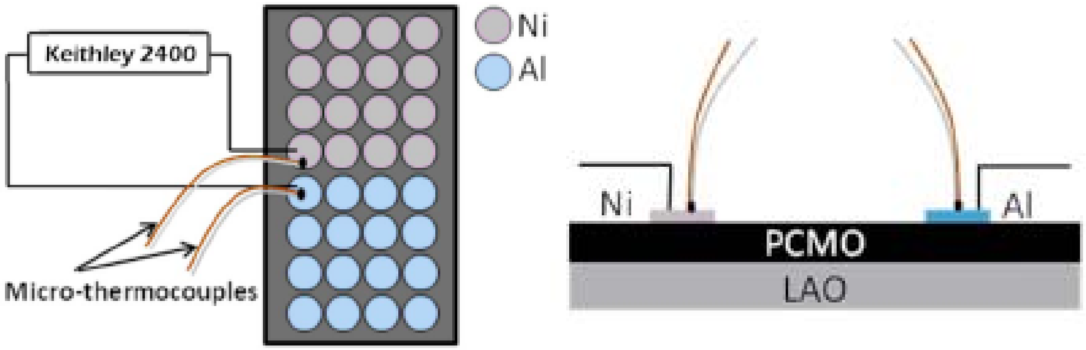

Figure 7-1 Schematic diagrams of electrical (left) and thermal measurement setups (right).

7.3 Electrical measurements

The *I-V* characteristic of an Al/PCMO/Ni device, as measured by the two-point probe method, is shown in *Figure 7-2*. Here the positive bias is defined as electric current flowing from Al to Ni. When the applied voltage bias increases from 0 to +10 V (path 1), the slope of the *I-V* curve is gentle and the device is at HRS. It remains at HRS along path 2 and path 3, until the applied voltage is over -6.4 V at path 3. The current across the sample increases suddenly from this point, and the device is switched into the LRS. After that, the device remains at LRS as the voltage returns to zero along path 4 and switchs again to HRS.

Resistance switching measurements were performed. The changes in sample resistances, after the application of voltage pulses, are displayed in *Figure 7-3*. After applying two pulses at -10 V for 1 ms, the sample resistance was measured with a bias of -2 V. Subsequently, two +10 V pulses were applied to switch the sample back to the HRS, and the resistance was measured again. A resistance switching ratio of around 200% was obtained over 100 switching cycles. The LRS and HRS resistance values are fairly stable through this period except in the last part of the measurement, in which a slight increase of resistance on both states were obtained.

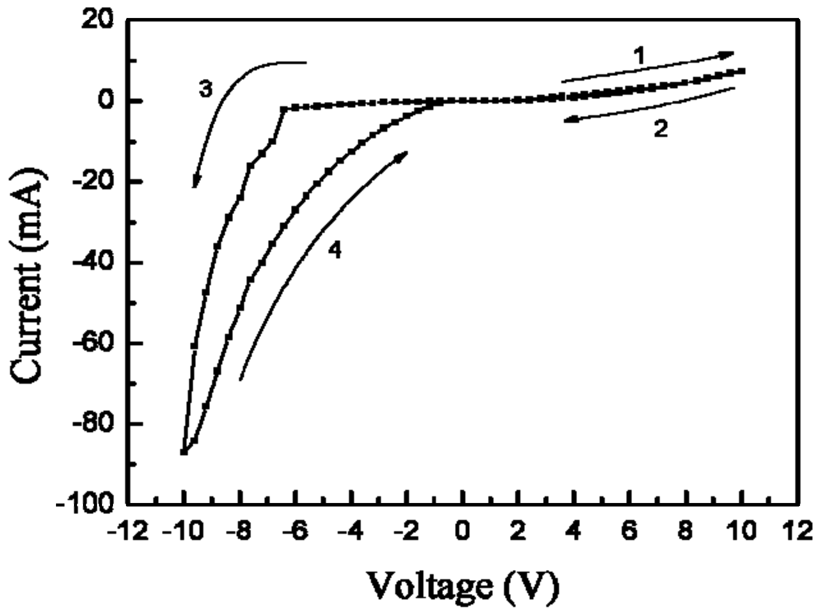

Figure 7-2 I-V characteristic of a Al/PCMO/Ni device obtained by two-point probe measurement.

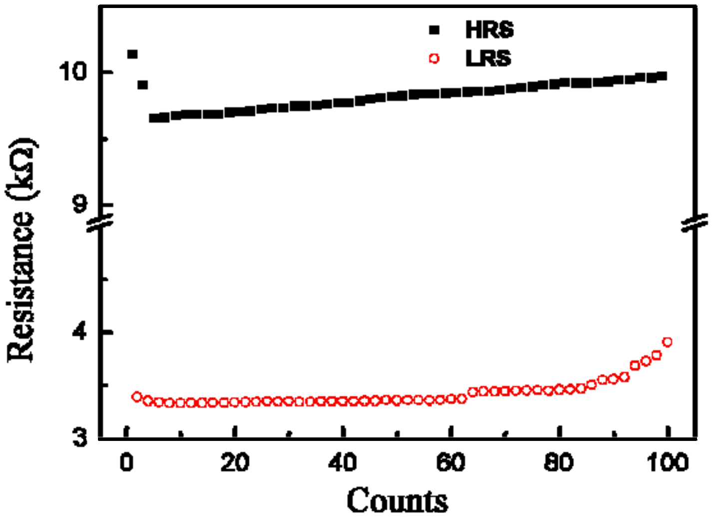

Figure 7-3 Resistance switching measurement of the Al/PCMO/Ni device.

7.4 Thermal measurements

For thermal measurements, background measurement (i.e. temperature measurement without bias voltage applied) was performed for 20 s, followed by a -2 V dc probing voltage (V_p) applied across the sample for 30 s. These procedures stabilized the temperature changes caused by the voltage bias applied and ensured identical starting conditions for the sample during measurements. The thermal response of the device as a function of time is plotted in *Figure 7-4*. It can be seen that no observable temperature difference between the two electrodes was detected. Initially, the sample was set in HRS. Subsequently, a negative dc current (I_{bias}) was applied for another 30 s, switching the sample to LRS. A large temperature difference between Al and Ni was measured during the application of I_{bias}, which suggests uneven heating inside the device. Afterwards, V_p was applied to the device for 60 s, and the electrode temperatures decreased gradually back to the initial values. Similarly, for HRS measurements I_{bias} of the same positive magnitudes were applied to the device, and the thermal responses at LRS and HRS were compared directly.

It is worth to mention that the thermocouples used for measuring Al and Ni electrode temperatures have been swapped during the experiment, to ensure the measured temperature difference was not due to the intrinsic error from the thermocouples. Moreover, the position of the thermocouple was also a concern. It is possible that uneven heating on the electrodes surface may occur. Both thermocouples were places in the middle of the metal electrodes, where electrical probes were placed next to them and relatively far away from the junction. This ensured the current to pass through the metal electrodes at the position where thermocouples were placed, and so more observerable results can be achieved.

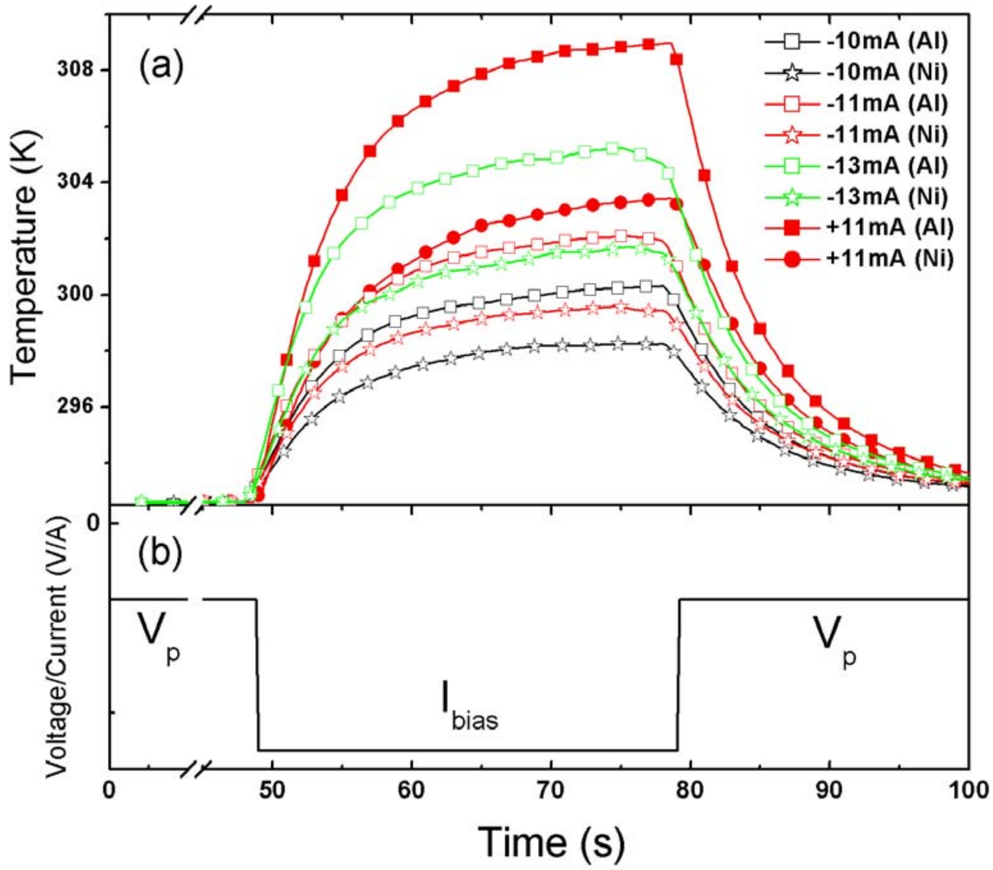

Figure 7-4 *(a) Thermal response of a Al/PCMO/Ni device subjected to external electrical signals, as a function of time. (b) The bias current/voltage profile during electrical measurements.*

The temperature response of Al and Ni electrodes at LRS and HRS as a function of I_{bias} magnitude is plotted in *Figure 7-5*. I_{bias} magnitude from 10 mA to 13 mA were chosen as resistance switching from HRS to LRS occurred at around -10 mA. It can be clearly observed that, for the same magnitude of I_{bias}, both electrodes have higher temperatures at the HRS than the LRS. In order to verify the origin of the heat source, the temperature differences between the HRS and LRS within the electrodes are plotted in *Figure 7-6*. It can be observed that when $|I_{\mathrm{bias}}|$ equals 13 mA, the Al electrode is at 315 and 305 K for HRS and LRS, respectively (i.e., $\Delta T_{Al} = 10$ K), whereas ΔT_{Ni} is just 6 K. The result suggests that a stronger local heat source exists under the Al electrode.

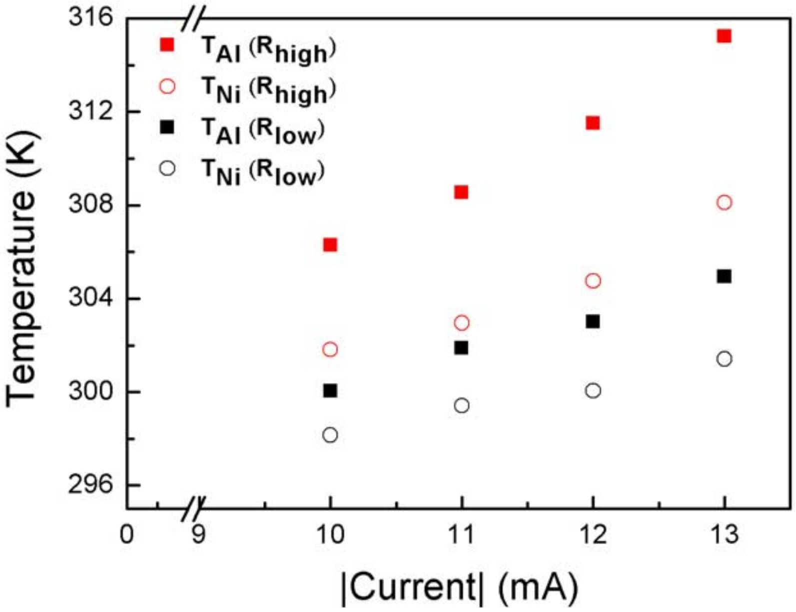

Figure 7-5 The thermal response of Al and Ni electrodes under HRS and LRS as a function of varying I_{bias}.

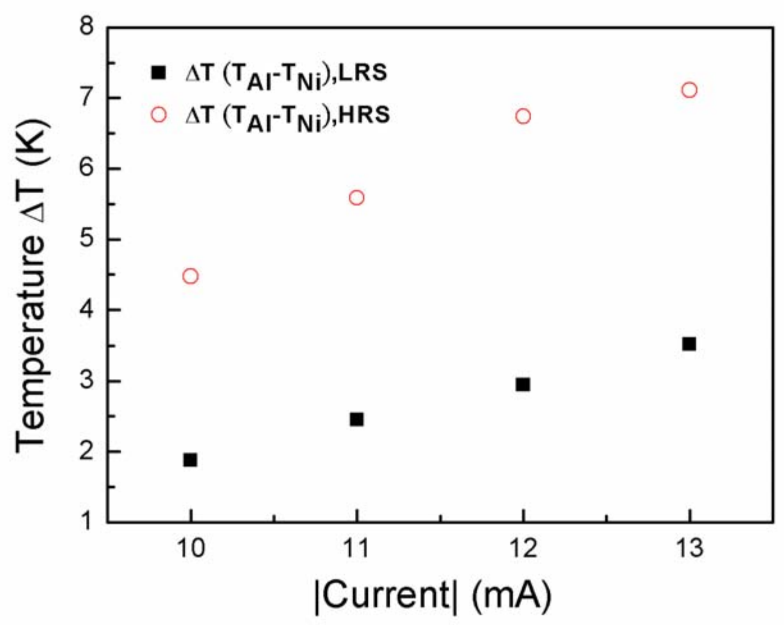

Figure 7-6 The temperature differences within the electrodes between HRS and LRS.

7.5 Discussion

According to the results, a higher temperature was observed in Al electrode, no matter the device was in LRS or HRS. A local heat source must exist under the Al electrode. This phenomenon can be explained by the finding that AlO_x layer exists at the interface between Al and PCMO thin films[81]. Locally, with a resistive AlO_x layer, more heat is generated during the application of the bias current. Thus, it causes additional heating, and a higher temperature was obtained.

Moreover, the characterization of the thermal response as a function of varying I_{bias} can provide extra information on the heating phenomenon[113]. There are two main types of heating effect, one is Joule effect and the other is Peltier effect. Joule effect is a quadratic effect, in which heat is dissipated by the resistor when a current is applied on it, and it is a bulk heating effect. Peltier effect is a linear effect with the bias current, in which the heat can be absorbed or liberated depending on the polarity of the current applied on two materials. These two effects can be distinguished by the temperature variation with different current bias. A quadratic behaviour between temperature and current bias represents Joule effect where linear relationship represents Peltier effect[113]. According to *Figure 7-6*, it seems the results cannot be simply explained by Joule heating effect due to a relatively linear relationship.

Apart from the thermal measurements, in order to verify the activating switching area of the devices, three-point and four-point resistance measurements were performed to determine the interfacial nature of resistive switching and the results are shown in *Table 7-1*. From the results, only the interface resistance of Al/PCMO was changed in the switching and the resistance difference were nearly the same as the totally resistance difference in the devices. It is concluded that Al/PCMO interface contribute the resistive switching.

	LRS	HRS
PCMO bulk resistance (4-point measurement)	0.5 kΩ	0.5 kΩ
Al/PCMO interface resistance (3–point measurement)	5.2 kΩ	7.8 kΩ
Ti/PCMO interface resistance (3–point measurement)	0.0278 kΩ	0.0278 kΩ
Total resistance (calculated base on 3-point and 4-point measurements)	5.73 kΩ	8.5 kΩ
Total resistance (base on resistance measurement)	5.5 kΩ	8.5 kΩ

Table 7-1 Summary of measured resistances at various locations of the Al/PCMO/Ni device, in LRS and HRS.

7.6 Conclusion

To summarize, thermal analysis was used as a direct and non-destructive method to study the resistance switching effect in planar Al/PCMO/Ni devices. Thermal measurements with thermocouples showed a significant temperature difference between the two electrodes, and higher temperature values were obtained at aluminum electrode at both HRS and LRS. It indicates the existence of a resistive layer underneath the Al electrode. This resistive layer is possibly AlO_x, which was also found in other studies in literature. Moreover, by three-point measurements, the switching performance is suggested to be due to the Al/PCMO interface resistance, and it further proves the interface between Al/PCMO contribute the switching effect. The thermal measurement can be very useful to characterize the resistive switching devices, and it can provide useful information on how input power is dissipated inside the devices.

Chapter 8 Study of resistive switching in planar PCMO resistive switching devices with thermoreflectance imaging

In this Chapter, planar PCMO resistive switching devices are studied. In particular, thermal measurements with thermoreflectance imaging technique are discussed. SEM with FIB technique are used to investigate the interface between metal and PCMO. These studies provide further support that oxide formation is responsible for the switching mechanism.

8.1 Introduction

In the last Chapter, I used a direct, *in-suit* thermal measurement with thermocouples on planar Al/PCMO/Ni devices to investigate the resistive switching phenomenon. It showed unequal heating at Al and Ni electrodes, with much stronger temperature changes observed at the Al electrodes between low and high resistance states. These information provide the temperature variation of surface of metal electrodes, and it is a suitable method to analyze the thermal response of the devices.

Thermal measurement with thermocouples is the easiest thermal characterization technique to measure the thermal properties of the devices. It is cheap and accurate. However, this technique only provides limited spatial thermal information, which is limited by the size of the thermocouple used. Given that the smallest size of commercially available thermocouple is 25-50 μm in diameter, it is impossible to perform experiments with greater details by using this technique[126]. Also, extreme care must be taken to handle the micro-thermocouples and setup the micro-probing system. In my case, thermocouples can be used to measure the temperature profile of the surface metal electrodes. However, as the separation between two electrodes was 30 μm, it reached the spatial resolution limit of my 30 μm thermocouples. Although uneven heating between electrodes was formed, it is worth to know the temperature distribution of the PCMO in between the metal electrodes. For example, a sharp filamentation path was observed in Cr-doped $SrTiO_3$ single crystal memory cell with an infrared thermal imaging technique[59]. Azumi *et al.*[125] also observed heat diffusion movement in the $La_{0.33}Sr_{0.67}FeO_{3-\delta}$ oxide surface during switching, and they proposed an oxygen-ion migration model to explain the phenomena and the switching effect. Studying the thermal profile of my PCMO surface is therefore important to determine the resistive switching mechanism. Thermal measurement techniques other than thermocouples were needed to achieve better spatial resolution.

There are a few different types of thermal measurements which can be used [126]. Infrared thermography is the most popular method among the thermal imaging techniques, in which sensitive infrared camera is used to measure the radiation intensity and determine the temperature of the object based on Plank's blackbody law. However, the highest spatial resolution of the image is 3 μm[126]. Scanning thermal microscopy can achieve spatial resolution image down to 0.05 μm. It is based on the scanning probe microscopy technique, with a very small thermocouple fabricated on the tip. This technique provides an excellent spatial resolution. However, a fairly long time is need to get a single thermal image[126].

To balance both spatial resolution and imaging time, the thermo-reflectance imaging technique was used in my experiment. It is based on the temperature-reflectivity relationship of the material. The reflectance signals of the materials are recorded by a CCD camera for temperature mapping. This technique provides a high spatial resolution down to 0.3-0.5 μm, and it does not need scanning and so it can save measurement time. Other poplar thermal measurement techniques are summarized in *Table 8-1*.

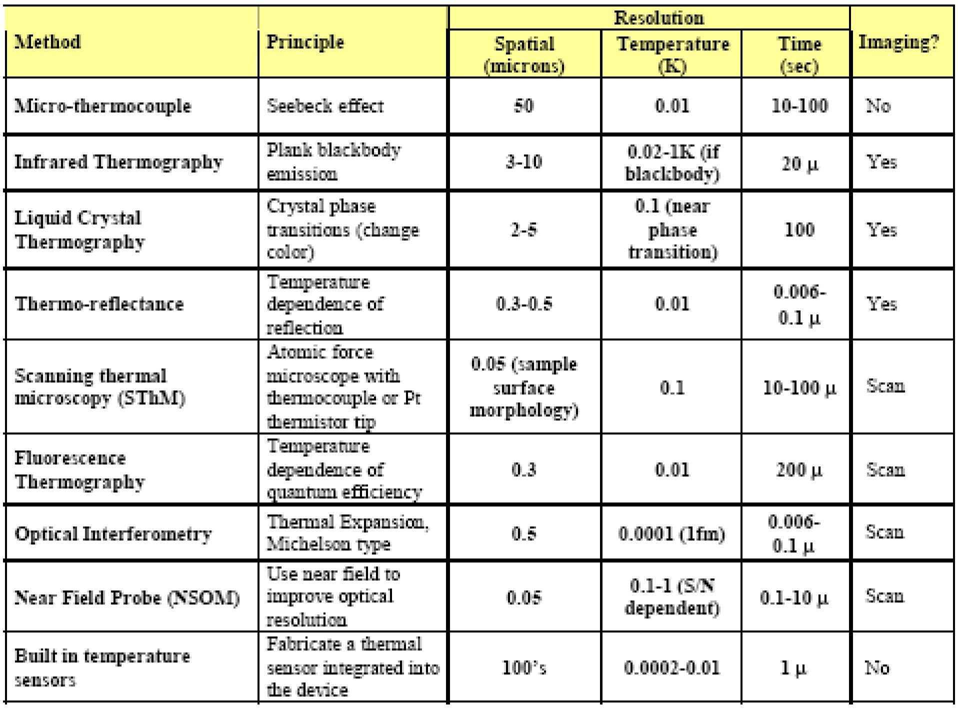

Method	Principle	Resolution			Imaging?
		Spatial (microns)	Temperature (K)	Time (sec)	
Micro-thermocouple	Seebeck effect	50	0.01	10-100	No
Infrared Thermography	Plank blackbody emission	3-10	0.02-1K (if blackbody)	20 μ	Yes
Liquid Crystal Thermography	Crystal phase transitions (change color)	2-5	0.1 (near phase transition)	100	Yes
Thermo-reflectance	Temperature dependence of reflection	0.3-0.5	0.01	0.006-0.1 μ	Yes
Scanning thermal microscopy (SThM)	Atomic force microscope with thermocouple or Pt thermistor tip	0.05 (sample surface morphology)	0.1	10-100 μ	Scan
Fluorescence Thermography	Temperature dependence of quantum efficiency	0.3	0.01	200 μ	Scan
Optical Interferometry	Thermal Expansion, Michelson type	0.5	0.0001 (1fm)	0.006-0.1 μ	Scan
Near Field Probe (NSOM)	Use near field to improve optical resolution	0.05	0.1-1 (S/N dependent)	0.1-10 μ	Scan
Built in temperature sensors	Fabricate a thermal sensor integrated into the device	100's	0.0002-0.01	1 μ	No

Table 8-1 Summary of popular thermal measurement techniques in micro- and nano-scales[126].

Thermoreflectance imaging technique has been successfully applied on studying various electronic devices including quantum dots (QD), quantum well (QW) lasers, and nanowire devices[127-129]. Recently, there is only one paper try to analyze the resistive switching devices with the thermoreflectance imaging technique[125], and it has the potential to extract some interesting information which is otherwise not assessable by other techniques.

The working principle of thermoreflectance imaging technique and equipment used were discussed in Chapter 3. In my current work, by using thermoreflectance method, thermal response information of the metal electrodes and the PCMO channel were obtained. Two-dimensional temperature maps can then be produced, allowing one to locate the origin of the heat sources and compare with the heat transfer model for characterizing the switching phenomenon under different bias conditions.

8.2 Experimental details

The structure under test is Al/PCMO/Ti with a planar geometry. 250-nm-thick PCMO perovskite thin films were epitaxially grown on LAO (001) substrates using PLD. Identical deposition conditions as PCMO thin films growth described in Chapter 5 were used. Metal electrodes (in form of 200 μm square) were prepared on PCMO through photolithography-prepared lift-off patterns, and the minimum separation between pairs of electrodes was around 40 μm (*Figure 8-1)*. Electrical measurements, including *I-V* characteristics and resistance switching measurements, were performed with a Keithley 2400 source meter.

For thermoreflectance imaging measurements, a 10-Hz voltage bias signal was sent to the device, and the frame trigger signal was sent to a 12-bits CCD camera. The frame trigger signal was phase-locked to the device bias signal at 40 Hz. A blue LED with wavelength of 470nm was used for illumination; operating the LED at constant input power ensured that the optical flux was a constant. Four pictures were taken by the CCD camera during each cycle of device bias, and the calculation of thermoreflectance signal ($\Delta R/R$) was based on the approach suggested by Grauby *et al.*[113] and Fournier *et al.*[112] by using a LabVIEW program. The schematic diagram of experimental setup for thermoreflectance imaging, electrical measurement setup and optical micrograph of a Al/PCMO/Ti resistive switching device are shown in *Figure 8-1*.

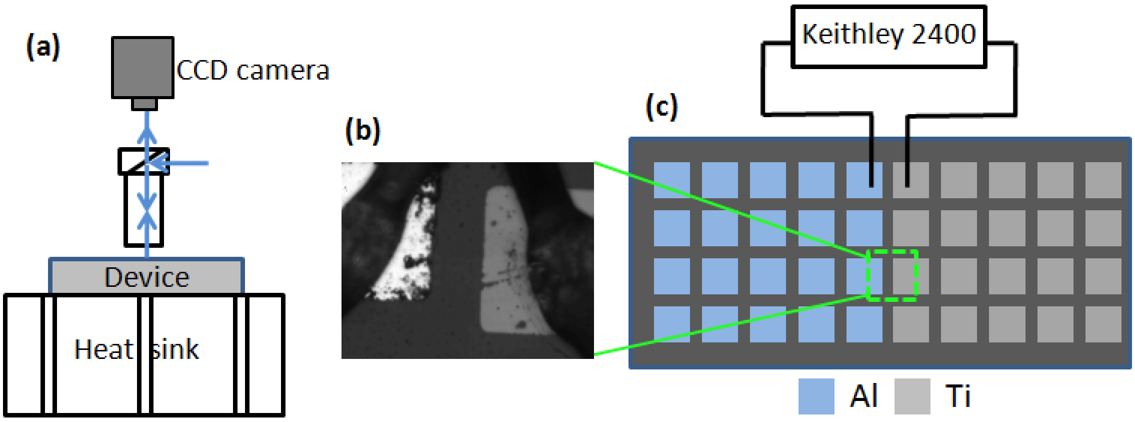

Figure 8-1 *(a) Schematic of experimental setup for thermoreflectance imaging. (b) Optical micrograph of a Al/PCMO/Ti resistive switching device. (c) Schematic of electrical setup.*

8.3 Electrical measurements

Figure 8-2 shows the *I-V* characteristics of a Al/PCMO/Ti device. A positive bias is defined as electric current flowing from Al to Ti. When the applied voltage bias is increased from zero to +5 V (path 1), the slope of the *I-V* curve is gentle and the device is at the HRS. It remains at HRS along paths 2 and 3, and switches to the LRS only when a -3.8 V bias is applied across the electrodes, which is accompanied by a sharp increase in current. The device then remains at the LRS along path 4, until a large positive bias is applied to the sample. By comparing the current values under HRS and LRS in *Figure 8-2*, the RS ratio is equal to 27 times for the device under a -2 V probing voltage. The maximum power consumption in this case is around 1 mW ($I(200uA)\times V(5V)$) which is quite small for memory applications.

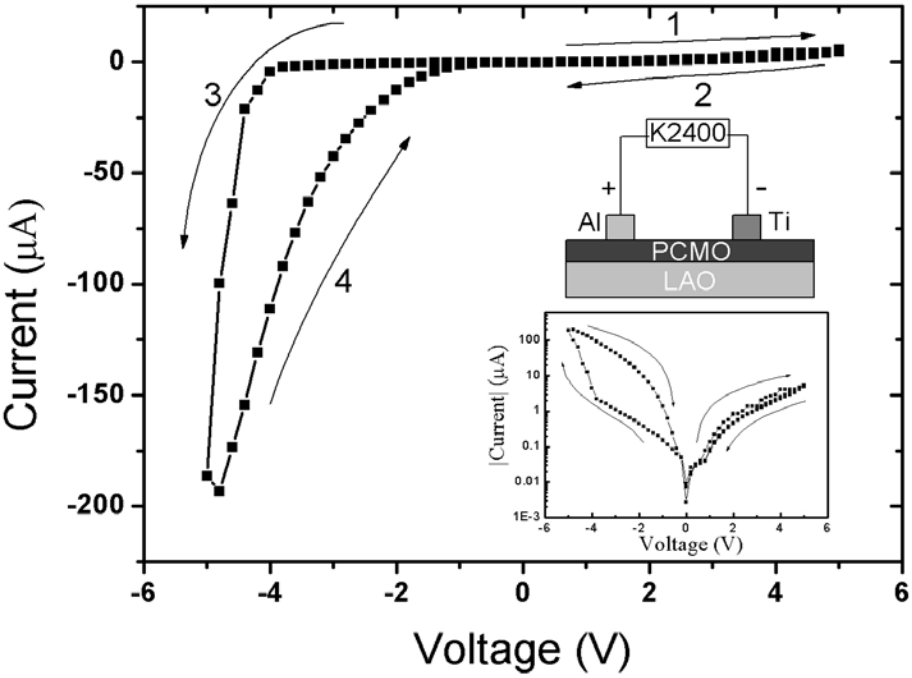

Figure 8-2 I-V characteristics of a typical Al/PCMO/Ni device. Upper inset indicates the polarity of the electrodes under positive bias, and lower inset shows the semi-log plot of the I-V curve.

8.4 Thermal measurements

Thermoreflectance images of a Al/PCMO/Ti device under different bias conditions are shown in *Figure 8-3(b) to (i)*. The images can be converted into temperature maps once the thermoreflectance signals ($\Delta R/R$) for different materials are multiplied by the corresponding thermoreflectance coefficients κ. The thermoreflectance coefficients of Al, Ti and PCMO are measured to be around 3×10^{-4}, 8×10^{-4} and 1.3×10^{-3} K^{-1} respectively by comparing the measured temperatures obtained using micro-thermocouple and the thermoreflectance signal under the same voltage bias. For simplicity, one can use the value of $\Delta R/R$ while comparing over the temperature changes of the same materials.

At positive bias (current flows from Al to Ti) (*Figure 8-3(b)-(d)*), the normalized thermoreflectance signal ($\Delta R/R$) (which is proportional to the temperature variation) within the device is spatially homogenous (3.2-3.5×10^{-4}), indicating a fairly uniform temperature distribution across the device and no localized heating can be observed. At low negative bias levels up to -3 V (*Figure 8-3(g)*), the thermoreflectance signal remains nearly the same as in the positive bias regime and no heating is observed. However, when the applied voltage is increased to -4 V (*Figure 8-3(h)*), localized hot spots starts forming at the PCMO edge next to the Al electrode and resistive switching from HRS to LRS occurs. If the bias voltage is further increased to -5 V (*Figure 8-3(i)*), stronger localized heating occur and the hot spots grow in size. The heated region spans over a distance of 10 μm along the edge of the Al electrode. This result agrees well with the previous finding in Chapter 7, where the interface between Al and PCMO is the major heat source of such RS devices. However, since the micro-thermocouples used in Chapter 7 had a diameter of 30 μm, it would be extremely difficult to measure the temperature of the PCMO channel in between the electrodes directly. Besides, the spatial resolution of the single-point measurement is insufficient for locating the hot spots on the PCMO channel.

To further investigate the localized heating effect on the device, the thermoreflectance signal (averaged across the hot spot region of the PCMO channel at various voltage biases) are compared in *Figure 8-4*. It can be observed that the heat source width is about 5 μm next to Al electrode on the PCMO channel. The thermal gradient of about 2×10^5 K/m represents a significant amount of heat flowing from the Al to Ti thought the PCMO. Such a localized heating phenomenon occurs only under large negative bias, during which switching from HRS to LRS occurs. The temperature increase for the hot spot under LRS is 7 times larger than the HRS.

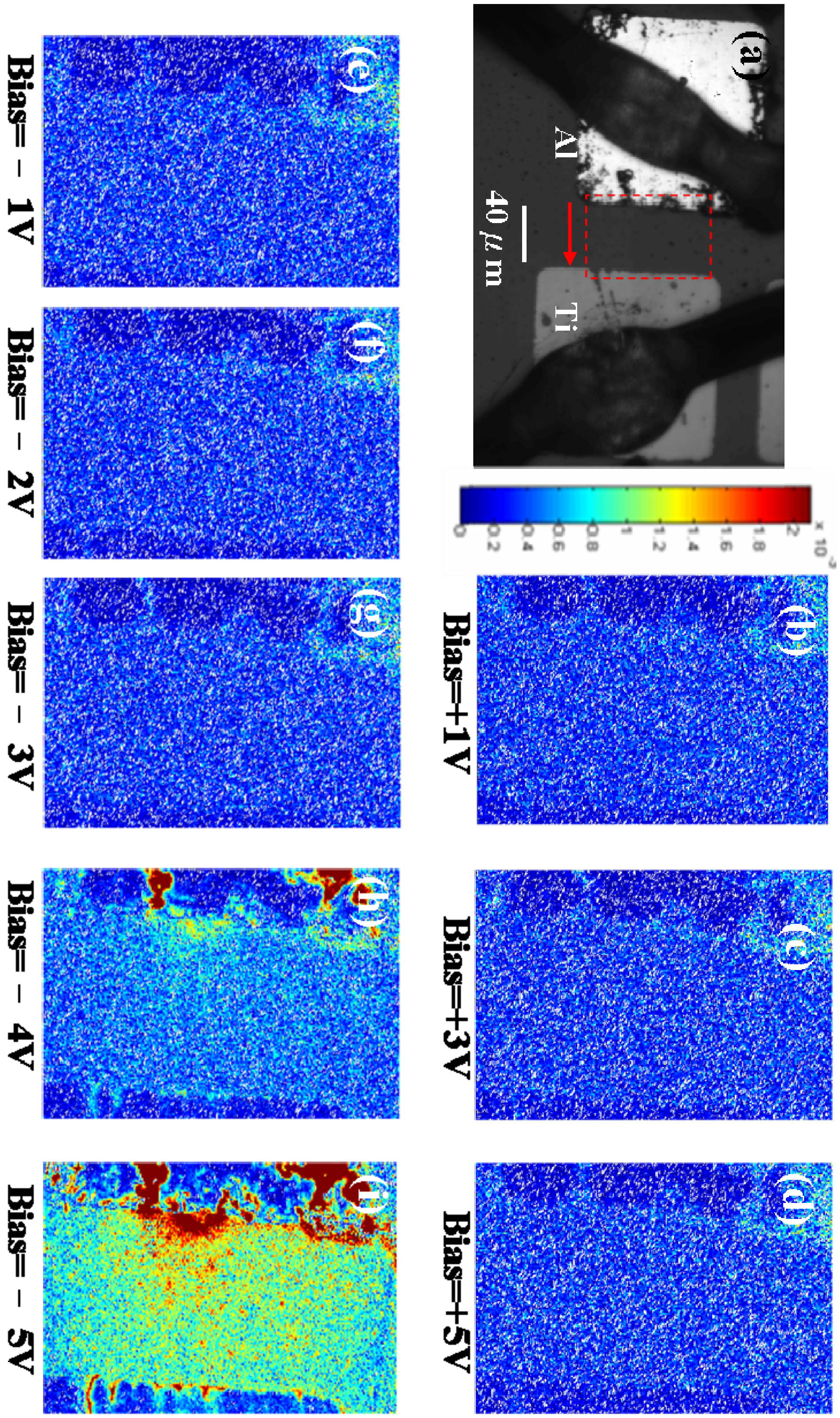

Figure 8-3 Thermoreflectance measurements of resistive switching devices. (a) Optical image of the device; (b)-(i) are the reflectance images at the highlighted region, obtained by biasing the device at different positive and negative voltage biases.

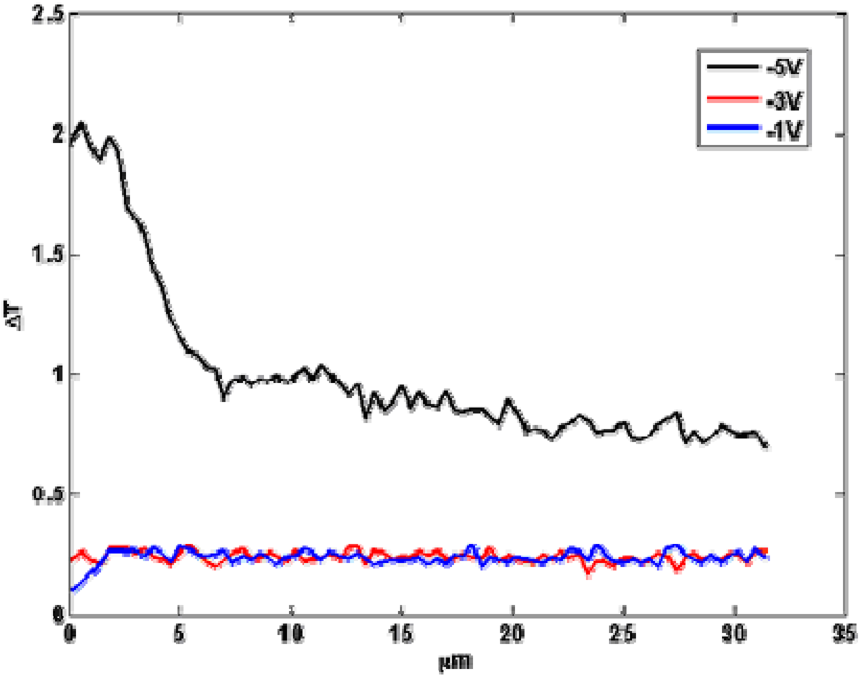

Figure 8-4 The actual temperature variation across the PCMO channel across the arrow in Figure 8-3(a) at various biases, with zero position indicating the edge of the Al electrode.

8.5 Finite element computational simulation [130]

In order to identify the origin of the localized heat sources and their relationships with the resistance switching mechanism, a two-dimensional heat transfer finite element model was developed with a commercial software (COMSOL), and the results are shown in *Figure 8-5*. The heat transfer simulation was governed by the equation $-\nabla^2 kT = q$ where k is the thermal conductivity of the material and q is the volumetric heat source. The values of k used in the simulation were 237, 21.9 and 1 $\mathrm{Wm^{-1}K^{-1}}$ for aluminum, titanium and PCMO[131], respectively. The volumetric heat source was obtained by fitting the simulated results with the experimental finding, based on the input power ($I \times V$) at LRS. Convection and radiation heat transfer were neglected in the thermal model.

In the model, Al and Ti electrodes were assumed to be connected electrically by the PCMO channels. Two different scenarios were considered. In the first case, a total of seven equally-conducting paths (each 10 μm length) were present in between the metallic electrodes (inset of *Figure 8-5(a)*). The second case (inset of *Figure 8-5(b)*) was identical to the first one except that six of the paths were blocked by the presence of oxide barriers. Equal voltage biases were assumed for both cases, and therefore the current through each channel should be identical if the metal electrodes were treated as equipotential surfaces.

In *Figure 8-5(a)*, the current is evenly injected into all of the seven paths, and uniform heating can be observed on the PCMO film. However, if only one of the channels contributes to the current follow, the current will be crowded in the particular channel. Uneven temperature distribution similar to the experimental results (*Figure 8-4(i)*) will then be obtained as shown in *Figure 8-5(b)*. It can also be observed from the simulated thermal results that if all channels are contributing to the electrical current, the maximum temperature at the PCMO thin film at LRS increases from 303K to 315 K.The heat transfer model allows us to compare the effect of the current distribution on the homogeneity of the temperature across the PCMO channel and predict the temperature profile under different bias conditions.

Since the blocking and un-blocking of the PCMO channel is closely related to the RS mechanism, it is important to discuss the possible physical origin of the effect. Janousch *et al.* observed filament paths on Cr-doped STO single crystal resistance switching device by infrared thermal imaging, although the actual temperature rise was not reported due to the low spatial resolution of the IR camera[59]. For the NiO device, Phark *et al.* demonstrated the resistance switching mechanism can be related to the thermal treatment of the device[132].

On the other hand, for PCMO RS devices, Li *et al.*[81] showed that a thin layer of

AlO_x exists at the interface between Al and PCMO by using TEM. It was proposed that the formation and dissociation of the AlO_x layer actually contributes to the RS effect in the device. This phenomenon can be explained by electrochemical reaction of the interfacial AlO_x. In the negative voltage bias, dissociation of interfacial AlO_x layer occurs, Al and oxygen are formed, and hence the electrical conductivity of the device increases. Similarly, when the device is under positive bias, AlO_x layer would be formed between the Al and PCMO interface, and the resistance of the device increases. The occurrence and removal of AlO_x thus explains the blocking and unblocking of the conducting paths from the Al into PCMO.

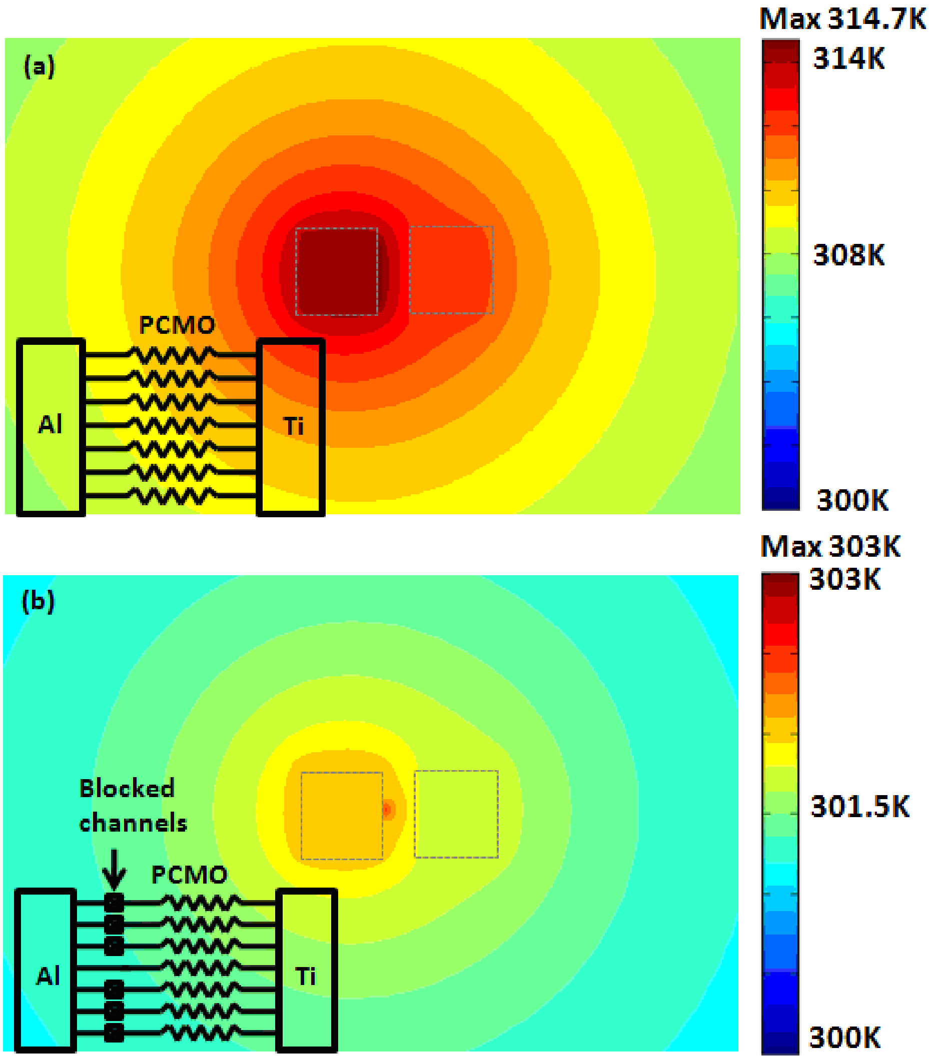

Figure 8-5 Thermal modeling results for the resistive switching devices, assuming the presence of seven heat sources (inset of (a)) or one single heat source (inset of (b)) at the Al edge.

8.6 Discussion

In order to verify the hypothesis, additional experiments were performed by using focused-ion-beam microscope to etch the area under the aluminum contact and the PCMO film, and examine subsequently those etched regions by SEM.

It can be observed from *Figure 8-7(a)* that for a device used for resistance switching measurement, a thin barrier layer is present under the aluminum electrode. This is in contrast with the case of a fresh device which has not performed any resistance switching measurement (*Figure 8-7(b)*). Such formation of oxides has been observed between PCMO and metallic electrodes by high-resolution transmission electron microscopy, and was attributed to the RS effect[81, 121]. *Figure 8-7(a)* and *(b)* directly draw the relation between the resistive states of the devices with the existence of the oxide layer at Al/PCMO interface in our devices, and how does it affects the thermal distribution at LRS and HRS .

It is also interesting to note that this interfacial layer is observed only at regions of Al electrode close to the PCMO channel, where the electric current tends to rush into the PCMO and hence has a higher electric field when the device is under operations. No such a barrier was observed at the interface in the central region of the Al electrode (*Figure 8-7(c)*). Moreover, in the optical microscopy image (*Figure 8-6*), lots of bubbles are formed near the edge of the Al, where the thin barrier layer exists. It is correlated to the finding in the SEM image, which the layer is only observed at regions of Al electrode close to the PCMO channel. Furthermore, no barrier is observed in the edge of Ti electrode, which further strengthen the resistive switching is due to the existence of the oxide layer at Al/PCMO interface.

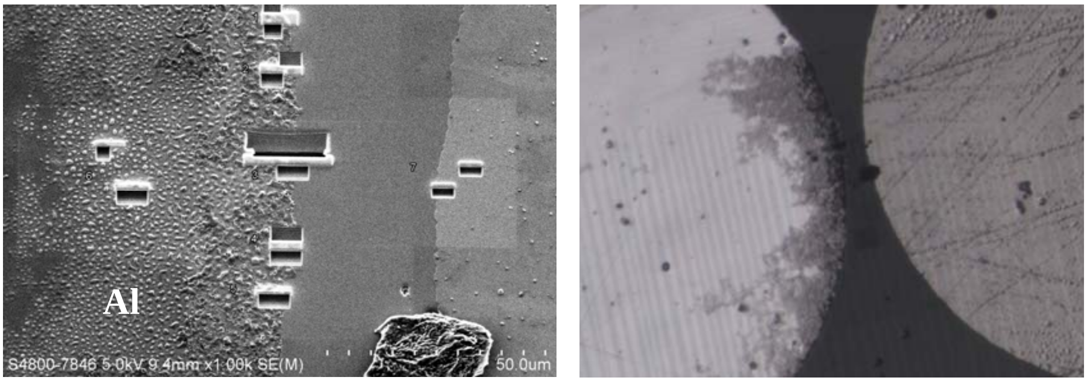

Figure 8-6 Scanning electron micrograph (left) and optical micrograph (right) of the device; difference is observed between regions of Al electrode close to the PCMO channel and the central region of the Al electrode.

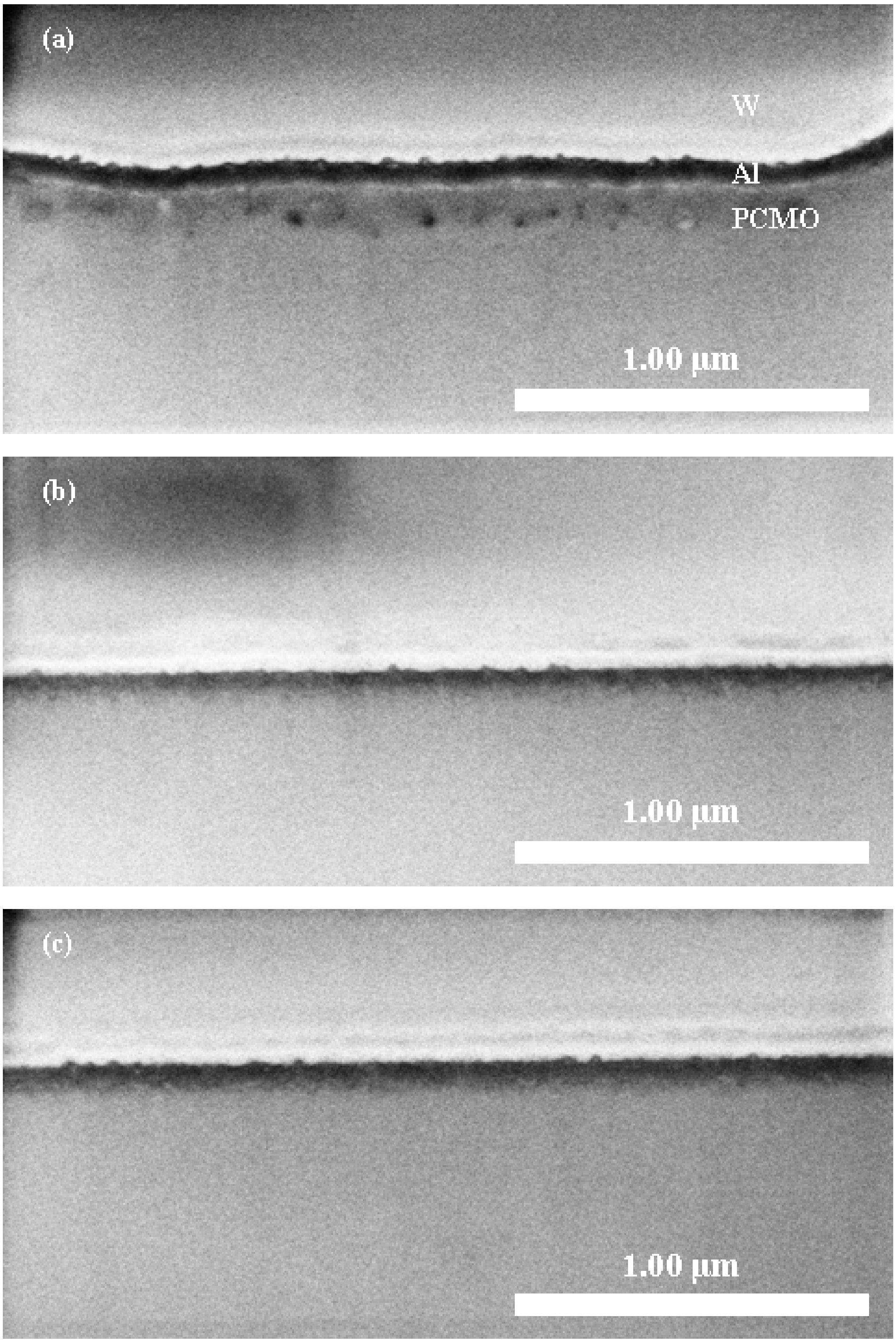

Figure 8-7 The cross-sectional scanning electron micrographs of Al/PCMO interfaces. The interface at regions close to the PCMO channel are shown for devices with (a) or without (b) performing resistive switching. (c) shows the Al/PCMO interface at the centre of Al electrode for the switched device. Tungsten (W) layers on Al were deposited for sample protection during FIB etching.

By combining our experimental findings from the thermal imaging method and the SEM images, we can conclude that uneven current injection occurred in the device which caused an inhomogenous temperature distribution. Such an uneven current injection is believed to be due to the variation of the AlO_x thickness underneath the Al electrode. It is possible that at some regions the AlO_x fails to be reduced back into Al and shuts the corresponding current channel into PCMO; in the long-run this would raise the equivalent resistance of the device. A larger voltage bias is therefore required to enforce the reaction to take place. It can thus be postulated that if the RS device is modulated by a current source, a thermal runaway process would occur due to the cumulative current crowding effect over a limited number of channels, which speeds up the degradation of the device. On the other hand, if a voltage bias is used to modulate the resistance switching device, a gradual increase in the overall resistance of the device would be expected in the long run due to the incomplete reduction of the aluminum oxide under large negative bias. This results in a gradual decrease in resistance switching ratio, given that the voltage bias source does not affect the high resistance state under positive bias. Partial support of this claim can also be found in *Figure 5-6 and Figure 7-3*, which demonstrates a continuous measure increase of LRS resistance value with repeated switching by application of fixed positive and negative pulses.

8.7 Conclusion

In conclusion, uneven current injection into the PCMO resistance switching device has been observed by high-resolution thermal imaging method. A heated region with width 10 μm was detected. By combining thermal images under different bias levels and the SEM images, an explanation for the RS mechanism of the PCMO device was provided.

Since the uneven current injection is difficult to be observed by performing electrical measurement as all the channels are connected in parallel, the proposed thermal imaging method thus provides a novel, *in-situ* and powerful technique to characterize RS devices by measuring the area of active channels and hence the total injection current. Moreover, both measurements and simulation have been determine that when the RS device switch from HRS to LRS, a 7-fold increase on temperature variation can be observed at the hot spots.

Chapter 9 Conclusion

The research work in this thesis includes the fabrication of resistive switching oxide thin film devices based on two types of manganites, LSMO and PCMO. Characterization of the devices were done, including structural and electrical analysis. Both LSMO and PCMO were epitaxially grown on LAO (001) substrates using pulsed laser deposition technique. The characteristics of the switching devices were studied using electrical measurements.

Planar LSMO thin film resistive switching devices with Au electrodes performed multi-level resistive switching, by applying different voltages after the forming process. Those multi-level resistance states showed good stability up to 30 mins and reproducibility up to 10^4 multi-switching cycles.

Planar PCMO thin films with different metal electrodes were fabricated for studying metal electrodes dependence of resistive switching. Only devices with Al electrodes performed switching effect. Moreover, switching ratio performance of the devices was also studied, and the switching ratio was shown to be governed by the applied voltage pulse width and magnitude. In order to reduce the switching magnitude by the keeping the switching ratio constant, a longer pulse width is required. In contrast, increasing the pulse magnitude can reduce the pulse duration required for generating a constant switching ratio.

In order to improve the potential application of PCMO resistive switching devices, top-down geometry PCMO was also studied. Epitaxial PCMO thin film growth on conducting LNO bottom electrode with LAO substrate was fabricated. The devices with Ti metal electrodes showed switching effect after the forming process. Only ±5 V was enough to switch the devices in between HRS and LRS.

The resistive switching mechanism of the PCMO devices was investigated using basic electrical measurements, three-point and four-point measurements, as well as thermal measurements. Electrical measurements showed that the interface of Al/PCMO contributed to the switching effect, and linear *I-V* characterization in four-point measurement determined that the bulk of PCMO thin film alone was not able to explain the effect. Moreover, thermal measurements with thermocouples and thermoreflectance imaging technique showed an uneven heating between electrodes, and higher temperature was obtained at regions of Al electrode close to the PCMO channel. Furthermore, a resistive layer was observed at Al/PCMO interface in switching devices by SEM.

A mechanism of resistive switching was proposed, in which electrochemical reaction of the interfacial AlO_x was suggested to be responsible for the resistive switching effect. By the formation and dissociation of the AlO_x layer under different voltages of polarities, the resistance of the sample changed due to the thickness variation of the resistive AlO_x layer. This reaction further explained why the endurance and retention performances of the devices were not good enough for commercial application at the moment. Due to the variation of the thickness changes in AlO_x during the application of the voltage bias, fluctuation of the resistive states values were observed.

To conclude, resistive switching effect has the potential for being used as commercial memory products, especially for devices with Al electrodes. By controlling the thickness of AlO_x in the interface, commercial memory products with high density and good stability are possible.

References

[1] "SanDisk® Cruzer® USB Flash Drive", *http://www.sandisk.com/products/usb-flash-drives/sandisk-cruzer-usb-flash-drive-(new-design!).aspx,* 2009.

[2] "Kingston USB Flash Drives", *http://www.kingston.com/flash/DataTravelers_consumer.asp,* 2009.

[3] "Hitachi Glogal Storage Technologies", *http://www.hitachigst.com/portal/site/en/products/travelstar/,* 2009.

[4] "Fujitsu 500 GB 2.5" HDD Models", *http://www.fujitsu.com/global/news/pr/archives/month/2008/20081111-01.html,* 2009.

[5] "Hard disk drive news," *http://www.storagesearch.com/diskwin.html,* 2009.

[6] "Western digital 2008 annual report", *https://materials.proxyvote.com/Approved/958102/20080917/AR_27910/HTML2/western_digital-ar2008_0038.html,* 2009.

[7] "Web-Feet Research", *http://webfeet.sp360hosting.com/default.aspx,* 2009.

[8] "International Technology Roadmap for Semiconductors", *http://www.itrs.net/,* 2008.

[9] J. C. Scott, "Is There an Immortal Memory?", in *Science*. vol. 304: AAAS, pp. 2, 2004.

[10] "ITRS annual edition report 2007", *http://www.itrs.net/Links/2007ITRS/2007_Chapters/2007_PIDS.pdf,* 2007.

[11] T. Li, *Materials and processes for nonvolatile memories II : symposium held April 10-13, 2007, San Francisco, California, U.S.A*. Warrendale, Pa. ,Materials Research Society, 2007.

[12] "IBM's Magnetic Race-Track Memory", *http://webfeet.sp360hosting.com/nbblogsummary/Lists/Posts/Post.aspx?ID=45,* 2008.

[13] E. T. Wertz and Q. Li, "Magnetoresistance after initial demagnetization in $La_{0.67}Sr_{0.33}]MnO_3/SrTiO_3/La_{0.67}Sr_{0.33}MnO_3$ magnetic tunnel junctions", *Applied Physics Letters,* vol. 90, 142506, 2007.

[14] Y. Ogimoto, M. Izumi, A. Sawa, T. Manako, H. Sato, H. Akoh, M. Kawasaki, and Y. Tokura, "Tunneling Magnetoresistance above Room Temperature in $La_{0.7}Sr_{0.3}MnO_3/SrTiO_3/La_{0.7}Sr_{0.3}MnO_3$Junctions", *Japanese Journal of Applied Physics,* vol. 42, pp. L369, 2003.

[15] W. F. Cheng, A. Ruotolo, Y. K. Chan, K. H. Wong, and C. W. Leung,

"Spacerless metal-manganite pseudo-spin-valve structure", *Journal of Applied Physics,* vol. 103, 103903, 2008.

[16] R. E. Jones, P. D. Maniar, R. Moazzami, P. Zurcher, J. Z. Witowski, Y. T. Lii, P. Chu, and S. J. Gillespie, "Ferroelectric non-volatile memories for low-voltage, low-power applications", *Thin Solid Films,* vol. 270, pp. 584-588, 1995.

[17] W. Xin Yi, Y. Jun, W. Yun Bo, Z. Wen Li, G. Jun Xiong, and C. Xiao Hui, "Preparation and Characterization of BPO Film as Electrode for Using of FeRAM", *Chinese Physics Letters,* pp. 2694, 2008.

[18] T. Mikolajick, C. Dehm, W. Hartner, I. Kasko, M. J. Kastner, N. Nagel, M. Moert, and C. Mazure, "FeRAM technology for high density applications", *Microelectronics Reliability,* vol. 41, pp. 947-950, 2001.

[19] S. Raoux, R. M. Shelby, J. Jordan-Sweet, B. Munoz, M. Salinga, Y. C. Chen, Y. H. Shih, E. K. Lai, and M. H. Lee, "Phase change materials and their application to random access memory technology", *Microelectronic Engineering,* vol. 85, pp. 2330-2333, 2008.

[20] N. J. W. S.Q. Liu and A. Ignatiev, "A New Concept for Non-Volatile Memory: The Electric-Pulse Induced Resistive Change Effect in Colossal Magnetoresistive Thin Films", *Chinese University of Hong Kong Seminar,* 2005.

[21] H. Schroeder and D. S. Jeong, "Resistive switching in a Pt/TiO_2/Pt thin film stack - a candidate for a non-volatile ReRAM", *Microelectronic Engineering,* vol. 84, pp. 1982-1985, 2007.

[22] G. I. Meijer, "Who Wins the Nonvolatile Memory Race?", in *Science*. vol. 319, pp. 1625-1626, 2008.

[23] D. Hsu, J. G. Lin, and W. F. Wu, "Resistive switching effects in $Nd_{0.7}Ca_{0.3}MnO_3$ manganite", *Journal of Magnetism and Magnetic Materials,* vol. 310, pp. 978-980, 2007.

[24] A. Sawa, "Resistive switching in transition metal oxides", *Materials Today,* vol. 11, pp. 28-36, 6 2008.

[25] C. Acha, "Electric pulse-induced resistive switching in ceramic $YBa_2Cu_3O_{7-\Delta}$/Au interfaces," *Physica B: Condensed Matter,* vol. In Press, Corrected Proof.

[26] S. Duhalde, M. Villafuerte, G. Juarez, and S. P. Heluani, "Electric field-driven resistive switching in magnetoresistive $La_{0.5}Ca_{0.5}MnO_3$ thin films", *Physica B: Condensed Matter,* vol. 354, pp. 11-15, 2004.

[27] L. Huang, B. Qu, L. Liu, and L. Zhang, "Study on the resistive switching properties of epitaxial $La_{0.67}Sr_{0.33}MnO_3$ films", *Solid State Communications,* vol. 143, pp. 382-385, 2007.

[28] A. Odagawa, T. Kanno, H. Adachi, H. Sato, I. H. Inoue, H. Akoh, M. Kawasaki, and Y. Tokura, "Temperature dependence of colossal electro-resistance of $Pr_{0.7}Ca_{0.3}MnO_3$ thin films", *Thin Solid Films,* vol. 486, pp. 75-78, 2005.

[29] D. S. Kim, C. E. Lee, Y. H. Kim, and Y. T. Kim, "Effect of oxygen annealing on $Pr_{0.7}Ca_{0.3}MnO_3$ thin film for colossal electroresistance at room temperature", *Journal of Applied Physics,* vol. 100, 093901, 2006.

[30] G. Dearnaley, A. M. Stoneham, and D. V. Morgan, "Electrical phenomena in amorphous oxide films", *Reports on Progress in Physics,* vol. 33, pp. 1129-1191, 1970.

[31] B. P. Andreasson, M. Janousch, U. Staub, G. I. Meijer, and B. Delley, "Resistive switching in Cr-doped $SrTiO_3$: An X-ray absorption spectroscopy study", *Materials Science and Engineering: B,* vol. 144, pp. 60-63, 2007.

[32] X. Cao, X. Li, W. Yu, X. Liu, and X. He, "Bipolar resistive switching properties of microcrystalline TiO_2 thin films deposited by pulsed laser deposition", *Materials Science and Engineering: B,* vol. 157, pp. 36-39, 2009.

[33] D. S. Kim, Y. H. Kim, C. E. Lee, and Y. T. Kim, "Resistive switching characteristics of $Pr_{0.7}Ca_{0.3}MnO_3$ thin films grown on glass substrates by pulsed laser deposition", *Thin Solid Films,* vol. 515, pp. 2573-2576, 2006.

[34] W. G. Kim and S. W. Rhee, "Effect of the top electrode material on the resistive switching of TiO_2 thin film", *Microelectronic Engineering,* vol. In Press, Corrected Proof.

[35] W. G. Kim and S. W. Rhee, "Effect of post annealing on the resistive switching of TiO_2 thin film", *Microelectronic Engineering,* vol. In Press, Corrected Proof.

[36] X. Liu, Z. Ji, D. Tu, L. Shang, J. Liu, M. Liu, and C. Xie, "Organic nonpolar nonvolatile resistive switching in poly(3,4-ethylene-dioxythiophene): Polystyrenesulfonate thin film," *Organic Electronics,* vol. 10, pp. 1191-1194, 2009.

[37] N. Xu, L. Liu, X. Sun, X. Liu, D. Han, Y. Wang, R. Han, J. Kang, and B. Yu, "Characteristics and mechanism of conduction/set process in TiN/ZnO/Pt resistance switching random-access memories", *Applied Physics Letters,* vol. 92, 232112, 2008.

[38] M. J. Rozenberg, I. H. Inoue, and M. J. Sanchez, "Nonvolatile memory with multilevel switching: A basic model", *Physical Review Letters,* vol. 92, 178302, 2004.

[39] R. Waser and M. Aono, "Nanoionics-based resistive switching memories", *Nature Materials,* vol. 6, pp. 833-840, 2007.

[40] J. E. Brewer and M. Gill, "Nonvolatile memory technologies with emphasis on Flash: a comprehensive guide to understanding and using NVM devices",

Hoboken, *N.J. Wiley*, 2008.

[41] R. Waser, "Resistive non-volatile memory devices (Invited Paper)," *Microelectronic Engineering,* vol. 86, pp. 1925-1928, 2009.

[42] M. Colle, M. Buchel, and D. M. de Leeuw, "Switching and filamentary conduction in non-volatile organic memories", *Organic Electronics,* vol. 7, pp. 305-312, 2006.

[43] D. S. Shang, Q. Wang, L. D. Chen, R. Dong, X. M. Li, and W. Q. Zhang, "Effect of carrier trapping on the hysteretic current-voltage characteristics in Ag/$La_{0.7}Ca_{0.3}MnO_3$/Pt heterostructures", *Physical Review B (Condensed Matter and Materials Physics),* vol. 73, 245427, 2006.

[44] D. C. Shang, D. Lidong; Q. Wang, Qun; Z. H. Wu, Zihua; W. Q. Zhang, Wenqing; X. M. Li, Xiaomin, "Reversible multilevel resistance switching of Ag/$La_{0.7}Ca_{0.3}MnO_3$/Pt heterostructures", *Journal of Materials Research,* vol. 23, 6, 2008.

[45] R. Oligschlaeger, R. Waser, R. Meyer, S. Karthauser, and R. Dittmann, "Resistive switching and data reliability of epitaxial (Ba,Sr)TiO_3 thin films", *Applied Physics Letters,* vol. 88, 042901, 2006.

[46] S. Q. Liu, N. J. Wu, and A. Ignatiev, "Electric-pulse-induced reversible resistance change effect in magnetoresistive films", *Applied Physics Letters,* vol. 76, pp. 2749-2751, 2000.

[47] S. Tsui, "Field-induced resistive switching in metal-oxide interfaces", *Applied Physics Letters,* vol. 85, pp. 317-319, 2004.

[48] T. Kenta, O. Isao, K. Hiroshi, O. Masaharu, K. I. Yuji Matsumoto, O. Tsuyoshi, L. Mikk, and K. Hideomi, "High-throuhgput characterization of metal electrode performance for electric-field-induced resistance switching in metal/PCMO/metal structures", *Advanced Materials, Wiley,* vol. 19, pp. 1711-1713, 2007.

[49] A. Baikalov, "Field-driven hysteretic and reversible resistive switch at the Ag-$Pr_{0.7}Ca_{0.3}MnO_3$ interface", *Applied Physics Letters,* vol. 83, pp. 957-959, 2003.

[50] M. Meier, S. Gilles, R. Rosezin, C. Schindler, S. Trellenkamp, A. Rudiger, D. Mayer, C. Kugeler, and R. Waser, "Resistively switching Pt/spin-on glass/Ag nanocells for non-volatile memories fabricated with UV nanoimprint lithography", *Microelectronic Engineering,* vol. 86, pp. 1060-1062, 2009.

[51] C. Liang, K. Terabe, T. Hasegawa and A. Masakazu, "Resistance switching of an individual Ag_2S / Ag nanowire heterostructure", *Nanotechnology,* vol. 18, 485202, 2007.

[52] Y. Naitoh, M. Horikawa, H. Abe, and T. Shimizu, "Resistance switch

employing a simple metal nanogap junction", *Nanotechnology,* vol. 17, 5669, 2006.

[53] W. W. Zhuang, W. Pan, B. D. Ulrich, J. J. Lee, L. Stecker, A. Burmaster, D. R. Evans, S. T. Hsu, M. Tajiri, A. Shimaoka, K. Inoue, T. Naka, N. Awaya, A. Sakiyama, Y. Wang, S. Q. Liu, N. J. Wu, and A. Ignatiev, "Novel colossal magnetoresistive thin film nonvolatile resistance random access memory (RRAM)", *Electron Devices Meeting, 2002. IEDM '02. Digest. International,* 4, 2002.

[54] I. G. Baek, D. C. Kim, M. J. Lee, H. J. Kim, E. K. Yim, M. S. Lee, J. E. Lee, S. E. Ahn, S. Seo, J. H. Lee, J. C. Park, Y. K. Cha, S. O. Park, H. S. Kim, I. K. Yoo, U. I. Chung, J. T. Moon, and B. I. Ryu, "Multi-layer cross-point binary oxide resistive memory (OxRRAM) for post-NAND storage application", *Electron Devices Meeting, 2005. IEDM Technical Digest. IEEE International,* 4, 2005.

[55] C. Yoshida, K. Tsunoda, H. Noshiro, and Y. Sugiyama, "High speed resistive switching in Pt/TiO_2/TiN film for nonvolatile memory application", *Applied Physics Letters,* vol. 91, 223510, 2007.

[56] J. F. Gibbons and W. E. Beadle, "Switching properties of thin NiO films", *Solid-State Electronics,* vol. 7, pp. 785-790, 1964.

[57] M. D. Lee, C. K. Lo, T. Y. Peng, S. Y. Chen, and Y. D. Yao, "Endurance study of switching characteristics in NiO films", *Proceedings of the 17th International Conference on Magnetism, The International Conference on Magnetism,* vol. 310, pp. e1030-e1031, 2007.

[58] B. J. Choi, "Resistive switching mechanism of TiO_2 thin films grown by atomic-layer deposition", *Journal of Applied Physics,* vol. 98, 033715, 2005.

[59] M. Janousch, G. I. Meijer, U. Staub, B. Delley, S. F. Karg, and B. P. Andreasson, "Role of Oxygen Vacancies in Cr-Doped $SrTiO_3$ for Resistance-Change Memory", in *Advanced Materials*. vol. 19, pp. 2232-2235, 2007.

[60] T. W. Hickmott, "Low-Frequency Negative Resistance in Thin Anodic Oxide Films", *Journal of Applied Physics,* vol. 33, pp. 2669-2682, 1962.

[61] M. Hasan, R. Dong, D. S. Lee, D. J. Seong, H. J. Choi, M. B. Pyun, and H. Hwang, "A Materials Approach to Resistive Switching Memory Oxides", *Journal of Semiconductor Technology and Science,* vol. 8, pp. 66-79, 2008.

[62] G. S. Park, X. S. Li, D. C. Kim, R. J. Jung, M. J. Lee, and S. Seo, "Observation of electric-field induced Ni filament channels in polycrystalline NiO_x film", *Applied Physics Letters,* vol. 91, 222103, 2007.

[63] K. M. Kim, B. J. Choi, and C. S. Hwang, "Localized switching mechanism in resistive switching of atomic-layer-deposited TiO_2 thin films", *Applied Physics*

Letters, vol. 90, 242906, 2007.

[64] K. Kinoshita, T. Tamura, M. Aoki, Y. Sugiyama, and H. Tanaka, "Bias polarity dependent data retention of resistive random access memory consisting of binary transition metal oxide", *Applied Physics Letters,* vol. 89, 103509, 2006.

[65] S. Seo, M. J. Lee, D. H. Seo, S. K. Choi, D. S. Suh, Y. S. Joung, I. K. Yoo, I. S. Byun, I. R. Hwang, S. H. Kim, and B. H. Park, "Conductivity switching characteristics and reset currents in NiO films", *Applied Physics Letters,* vol. 86, 093509, 2005.

[66] D. C. Kim, S. Seo, S. E. Ahn, D. S. Suh, M. J. Lee, B. H. Park, I. K. Yoo, I. G. Baek, H. J. Kim, E. K. Yim, J. E. Lee, S. O. Park, H. S. Kim, U. I. Chung, J. T. Moon, and B. I. Ryu, "Electrical observations of filamentary conductions for the resistive memory switching in NiO films", *Applied Physics Letters,* vol. 88, 202102, 2006.

[67] D. W. Kim, B. H. Park, R. Jung, and S. Seo, "Reversible Resistance Switching Behaviors of Pt/NiO/Pt Structures", *Japanese Journal of Applied Physics,* vol. 46, pp. 5205, 2007.

[68] A. Sawa, T. Fujii, M. Kawasaki, and Y. Tokura, "Hysteretic current-voltage characteristics and resistance switching at a rectifying Ti/$Pr_{0.7}Ca_{0.3}MnO_3$ interface", *Applied Physics Letters,* vol. 85, pp. 4073-4075, 2004.

[69] T. Fujii, M. Kawasaki, A. Sawa, H. Akoh, Y. Kawazoe, and Y. Tokura, "Hysteretic current-voltage characteristics and resistance switching at an epitaxial oxide Schottky junction $SrRuO_3$/$SrTi_{0.99}Nb_{0.01}O_3$", *Applied Physics Letters,* vol. 86, 012107, 2005.

[70] A. Ruotolo, C. Y. Lam, W. F. Cheng, K. H. Wong, and C. W. Leung, "High-quality all-oxide Schottky junctions fabricated on heavily doped Nb:$SrTiO_3$ substrates", *Physical Review B (Condensed Matter and Materials Physics),* vol. 76, 075122, 2007.

[71] M. Hamaguchi, K. Aoyama, S. Asanuma, Y. Uesu, and T. Katsufuji, "Electric-field-induced resistance switching universally observed in transition-metal-oxide thin films", *Applied Physics Letters,* vol. 88, 142508, 2006.

[72] A. Odagawa, H. Sato, I. H. Inoue, H. Akoh, M. Kawasaki, Y. Tokura, T. Kanno, and H. Adachi, "Colossal electroresistance of a $Pr_{0.7}Ca_{0.3}MnO_3$ thin film at room temperature", *Physical Review B (Condensed Matter and Materials Physics),* vol. 70, 224403, 2004.

[73] C. J. Kim and I. W. Chen, "Effect of top electrode on resistance switching of (Pr, Ca)MnO_3 thin films", *Thin Solid Films,* vol. 515, pp. 2726-2729, 2006.

[74] R. Dong, Q. Wang, L. D. Chen, D. S. Shang, T. L. Chen, X. M. Li, and W. Q.

Zhang, "Retention behavior of the electric-pulse-induced reversible resistance change effect in Ag-$La_{0.7}Ca_{0.3}MnO_3$-Pt sandwiches", *Applied Physics Letters,* vol. 86, 172107, 2005.

[75] W. Y. Yang, W. G. Kim, and S. W. Rhee, "Radio frequency sputter deposition of single phase cuprous oxide using Cu_2O as a target material and its resistive switching properties", *Thin Solid Films,* vol. 517, pp. 967-971, 2008.

[76] R. Dong, D. S. Lee, W. F. Xiang, S. J. Oh, D. J. Seong, S. H. Heo, H. J. Choi, M. J. Kwon, S. N. Seo, M. B. Pyun, M. Hasan, and H. Hwang, "Reproducible hysteresis and resistive switching in metal-Cu_xO-metal heterostructures", *Applied Physics Letters,* vol. 90, 042107, 2007.

[77] Y. B. Nian, J. Strozier, N. J. Wu, X. Chen, and A. Ignatiev, "Evidence for an Oxygen Diffusion Model for the Electric Pulse Induced Resistance Change Effect in Transition-Metal Oxides", *Physical Review Letters,* vol. 98, 146403, 2007.

[78] C. Yoshida, K. Kinoshita, T. Yamasaki, and Y. Sugiyama, "Direct observation of oxygen movement during resistance switching in NiO/Pt film", *Applied Physics Letters,* vol. 93, 042106, 2008.

[79] R. Dong, W. F. Xiang, D. S. Lee, S. J. Oh, D. J. Seong, S. H. Heo, H. J. Choi, M. J. Kwon, M. Chang, M. Jo, M. Hasan, and H. Hwang, "Improvement of reproducible hysteresis and resistive switching in metal-$La_{0.7}Ca_{0.3}MnO_3$-metal heterostructures by oxygen annealing", *Applied Physics Letters,* vol. 90, 182118, 2007.

[80] K. Shono, H. Kawano, T. Yokota, and M. Gomi, "Origin of Negative Differential Resistance Observed on Bipolar Resistance Switching Device with Ti/$Pr_{0.7}Ca_{0.3}MnO_3$/Pt Structure", *Applied Physics Express,* vol. 1, 055002, 2008.

[81] S. L. Li, Z. L. Liao, J. Li, J. L. Gang, and D. N. Zheng, "Resistive switching properties and low resistance state relaxation in Al/$Pr_{0.7}Ca_{0.3}MnO_3$/Pt junctions", *Journal of Physics D: Applied Physics,* vol. 42, 045411, 2009.

[82] S. M. Sze and Kwok K. Ng, "Physics of semiconductor devices", 3rd ed., Hoboken, N.J., *Wiley-Interscience*, 2007.

[83] R. Fors, S. I. Khartsev, and A. M. Grishin, "Giant resistance switching in metal-insulator-manganite junctions: Evidence for Mott transition", *Physical Review B,* vol. 71, 045305, 2005.

[84] W. R. Hiatt and T. W. Hickmott, "Bistable switching in niobium oxide diodes", *Applied Physics Letters,* vol. 6, pp. 106-108, 1965.

[85] M. Jafar and D. Haneman, "Switching in amorphous-silicon devices", *Physical Review B,* vol. 49, 13611, 1994.

[86] W. Y. Chang, Y. C. Lai, T. B. Wu, S. F. Wang, F. Chen, and M. J. Tsai,

"Unipolar resistive switching characteristics of ZnO thin films for nonvolatile memory applications", *Applied Physics Letters,* vol. 92, 022110, 2008.

[87] D. Choi, D. Lee, H. Sim, M. Chang, and H. Hwang, "Reversible resistive switching of $SrTiO_x$ thin films for nonvolatile memory applications", *Applied Physics Letters,* vol. 88, 082904, 2006.

[88] C. H. Kim, Y. H. Jang, H. J. Hwang, Z. H. Sun, H. B. Moon, and J. H. Cho, "Observation of bistable resistance memory switching in CuO thin films", *Applied Physics Letters,* vol. 94, pp. 102107-3, 2009.

[89] Y. Watanabe, J. G. Bednorz, A. Bietsch, C. Gerber, D. Widmer, A. Beck, and S. J. Wind, "Current-driven insulator-conductor transition and nonvolatile memory in chromium-doped $SrTiO_3$ single crystals", *Applied Physics Letters,* vol. 78, pp. 3738-3740, 2001.

[90] X. Chen, J. Strozier, N. J. Wu, and A. Ignatiev, "Direct resistance profile for an electrical pulse induced resistance change device", *Applied Physics Letters,* vol. 87, 233506, 2005.

[91] T. Menke, P. Meuffels, R. Dittmann, K. Szot, and R. Waser, "Separation of bulk and interface contributions to electroforming and resistive switching behavior of epitaxial Fe-doped $SrTiO_3$", *Journal of Applied Physics,* vol. 105, 066104, 2009.

[92] J. M. D. Coey, M. Viret, and S. V. Molnar, "Mixed-valence manganites", *Advances in Physics,* vol. 48, pp. 167-293, 1999.

[93] A. M. Haghiri-Gosnet and J. P. Renard, "CMR manganites: physics, thin films and devices", *Journal of Physics D: Applied Physics,* vol. 36, pp. R127-R150, 2003.

[94] Y. Tokura and N. Nagaosa, "Orbital Physics in Transition-Metal Oxides", *Science,* vol. 288, pp. 462-468, 2000.

[95] E. Dagotto, T. Hotta, and A. Moreo, "Colossal magnetoresistant materials: the key role of phase separation", *Physics Reports,* vol. 344, pp. 1-153, 2001.

[96] M. B. Salamon and M. Jaime, "The physics of manganites: Structure and transport", *Reviews of Modern Physics,* vol. 73, 583, 2001.

[97] Y. Tomioka, A. Asamitsu, H. Kuwahara, Y. Moritomo, and Y. Tokura, "Magnetic-field-induced metal-insulator phenomena in $Pr_{1-x}Ca_xMnO_3$ with controlled charge-ordering instability", *Physical Review B,* vol. 53, pp. R1689-R1692, 1996.

[98] V. Kiryukhin, D. Casa, J. P. Hill, B. Keimer, A. Vigliante, Y. Tomioka, and Y. Tokura, "An X-ray-induced insulator-metal transition in a magnetoresistive manganite", *Nature,* vol. 386, pp. 813-815, 1997.

[99] K. Miyano, T. Tanaka, Y. Tomioka, and Y. Tokura, "Photoinduced

Insulator-to-Metal Transition in a Perovskite Manganite", *Physical Review Letters,* vol. 78, 4257, 1997.

[100] A. Asamitsu, Y. Tomioka, H. Kuwahara, and Y. Tokura, "Current switching of resistive states in magnetoresistive manganites", *Nature,* vol. 388, pp. 50-52, 1997.

[101] W. F. Cheng, A. Ruotolo, Y. K. Chan, K. H. Wong, and C. W. Leung, "Spacerless metal-manganite pseudo-spin-valve structure", *Journal of Applied Physics,* vol. 103, pp. 103903-4, 2008.

[102] M. Fujimoto, H. Koyama, S. Kobayashi, Y. Tamai, N. Awaya, Y. Nishi, and T. Suzuki, "Resistivity and resistive switching properties of $Pr_{0.7}Ca_{0.3}MnO_3$ thin films", *Applied Physics Letters,* vol. 89, pp. 243504-3, 2006.

[103] A. Ruotolo, C. W. Leung, C. Y. Lam, W. F. Cheng, K. H. Wong, and G. P. Pepe, "Unification of bulk and interface electroresistive switching in oxide systems", *Physical Review B (Condensed Matter and Materials Physics),* vol. 77, 233103, 2008.

[104] Y. Tokunaga, Y. Kaneko, J. P. He, T. Arima, A. Sawa, T. Fujii, M. Kawasaki, and Y. Tokura, "Colossal electroresistance effect at metal electrode/$La_{1-x}Sr_{1+x}MnO_4$ interfaces", *Applied Physics Letters,* vol. 88, 223507, 2006.

[105] D. S. Kim, C. E. Lee, Y. H. Kim, S. M. Jung, and Y. T. Kim, "Growth and characterization of PCMO thin films for resistance random access memory," *Journal of the Korean Physical Society,* vol. 49, 5, 2006.

[106] Douglas B. Chrisey and Graham K. Hubler, "Pulsed laser deposition of thin films", New York, *J. Wiley*, 1994.

[107] Robert Eason, "Pulsed laser deposition of thin films : applications-led growth of functional materials", Hoboken, NJ, *Wiley*, 2007.

[108] A. Masuno, T. Terashima, and M. Takano, "Transport and magnetic properties of the micro-fabricated perovskite-type manganese oxides", *Physica B: Condensed Matter,* vol. 329-333, pp. 920-921, 2003.

[109] "Basic of X-ray diffraction," *http://epswww.unm.edu/xrd/xrdbasics.pdf,* 2009.

[110] J. G. J. Chern and W. G. Oldham, "Determining specific contact resistivity from contact end resistance measurements", *Electron Device Letters, IEEE,* vol. 5, pp. 178-180, 1984.

[111] M. Bhaskaran, S. Sriram, and A. S. Holland, "Accurate Estimation of Low ($< 10^{-8}\ \Omega \cdot cm^2$) Values of Specific Contact Resistivity", *Electron Device Letters, IEEE,* vol. 29, pp. 259-261, 2008.

[112] D. Fournier, B. C. Forget, C. Boué, J. P. Roge, "Micron scale photothermal imaging", *International Journal of Thermal Sciences,* vol. 39, pp. 514-518,

2000.

[113] S. Grauby, B. C. Forget, S. Hole, and D. Fournier, "High resolution photothermal imaging of high frequency phenomena using a visible charge coupled device camera associated with a multichannel lock-in scheme", *Review of Scientific Instruments,* vol. 70, pp. 3603-3608, 1999.

[114] G. Tessier, S. Hol, and D. Fournier, "Ultraviolet illumination thermoreflectance for the temperature mapping of integrated circuits", *Optics Letters,* vol. 28, pp. 875-877, 2003.

[115] P. W. Epperlein, "Micro-Temperature Measurements on Semiconductor Laser Mirrors by Reflectance Modulation: A Newly Developed Technique for Laser Characterization", *Japanese journal of applied physics,* vol. 32, pp.5514-5522, 1993.

[116] K. L. Chan, "High resolution thermal imaging for electrical and optical characterization of electronic and photonic devices", in *Mechanical Engineering*, Doctor of Philosophy, University of Michigan, 2007.

[117] A. Beck, J. G. Bednorz, C. Gerber, C. Rossel, and D. Widmer, "Reproducible switching effect in thin oxide films for memory applications", *Applied Physics Letters,* vol. 77, pp. 139-141, 2000.

[118] K. Lee, S. Han, K. Park, J. S. Lee, S. Han, K. Park, and J. Sok, "Resistance Changes of $Pr_{0.7}Ca_{0.3}MnO_3$ Films Deposited Through rf-Magnetron Sputtering ", *Journal of the Korean physical society,* vol. 49, 4, 2006.

[119] D. W. Reagor, S. Y. Lee, Y. Li, and Q. X. Jia, "Work function of the mixed-valent manganese perovskites", *Journal of Applied Physics,* vol. 95, pp. 7971-7975, 2004.

[120] H. B. Michaelson, "The work function of the elements and its periodicity", *Journal of Applied Physics,* vol. 48, pp. 4729-4733, 1977.

[121] Z. L. Liao, Z. Z. Wang, Y. Meng, Z. Y. Liu, P. Gao, J. L. Gang, H. W. Zhao, X. J. Liang, X. D. Bai, and D. M. Chen, "Categorization of resistive switching of metal-$Pr_{0.7}Ca_{0.3}MnO_3$-metal devices", *Applied Physics Letters,* vol. 94, 253503, 2009.

[122] Y. H. You, B. S. So, J. H. Hwang, W. Cho, S. S. Lee, T. M. Chung, C. G. Kim, and K. S. An, "Impedance spectroscopy characterization of resistance switching NiO thin films prepared through atomic layer deposition", *Applied Physics Letters,* vol. 89, 222105, 2006.

[123] Y. Sato, K. Kinoshita, M. Aoki, and Y. Sugiyama, "Consideration of switching mechanism of binary metal oxide resistive junctions using a thermal reaction model", *Applied Physics Letters,* vol. 90, 033503, 2007.

[124] S. H. Chang, S. C. Chae, S. B. Lee, C. Liu, T. W. Noh, J. S. Lee, B. Kahng, J. H.

Jang, M. Y. Kim, D. W. Kim, and C. U. Jung, "Effects of heat dissipation on unipolar resistance switching in Pt/NiO/Pt capacitors", *Applied Physics Letters,* vol. 92, 183507, 2008.

[125] K. Azumi, K. Aoyama, S. Asanuma, Y. Uesu, and T. Katsufuji, "Direct observation of a repeatable change in electronic states with applied electric voltage pulses in the metal-insulator-metal structure", *Physical Review B (Condensed Matter and Materials Physics),* vol. 79, 121101, 2009.

[126] J. Christofferson, K. Maize, Y. Ezzahri, J. Shabani, X. Wang, and A. Shakouri Baskin, "Microscale and Nanoscale Thermal Characterization Techniques", in *Thermal Issues in Emerging Technologies: Theory and Application, THETA 1, Cario, Egypt*, pp. 3-9, 2007.

[127] P. K. L. Chan, K. P. Pipe, G. Qin, and Z. Ma, "Thermoreflectance imaging of current dynamics in high power SiGe heterojunction bipolar transistors", *Applied Physics Letters,* vol. 89, 233521, 2006.

[128] P. K. L. Chan, K. P. Pipe, J. J. Plant, R. B. Swint, and P. W. Juodawlkis, "Temperature mapping and thermal lensing in large-mode, high-power laser diodes", *Applied Physics Letters,* vol. 89, 201110, 2006.

[129] Z. Yan, J. Christofferson, A. Shakouri, L. Deyu, A. Majumdar, W. Yiying, F. Rong, and Y. Peidong, "Characterization of heat transfer along a silicon nanowire using thermoreflectance technique", *IEEE Transactions on Nanotechnology,* vol. 5, pp. 67-74, 2006.

[130] Simulation was done by *Dr. Paddy K.L. Chan*.

[131] M. Ikebe, H. Fujishiro, S. Kanoh, and H. Yamazaki, "Lattice effect on ferromagnetic-metal phase transition in $Pr_{0.65}Ca_{0.35}(Mn_{1-Z}Co_{Z})O_3$ and $Pr_{0.65}Ca_{0.35}(Mn_{1-Z}Cr_{Z})O_3$", *Journal of Magnetism and Magnetic Materials,* vol. 272-276, pp. 1798-1799, 2004.

[132] S. H. Phark, R. Jung, Y. J. Chang, T. W. Noh, and D. W. Kim, "Interfacial reactions and resistive switching behaviors of metal/NiO/metal structures", *Applied Physics Letters,* vol. 94, 022906, 2009.